



LUND UNIVERSITY

Methodologies for Non-aqueous Systems and Precipitating Systems as Carbon Capture Technologies

A case-study of AMP-NMP

Sanku, Meher

2020

Document Version:

Publisher's PDF, also known as Version of record

[Link to publication](#)

Citation for published version (APA):

Sanku, M. (2020). *Methodologies for Non-aqueous Systems and Precipitating Systems as Carbon Capture Technologies: A case-study of AMP-NMP*. Department of Chemical Engineering, Lund University.

Total number of authors:

1

General rights

Unless other specific re-use rights are stated the following general rights apply:

Copyright and moral rights for the publications made accessible in the public portal are retained by the authors and/or other copyright owners and it is a condition of accessing publications that users recognise and abide by the legal requirements associated with these rights.

- Users may download and print one copy of any publication from the public portal for the purpose of private study or research.
- You may not further distribute the material or use it for any profit-making activity or commercial gain
- You may freely distribute the URL identifying the publication in the public portal

Read more about Creative commons licenses: <https://creativecommons.org/licenses/>

Take down policy

If you believe that this document breaches copyright please contact us providing details, and we will remove access to the work immediately and investigate your claim.

LUND UNIVERSITY

PO Box 117
221 00 Lund
+46 46-222 00 00

Methodologies for Non-aqueous Systems and Precipitating Systems as Carbon Capture Technologies

MEHER GEETIKA SANKU | CHEMICAL ENGINEERING | LUND UNIVERSITY



Methodologies for Non-aqueous Systems and Precipitating Systems as Carbon Capture Technologies

A case-study of AMP-NMP

Meher Geetika Sanku



LUND
UNIVERSITY

DOCTORAL DISSERTATION

which by due permission of the Faculty of Engineering, Lund University,
Sweden,

will be defended on 20th February, 2020 at 13:15 in lecture hall K:B at
Kemicentrum, Naturvetarvägen 14, Lund.

Faculty opponent

Assoc. Prof. Kathryn Mumford, University of Melbourne

Organization LUND UNIVERSITY Department of Chemical engineering P.O. Box 124 SE-221 00 Lund Sweden Author(s) Meher Geetika Sanku	Document name DOCTORAL THESIS	
	Date of issue 20 th February, 2020	
	Sponsoring organization Swedish Energy Agency, Göteborg Energi Research Foundation, MISTRA	
Title and subtitle Methodologies for Non-aqueous Systems and Precipitating Systems as Carbon Capture Technologies - A case study of AMP-NMP		
Abstract <p>In order to combat the effects of climate change, it is important to use a combination of solutions to achieve carbon neutrality as soon as possible. Carbon capture and sequestration is one such technology that can be used to significantly reduce the carbon footprint of many industrial plants. A mature technology for CO₂ capture, amine-based post-combustion capture, is readily available today. However, the economic cost associated with CO₂ capture plants constitutes a serious problem. Therefore, new systems are being developed in an attempt to reduce the cost of CO₂ capture. Non-aqueous systems and precipitating systems are among the new systems being considered.</p> <p>Research in such systems is still relatively new, and it will be several years before they can be applied commercially. The somewhat ambitious aim of the work presented in this thesis was to accelerate research in these fields by concentrating on methodologies that can be used in any non-aqueous systems (precipitating or non-precipitating) and precipitating systems (aqueous or non-aqueous). Two main research questions were posed to this end: 1) How can non-aqueous systems be modelled? and 2) How can the crystallization kinetics for gas-liquid-solid systems be estimated? Methodologies required to answer these questions were developed and tested for the case of the amine, 2-amino-2-methyl-1-propanol (AMP), in the organic solvent, N-methyl-2-pyrrolidone (NMP). This is a non-aqueous system and leads to precipitation when AMP reacts with CO₂, i.e., it is also a precipitating system.</p> <p>The system was modelled using an unsymmetric reference state of infinite dilution in water for ions. It was shown that using this for ions in non-aqueous solutions is thermodynamically valid, and it was applied to the AMP-in-NMP system. Experiments were performed to gain an understanding of the effect of equilibrium time, temperature, CO₂ loading, and amine concentration on the solubility of CO₂ in solution. These experiments were used to obtain the model parameters, and the model provided satisfactory predictions.</p> <p>Regarding the crystallization kinetics, theoretical modifications to the semi-empirical power law relation are suggested in the cases of gas-liquid-solid equilibrium. The experimental procedure developed to estimate the crystallization kinetics was refined, and complications such as varying crystal structure are taken into consideration. The developed theory was assessed for the AMP-NMP system. The saturation conditions for the system, required in assessing crystallization kinetics, were obtained using the thermodynamic model developed in this thesis. Although developed for the case of AMP in NMP, the methodologies presented here for modelling thermodynamic behavior and crystallization kinetics can be extended to other non-aqueous systems and precipitating systems, respectively.</p>		
Key words CO ₂ capture, non-aqueous, precipitating, thermodynamic model, crystallization kinetics		
Classification system and/or index terms (if any)		
Supplementary bibliographical information		Language English
ISSN and key title		ISBN 978-91-7422-726-0 (printed) 978-91-7422-727-7 (digital)
Recipient's notes	Number of pages 205	Price
	Security classification	

I, the undersigned, being the copyright owner of the abstract of the above-mentioned dissertation, hereby grant to all reference sources permission to publish and disseminate the abstract of the above-mentioned dissertation.

Signature

Date 09-01-2020

Methodologies for Non-aqueous Systems and Precipitating Systems as Carbon Capture Technologies

A case-study of AMP-NMP

Meher Geetika Sanku



LUND
UNIVERSITY

Coverphoto: Power plant at Kozani, Greece

Source: Adobe Stock, Artist: Verve

Copyright Introductory summary Meher Geetika Sanku

Paper 1 © Elsevier

Paper 2 © Elsevier

Paper 3 © The authors (Open access)

Paper 4 © The authors (Submitted)

Faculty of Engineering
Department of Chemical Engineering

ISBN 978-91-7422-726-0 (Print)

ISBN 978-91-7422-727-7 (PDF)

Printed in Sweden by Media-Tryck, Lund University
Lund 2020



Media-Tryck is a Nordic Swan Ecolabel
certified provider of printed material.
Read more about our environmental
work at www.mediatryck.lu.se

MADE IN SWEDEN 

Errata/Corrigendum

This sheet lists the errors and corresponding corrections for the doctoral thesis by Meher Geetika Sanku titled: “Methodologies for Non-aqueous Systems and Precipitating Systems as Carbon Capture Technologies”

ISBN (printed): 978-91-7422-726-0

ISBN (digital): 978-91-7422-727-7

Location	Original text	Correction
Page 49, Figure 4.3 caption, Line 2	...experimental data (points)...	... experimental data where the equilibrium time is 30 min (points)...
Page 50, Para 2, Line 10	...in Figure 2.5...	...in Figure 2.6...
Page 63, Line 5	...this chapter: 1) The shift...	...this chapter three things must be addressed: 1) The shift...
Page 69, Para 2, Line 15	...the cooling rate is high,...	...the cooling rate is low,...
Paper I, Page 3, Line 4 after Equation (6)	...(, [kJ])...	...(Q, [kJ])...
Paper I, Page 3, Line above Equation (7)	...was also added to.	...was also added to Q.
Paper II, Page 26, Table 3 caption	Equilibrium constants for reaction (R2)...	Equilibrium constants for the reverse of reaction (R2)...
Paper II, Table 4, value in the last row	-1.15199E+09	-1.146E+09
Paper II, Figure 8, y-axes	(J/kmol)	(kJ/mol)

For Paper IV, the readers are advised that some information will change during revision. The thesis has, however, the correct information with regard to this paper.

Abstract

In order to combat the effects of climate change, it is important to use a combination of solutions to achieve carbon neutrality as soon as possible. Carbon capture and sequestration is one such technology that can be used to significantly reduce the carbon footprint of many industrial plants. A mature technology for CO₂ capture, amine-based post-combustion capture, is readily available today. However, the economic cost associated with CO₂ capture plants constitutes a serious problem. Therefore, new systems are being developed in an attempt to reduce the cost of CO₂ capture. Non-aqueous systems and precipitating systems are among the new systems being considered.

Research in such systems is still relatively new, and it will be several years before they can be applied commercially. The somewhat ambitious aim of the work presented in this thesis was to accelerate research in these fields by concentrating on methodologies that can be used in any non-aqueous systems (precipitating or non-precipitating) and precipitating systems (aqueous or non-aqueous). Two main research questions were posed to this end: 1) How can non-aqueous systems be modelled? and 2) How can the crystallization kinetics for gas-liquid-solid systems be estimated? Methodologies required to answer these questions were developed and tested for the case of the amine, 2-amino-2-methyl-1-propanol (AMP), in the organic solvent, N-methyl-2-pyrrolidone (NMP). This is a non-aqueous system and leads to precipitation when AMP reacts with CO₂, i.e., it is also a precipitating system.

The system was modelled using an unsymmetric reference state of infinite dilution in water for ions. It was shown that using this for ions in non-aqueous solutions is thermodynamically valid, and it was applied to the AMP-in-NMP system. Experiments were performed to gain an understanding of the effect of equilibrium time, temperature, CO₂ loading, and amine concentration on the solubility of CO₂ in solution. These experiments were used to obtain the model parameters, and the model provided satisfactory predictions.

Regarding the crystallization kinetics, theoretical modifications to the semi-empirical power law relation are suggested in the cases of gas-liquid-solid equilibrium. The experimental procedure developed to estimate the crystallization kinetics was refined, and complications such as varying crystal structure are taken into consideration. The developed theory was assessed for the

AMP-NMP system. The saturation conditions for the system, required in assessing crystallization kinetics, were obtained using the thermodynamic model developed in this thesis. Although developed for the case of AMP in NMP, the methodologies presented here for modelling thermodynamic behavior and crystallization kinetics can be extended to other non-aqueous systems and precipitating systems, respectively.

సారాంశం (Summary in Telugu)

మన భూమి ఉష్ణోగ్రత రోజురోజుకీ పెరుగుతున్న మాట తెలిసిందే, తద్వారా, వాతావరణంలో అనేకమైన మార్పులు చేకూరుతాయని శాస్త్రజ్ఞుల అంచనా. ఈ సమస్యని ఎదుర్కోవడానికి ఏమీ చెయ్యకపోతే, క్రీ. శ. 2100 నాటికి ప్రపంచవ్యాప్తంగా వడగాల్సులు, వరదలు వంటి ప్రకృతి వైపరీత్యాలు తీవ్రతరమై జీవితాలపై ప్రభావం చూపించగలవు. రెండు వందల కోట్ల మందికి నీటి సదుపాయాలు కరువవ్వవచ్చు, భారతదేశానికి రెండింతలు సాగుభూమి వ్యవసాయానికి పనికిరాకుండా పోగలదు. ఇటువంటి తీవ్ర పరిణామాలు కొంత స్థాయికి తగ్గించడానికి ప్రపంచదేశాలన్నీ క్రీ. శ. 2015లో ప్యారిస్‌లో కలిసి పూనుకున్నాయి.

ఈ మార్పులకు గల కారణాలలో, బొగ్గు మరియు ఇతర ఇంధనాలను కల్పగా ఉత్పత్తయ్యే బొగ్గు పులుసు వాయువు (కార్బన్‌డాయాక్సైడ్, CO₂) ముఖ్యమైనది. విద్యుత్, సిమెంట్, స్టీలు, ఎరువుల ఉత్పత్తి కర్మాగారాలనుండి ఈ వాయువు వెలువడుతుంది. ఈ వెలువడు CO₂ని రసాయనికంగా ఎమైన్ మరియు ద్రావక మిశ్రమంతో బంధించవచ్చు. తదుపరి ఈ మిశ్రమాన్ని వేడిచెయ్యడం ద్వారా CO₂ని విడుదల చేసి, రసాయన పదార్థాన్ని పునరుపయోగించవచ్చు. విడుదల చేయబడిన CO₂ని భూమిలోకి లోతుగా పంపడం లేదా ఉపయోగపరచడం పరిష్కారాలలో ఒకటి.

ఈ రసాయన పద్ధతికి కావలసిన సాంకేతిక పరిజ్ఞానం ఇప్పటికే అందుబాటులో ఉన్నది. ఐతే ప్రస్తుత పరిజ్ఞానం చాలా ఖరీదైనది. ఉదాహరణకు, ప్రతి 100 యూనిట్ల విద్యుత్తుత్పత్తికీ, మరో 27 యూనిట్లు విద్యుత్తు కేవలం CO₂ బంధనకి అవసరం అవుతుంది. ఈ అదనపు ఖర్చు వల్ల, అవసరమైనప్పటికీ ప్రపంచదేశాలలో CO₂ బంధనాయత్నాలు అరుదయ్యాయి. CO₂ బంధనకి సంబంధించిన ఖర్చును తగ్గించడంకోసం, రసాయన మిశ్రమంలో మార్పులు వల్ల కలిగే ఆర్థిక ప్రయోజనాలపై పరిశోధన జరుగుతున్నది. ఈ తీరులోనే, నిర్జలీయ ద్రావకాలు కలిగిన రసాయన మిశ్రమాలు పరిశీలించబడుతున్నాయి. అట్టి కొత్త మిశ్రమాలు పారిశ్రామికంగా ఉపయోగించడానికి ముందు కంప్యూటర్‌లో కాలపాత నమూనాల తయారీ వంటివి అవసరం. ప్రస్తుతం జల సంబంధమైన ద్రావక మిశ్రమాల నమూనాలు మాత్రమే అందుబాటులో ఉన్నాయి. కాబట్టి, నిర్జలీయ మిశ్రమాలను నమూనీకరించు పద్ధతులు విపులీకరించవలసిన అవసరమున్నది. ఈ పరిశోధనా వ్యయంలో భాగంగా నిర్జలీయ మిశ్రమాల నమూనాలు చర్చించబడ్డాయి.

బంధనా ఖర్చులు తగ్గించే ప్రయత్నాలలోనే, CO₂ బంధన ద్వారా ద్రవ్య పదార్థం నుండి దృఢ పదార్థంగా మారు మిశ్రమాలు కూడా పరిశీలించబడుతున్నాయి. ఈ విధమైన CO₂ బంధనా పద్ధతులలో, మిశ్రమాన్ని రెండు భాగాలుగా చీల్చి, ఒక భాగంలో CO₂ని దృఢ పదార్థంగా గాఢపరచి, ఆ భాగాన్ని మాత్రమే వేడిచేయవచ్చు. తద్వారా, కొంత భాగాన్ని వేడిచెయ్యవలసిన

అవసరం లేకుండానే పునరుపయోగించవచ్చు, CO₂ బంధనకు సంబంధించిన ఖర్చు కొంతవరకూ తగ్గించవచ్చు. దృఢీకరణ జరుగు ఉపకరణము యొక్క కొలత సరిపూర్వకంగా, దృఢీకరణకి సంబంధించిన గతివేగం తెలుసుకోవడం అవసరం. లవణ పదార్థాలు ద్రావకాలలో దృఢీకరించు గతివేగం అంచనావేయు పద్ధతులు అందుబాటులో ఉన్నాయి. ఐతే, CO₂ బంధనా విధానాలలో వాయు పదార్థం కూడా ఉండడమూ, అలాగే మరిన్ని రసాయనిక ప్రతిక్రియలు చోటుచేసుకోవడం మూలంగా, ఈ పద్ధతులను ఉన్నదున్నట్లు వాడడం సాధ్యం కాదు. ఈ వ్యాసంలో, CO₂ బంధనా విధానాలలో తారసపడే దృఢీకరణ గతివేగం అంచనా వేయు పద్ధతి కూడా చర్చించబడింది .

ఈ పరిశోధనలో పైన తెలిపినటువంటి, నిర్జలీయ మిశ్రమాల కాల్యునిక నమూనాల తయారీ పద్ధతీ మరియు దృఢ పదార్థాల గతివేగ పరిశీలనా పద్ధతీ చూపబడినవి. ఈ పద్ధతులు చూపడానికి, 2-అమీనో-2-మిథైల్-1-ప్రోపనోల్ (2-amino-2-methyl-1-propanol) ఎమైన్‌ను N-మిథైల్-పైరోలిడోన్ (N-methyl-2-pyrrolidone) అను కార్బనిక (నిర్జల) ద్రావకాన్ని కలిపిన మిశ్రమం ఉదాహరణగా ఉపయోగింపబడింది. ఈ మిశ్రమం నిర్జలమైనదే కాక CO₂ని బంధించినప్పుడు కొంత దృఢ పదార్థ రూపం దాల్చును. కాబట్టి, రెండు పద్ధతులకూ ఉదాహరణగా ఉపయోగపడును. పరిశోధన ద్వారా అనుకూల ఫలితాలు లభించాయి.

Sammanfattning

Klimatförändring är ett problem som behöver hanteras brådskande. Om inget görs för att bekämpa detta problem, kan naturkatastrofer som värmeböljor och översvämningar öka över hela världen. Det kan också leda till att två miljarder människor kan ha svårt att få tillgång till vatten, och jordbruksytor, sammantagna dubbelt så stora som Indien, kan bli sårbara. Orsaken till denna klimatförändring är att koldioxid som produceras genom förbränning av kol och andra bränslen, har ökat mycket i atmosfären efter den industriella revolutionen. Koldioxiden kommer från bland annat kraft-, cement-, stål- och gödningsmedelsanläggningar. Genom en kemisk process kan majoriteten av dessa utsläpp förhindras. Processen baseras på att koldioxidmolekylerna i anläggningsutsläppen binds av amin i lösningsmedel. Därefter värms denna blandning av koldioxid, amin och lösningsmedel upp så att koldioxiden återvänder till gasform. Därigenom kan den frigjorda koldioxiden komprimeras och lagras i marken. Amin och lösningsmedel kan i sin tur återanvändas.

Det finns redan tillräcklig kunskap för att fånga koldioxid från industrier men den nuvarande teknologin är väldigt dyr. För att ett kolbaserat kraftverk med koldioxidavskiljning ska kunna hålla samma elproduktion som ett konventionellt kraftverk krävs det till exempel 27% extra energi. Därför är koldioxidavskiljning sällsynt i världen även om det behövs. Forskning pågår för att minska koldioxidavskiljningens kostnader. Inom denna forskning undersöks kemiska blandningar som innehåller organiska lösningsmedel. Sådana nya blandningar kräver skapande av virtuella modeller innan de kan användas industriellt. I nuläget finns det bara vattenbaserade modeller och därför behövs metoder för att kunna modellera icke-vattenbaserade (organiska) system. Att utveckla dessa metoder har varit ett av studieämnena för denna avhandling.

För att minska avskiljningskostnaden studeras dessutom lösningar där fällning äger rum vid koldioxidbindning. I dessa system går det att koncentrera koldioxid i fast form och separera det från lösningsmedlet. På så vis värms bara koncentrerad koldioxid upp, vilket minskar värmebehovet. För att kunna beräkna en lämplig storlek för – och designa – de enheter där fällningen ska ske, är det viktigt att mäta fällningshastigheten. För närvarande finns det metoder för fällningshastighetsmätningar endast för

system med salter i lösningsmedel. Fällningssystem för koldioxidavskiljning är dock mer komplexa eftersom de hanterar koldioxid i gasform. Därför har en ny mätningssätt för dessa system utvecklats i avhandlingen.

För att testa modellen för icke-vattenbaserade system, såväl som modellen för att mäta fällningshastighet, har lösningar med 2-amino-2-metyl-1-propanol använts i det organiska lösningsmedlet N-metyl-2-pyrrolidon. Det rör sig alltså om ett icke-vattenbaserat system och eftersom lösningen också bildar fällning när aminen binder koldioxid, kan samma system användas för att testa båda de utvecklade metoderna. Testen gav lovande resultat.

List of Publications

This thesis is based on the following four papers, which are referred to in the text by their roman numerals.

- I. Hanna K Karlsson, Meher G Sanku, Helena Svensson. In Press “Absorption of carbon dioxide in mixtures of N-methyl-2-pyrrolidone and 2-amino-2-methyl-1-propanol”, *International Journal of Greenhouse Gas Control*. doi: 10.1016/j.ijggc.2019.102952
- II. Meher G Sanku, Helena Svensson. 2019. “Modelling the precipitating non-aqueous CO₂ capture system AMP-NMP, using the unsymmetric electrolyte NRTL”, *International Journal of Greenhouse Gas Control* 89: 20-32. doi: 10.1016/j.ijggc.2019.07.006
- III. Meher G Sanku, Helena Svensson. 2017. “Crystallization kinetics of AMP Carbamate in solutions of AMP in organic solvents NMP or TEGDME”, *Energy Procedia* 114: 840-851. doi: 10.1016/j.egypro.2017.03.1226
- IV. Meher G Sanku, Helena Svensson. “Crystallization kinetics and the role of equilibrium in carbon capture systems with gas-liquid-solid equilibrium: Case study of AMP in NMP solution”, *Submitted*

My Contributions to the Publications

- I. I performed parts of the experimental work (more specifically, most of the experiments for determining Henry's parameters for CO₂ in NMP). I also evaluated the data resulting from the experiments I performed and wrote the corresponding parts of the paper. My co-authors wrote the rest of the paper. All authors took part in reviewing the finished manuscript.
- II. I was responsible for the development of the methodology used. I performed the regression, thermodynamic modelling, and the corresponding evaluation of results. I also wrote and reviewed a major part of the paper.
- III. I was responsible for the application of existing concepts and methodology to our system. I took part in designing the experiments with my co-author. I evaluated the experimental data and wrote major parts of the paper. All authors took part in reviewing the finished manuscript.
- IV. I was responsible for the conceptualization and development of the methodology used. I performed the experimental work and evaluated the corresponding results. I also wrote the paper and reviewed a major part of the paper.

Other publications

I have also contributed to the following publications, which are not part of this thesis:

1. Wuyin Wang, Meher G Sanku, Hanna K Karlsson, Christian Hulteberg, Hans T Karlsson, Michael Balfe, Olaf Stallmann. 2017. “Medium temperature desulfurization for oxyfuel and regenerative calcium cycle” *Energy Procedia* 114: 271-284. doi: 10.1016/j.egypro.2017.03.1169
2. Meher G Sanku, Hanna K Karlsson, Christian Hulteberg, Wuyin Wang, Olaf Stallmann, Hans T Karlsson. 2019. “Kinetic evaluation of lime for medium temperature desulfurization in oxy-fuel conditions by dry sorbent injection” *Energies* 12: 2645-2661. doi: 10.3390/en12142645

Acknowledgements

Several people have played pivotal roles in the completion of this thesis. Although it would be impossible to name them all here, I would like to express my gratitude to some of them.

I begin by thanking my trio of supervisors in the chronological order that I worked with them: Assoc. Prof. Christian Hulteberg, for always giving me the freedom to make my own mistakes and yet being prepared to put out the fire if need be; Prof. Hans T. Karlsson, for inspiring me to explore the language of equations, which I now plan to make part of my life; and Sr. Lect. Helena Svensson, for being not just a supervisor, but also a mentor, for inspiring fundamental changes in me and, most of all, for all the running metaphors that I still keep in mind to handle stress. I could not have asked for a better combination of supervisors, and I appreciate every moment of every discussion we've had during the period of my PhD studies.

I would also like to thank all my colleagues at the Department of Chemical Engineering at LTH for making this time so much fun, and for inculcating a work culture with high standards. I would like to extend special thanks to Hanna K. Karlsson for her optimism, humor, and philosophical discussions during the course of our work together. Special thanks also to my office mate, Omar Abdelaziz, for always finding the time to proofread an article, to listen to my ideas, or for just letting me vent my frustration, even during his busiest times. I also thank everybody at floor +1 and -1 for being there during my hardest times and sharing so many fun memories during this long journey.

While several people have sparked an understanding that eventually led to the solution of problems that arose during my PhD studies, a few have been key in methodologically solving problems, and I would like to acknowledge them here: Assoc. Prof. Kaj Thomsen at DTU, for valuable discussions on electrolyte thermodynamics, Dr. Ugochukwu Aronu at SINTEF, for our exchange of ideas and discussions on crystallization processes, and Prof. Jens-Petter Andreassen at NTNU, for a systematic discussion on crystallization kinetics. I would also like to thank the staff of SINTEF for all those thought-provoking lunch discussions on pilot plant behavior, that have added an extra dimension to my research. I would also like to mention Herman Kolderup at SINTEF for being such a cozy office mate during my exchange there.

I also want to express my deep gratitude to M. Srinivas sir and Prof. R. P. Vaid, for helping me see the beauty in mathematics and chemical engineering thermodynamics, respectively. I would also like to thank my family and friends in India and in Sweden for all their support during these years.

Finally, I would like to thank the two most important people in my life: Meher Baba and my husband, Karl-Oskar Mogenfelt, the former for being the equilibrium point I aspire to reach and the latter for being the catalyst that inspires me to get there faster.

*If we knew what it was we were doing,
it would not be called research, would it?*

-Albert Einstein

Contents

1	Introduction	1
1.1	Post-combustion capture in the context of this thesis.....	3
1.2	Research questions	4
1.3	Outline	5
2	The State of the Art	9
2.1	Non-aqueous systems and water-lean systems	14
2.2	Phase-change systems	17
2.3	The system studied in this work: AMP-NMP	20
3	Solubility Experiments	23
3.1	Materials and Methods	24
3.1.1	Materials	24
3.1.2	Solubility of CO ₂ in AMP-NMP solutions	24
3.1.3	Solubility of the salt in AMP-NMP solutions	26
3.2	Results and Discussion	28
3.2.1	Solubility of CO ₂ in AMP-NMP solutions	28
3.2.2	Solubility of the salt in AMP-NMP solutions	32
4	Modelling Non-aqueous Systems	37
4.1	Theory	37
4.1.1	Chemical reaction thermodynamics	39
4.2	Thermodynamic property model	43
4.3	Discussion	49
5	Crystallization Kinetics for Precipitating Systems	55
5.1	Theory	55
5.1.1	Traditional power law kinetics	57
5.1.2	Proposed power law kinetics	59
5.2	Experimental procedure.....	61
5.3	Results and Discussion	63
6	Conclusions	73
7	Future work	77
	References	79

Abbreviations and Symbols

Abbreviations

0AN	Pure NMP
0AT	Pure TEGDME
15AN	15wt% AMP in NMP
15AT	15wt% AMP in TEGDME
2.5AT	2.5wt% AMP in TEGDME
25AN	25wt% AMP in NMP
AMP	2-amino-2-methyl-1-propanol
BECCS	Bioenergy with CCS
CCS	Carbon capture and sequestration
DAC	Direct air capture
DEEA	2-(diethylamino)ethanol
IPCC	Intergovernmental Panel on Climate Change
IEA	International Energy Agency
MAPA	3-(methylamino)propylamine
MEA	Monoethanol amine
MFC	Mass flow controller
MSW	Meta-stable zone width
NAS	Non-aqueous system
NMP	N-methyl-2-pyrrolidone
rrmse	Residual root mean square error
TEGDME	Triethylene glycol dimethyl ether
WLS	Water lean system

Latin symbols

(CO_2)	Amount of CO_2
a	Activity
A	Non-randomness factor (NRTL)
c	Molality (per kg of NMP)
g	Amount of a substance (usually CO_2) in the gas phase
H	Henry's constant
K	Equilibrium constant
k	"Rate constant" in the traditional power law relation
k'	"Rate constant" in the proposed power law relation
M	Molecular weight
m	Precipitation in moles/kg NMP
n	Amount in moles
p	"Order of reaction" in the traditional power law
p'	"Order of reaction" in the proposed power law
Q	Heat duty
R	Universal gas constant
S	Supersaturation ratio
T	Temperature
V	Volume
W	Work
w	Weight
x	Mole fraction

Mixed symbols

c_0	1 mol/kg NMP
c_{CO_2}	Molality of physically dissolved CO_2
c^S	Molality of dissolved salt at saturation conditions
$-\frac{dT}{dt}$	Cooling rate

P_{CO_2}	Partial pressure of CO ₂
$\ln S_a$	MSW in terms of activity
Δc	MSW in terms of concentration
ΔG	Change in Gibbs free energy
ΔH	Change in enthalpy
ΔT	MSW in terms of temperature
η_{th}	Thermodynamic efficiency
$\eta_{turbine}$	Turbine efficiency

Greek symbols

α	CO ₂ loading
γ	Activity coefficient
Δ	Change
ε	Dielectric constant
μ	Chemical potential
ν	Stoichiometric coefficient
σ	Relative supersaturation
τ	NRTL interaction parameter

Coefficients

a, b	Dielectric constant
A_H, B_H, C_H, D_H	Henry's parameter
$a_{ij}, b_{ij}, e_{ij}, f_{ij}$	NRTL binary interaction parameter
A_K, B_K	Equilibrium constant
A_S, B_S	Molality of the dissolved salt
c_{ij}, d_{ij}	NRTL non-randomness factor
$C_{m,ca}, D_{m,ca}, E_{m,ca}$	ENRTL molecule-ion pair interaction parameters
$C_{ca,m}, D_{ca,m}, E_{ca,m}$	ENRTL ion pair-molecule interaction parameters

Subscript

1	Reaction {13}
2	Reaction {11}

+	Protonated amine ion
–	Carbamate ion
±	Salt or mean ionic property
(<i>aq</i>)	In water
(<i>NMP</i>)	In solvent NMP
(<i>l</i>)	Pure liquid
(<i>sol</i>)	In solution
<i>a</i>	Activity basis
<i>abs</i>	Absorption
<i>AMP, 0</i>	Initial AMP
<i>aq</i>	Water
<i>c</i>	Concentration basis
<i>comp</i>	Compression to 15MPa
<i>CO₂sep</i>	CO ₂ separation
<i>CO₂sep + comp</i>	CO ₂ separation and compression to 15MPa
<i>i</i>	Component <i>i</i>
<i>ij</i>	Component <i>i</i> -component <i>j</i>
<i>in</i>	Into the reactor
<i>m, ca</i>	Molecule <i>m</i> -ion pair (<i>c, a</i>)
<i>min</i>	Minimum
<i>mix</i>	Mixture
<i>NMP</i>	NMP
<i>phase</i>	Phase change
<i>pump</i>	Pumping
<i>reb</i>	Reboiler
<i>ref</i>	Reference
<i>reg</i>	Regeneration
<i>rxn</i>	Reaction
<i>S</i>	Solvent

sens Sensible
vap vaporization

Superscript

* unsymmetric reference state
 ∞ Infinite dilution
0 Pure component reference state
0, s Pure component solid reference state
Born Born term contribution
id ideal
local local or short-range interactions
m molality scale
PDH long range interactions
s saturation

1 Introduction

The carbon content in the atmosphere has been increasing since the Industrial Revolution. The concentration of CO₂ in the atmosphere is currently above 400 ppm, compared to 280 ppm before the Industrial Revolution (Riebeek, 2011). If CO₂ emissions are allowed to increase at the current rate, the average temperature of the world will have increased by 5 °C by 2100, compared to the pre-industrial baseline period of 1861-1880 (Intergovernmental Panel on Climate Change (IPCC), 2013). It is believed that such an increase will have drastic consequences, such as heat waves and flooding affecting 12 billion people and 120 million people per year, respectively, difficulties in accessing water for two billion, a reduction in the land available for agriculture equivalent to an area more than twice the size of India, as well as many other serious consequences (AVOID2, 2019; IPCC, 2013). Two main long-term goals were set out in the Paris Agreement of 2015. The first is to limit the increase in global average temperature to well below 2 °C (compared to pre-industrial levels), and the second is to eventually achieve carbon neutrality by the end of the century (European Commission, 2015a; United Nations Framework Convention on Climate Change, 2015). Limiting the global average temperature increase to below 2 °C could decrease the number of people effected by heat waves, flooding and water scarcity by 89%, 76% and 26%, respectively. The cropland decline could also be decreased by 41% (AVOID2, 2019; IPCC, 2018a).

This 2 °C limit corresponds to a carbon budget of approximately, 1000 Gt carbon, or 2900 Gt CO₂ emitted into the atmosphere (IPCC, 2018b). About 77% of this carbon budget had already been used by the end of 2019. At the current CO₂ emission rate, it may take only about 17 years before the other 23% has been used (The Guardian, 2017; International Energy Agency (IEA), 2019a; IPCC, 2018b). By reducing the rate of CO₂ emissions, the time taken to use up the carbon budget for the 2 °C limit could be extended. Once this budget is used up, the emissions must go down to zero. To achieve the reduced and eventual zero carbon emissions, low-carbon and negative carbon emission technologies are required in highly carbon-emitting industries. Carbon capture and sequestration (CCS) is one such technology, necessary, in combination with other technologies.

About 80% of the world's primary energy comes from fossil sources (IEA, 2019b). To achieve CO₂ neutrality, investments in coal, oil and natural gas need to be diverted to low-carbon energy sources (Carbon Tracker Initiative, 2017),

CCS must be used when combusting fossil fuels, and other means of reducing atmospheric CO₂ must be employed, for example, afforestation. If CO₂ emissions are avoided by not exploiting or combusting fossil fuels, or if CO₂ is captured by means of afforestation, fossil resources and forested regions would have to remain untouched for more than several millennia to have any significant impact (IPCC, 2018c). This would be very difficult given the number of factors that can influence such measures. On the other hand, permanent storage of CO₂ using CCS technologies is possible for long periods, i.e., several millennia, just as crude oil has been stored for several millennia before human intervention (Consoli and Wildgust, 2017).

It has been estimated that in 2015 there were about 11 000 Gt CO₂ equivalent fossil fuel reserves around the world, which, if exploited would lead to overshoot in the carbon budget set for the 2 °C limit (IPCC, 2018c; Jakob and Hilaire, 2015). If there is an overshoot due to a delay in the introduction of low-carbon technologies, negative-emission technologies will become crucial in removing the excess CO₂ if we are to achieve the 2 °C limit. Negative emission can be achieved using technologies such as direct air capture (DAC) (Climeworks, 2019) or bioenergy with CCS (BECCS) (Newton-Cross and Gammer, 2016), which can also act as carbon sinks for unavoidable emissions such as those from agriculture. Both DAC and BECCS would be derived from CCS technologies that must be implemented immediately.

The cement and steel industries together represent 12 to 14% of global CO₂ emissions (IEA, 2013), and CCS must be employed in these industries to achieve carbon neutrality. CO₂ emissions from the cement industry are largely the result of fuel combustion in the rotary kilns and the release of CO₂ from limestone. Fly ash from coal-fired plants and slag from steel making can be used to replace some of the limestone used in the cement industry, which will reduce CO₂ emissions (IEAGHG, 2013a). There has also been some development of techniques to produce low-carbon cement (Solidia, n.d.). However, this is not sufficient to achieve net zero carbon emissions. The IEA has estimated that the lowest cost pathway to meet the 2 °C limit would require CCS at 20-30% of the world's cement facilities by 2050, and at most facilities after 2050 to achieve carbon neutrality (IEA, 2013).

Carbon emissions in the steel-making industry result from the reduction of iron ore using coke to produce raw iron and CO₂. The use of recycled scrap metal reduces emissions, but CCS is necessary for carbon neutrality if reduction with coke is continued (IEAGHG, 2013b). The reduction of iron ore with renewable hydrogen instead of coal has recently been gaining ground. This would allow steel to be produced with almost zero carbon emission, without the need for CCS. The construction of a pilot plant employing this technology started in Sweden in 2018 (HYBRIT, n.d.). Other industries, such as the fertilizer industry, natural gas

processing and hydrogen production (non-renewable) in oil refineries all require CCS to become near carbon neutral.

The energy sector includes power generation for industry, district heating and fuel for transport. District heating and transport give rise to numerous small CO₂ emissions that can be difficult to capture. Other methods of handling these dispersed CO₂ emissions have therefore been suggested, such as electrification and large-scale hydrogen production. The production of hydrogen from fossil sources and biological sources can be combined with CCS to achieve near-zero emissions and negative emissions, respectively. Electrification would require more power generation. Decarbonization of power generation could be achieved by increasing the amount of renewable energy resources and by using technologies with improved energy efficiency. However, renewable energy cannot always be instantly supplied throughout the whole year. To supply it on demand, capital-intensive production and storage infrastructure would have to be distributed widely in order to overcome the seasonal nature of renewables. It has therefore been suggested that depending completely on renewable resources might be too costly (Clack et al., 2017; Heard et al., 2017; Temple, 2018). This suggests that some dependence on nuclear power, biomass or fossil energy may be inevitable (IPCC, 2018c).

To summarize, in order to avoid drastic changes in the climate, the amount of CO₂ in the atmosphere has to be reduced. Undisturbed storage of the CO₂ removed is possible with CCS for several millennia. Negative emission technologies that must be employed in the case of an overshoot of the carbon budget for the 2 °C limit will also be based on current CCS technologies. CCS is necessary in the cement industry, while in steelmaking, reduction by hydrogen is the only future technology with the potential to be almost carbon neutral without CCS. Alternatives to CCS exist in the energy sector, however, it might be necessary to combine these technologies with fossil-based energy production, where CCS will be necessary to achieve carbon neutrality. Post-combustion carbon capture by liquid absorption is the most mature technology available for the capture part of CCS.

1.1 Post-combustion capture in the context of this thesis

Aqueous solutions of monoethanol amine (MEA) have been studied thoroughly and commercially for carbon capture. However, the cost of capture is rather high. The total equivalent work required in aqueous MEA systems is about 800-1000 kJ/kg CO₂ separated (Budzianowski, 2017a; Svendsen et al., 2011; Zhang et al., 2015). The minimum work i.e., the work required if there was no work lost in the

capture process, has been calculated for an inlet containing 13% CO₂, for 90% capture at 45 °C, to obtain a final CO₂ purity of 98%. For an actual work of 975 kJ/kg CO₂ separated, a thermodynamic efficiency (minimum work/actual work) of about 16% is achieved. Under these conditions, the aqueous MEA system would use 27% of the electricity delivered by the power plant to capture the CO₂ produced (Budzianowski, 2017a). While currently available technologies should be implemented immediately to mitigate climate change, improved CCS technologies will be required in the future.

The reboiler duty required to regenerate the amine accounts for about 90% of the cost of CO₂ separation (Budzianowski, 2017a). To reduce the energy consumption in the reboiler, novel systems such as non-aqueous systems and phase-change systems (either liquid-liquid splitting or solid-liquid splitting systems) are being studied. A demonstration project has already been carried out for liquid-liquid splitting systems by iCAP for aqueous solutions of 2-(diethylamino)ethanol (DEEA) and 3-(methylamino)propylamine (MAPA), showing a thermodynamic efficiency of 25% (with a work equivalent of 630 kJ/kg CO₂ separated), i.e., much better than the 16% for aqueous MEA (Budzianowski, 2017a, 2017b; European Commission, 2015). This illustrates the potential of novel technologies. Other novel technologies such as non-aqueous systems and solid-liquid splitting systems are yet to be studied at a level that facilitates calculating thermodynamic efficiency. In this thesis, it is attempted to accelerate research in these fields.

1.2 Research questions

Research in the fields of non-aqueous systems (precipitating or non-precipitating) and precipitating systems (aqueous or non-aqueous) face several challenges. Moving from aqueous to non-aqueous systems affects the methods used to design and assess various aspects of the capture plant (as explained in Chapter 2). Precipitation also adds an extra level of complexity to the capture plant that must be well-understood (as discussed in Chapter 2). The work described in this thesis concerns novel systems, more specifically, non-aqueous systems and solid-liquid splitting systems, and is a continuation of previous research at the Department of Chemical Engineering at Lund University (Svensson, 2014). Theoretical and methodological gaps were identified and addressed in an attempt to further research in the fields of non-aqueous systems and precipitating systems. The main research question was therefore formulated as follows:

What methodologies need to be developed to accelerate research in the fields of non-aqueous systems and precipitating systems for carbon capture?

Knowledge gaps in these fields have been identified as modelling for the field of non-aqueous systems, and developing a theory for the crystallization kinetics in the case of precipitating systems (i.e., systems with a gas-liquid-solid equilibrium). The above research question was thus broken down into two questions:

RQ1. How can non-aqueous systems be modelled?

RQ2. How can crystallization kinetics for gas-liquid-solid systems be estimated?

Throughout this work, a non-aqueous precipitating system of the amine 2-amino-2-methyl-1-propanol (AMP) in the non-aqueous solvent N-methyl-2-pyrrolidone (NMP) was used as a model system to which the methodologies developed were applied.

1.3 Outline

This thesis summarizes the work described in 4 papers aimed at answering the above research questions as outlined in Table 1.1. Chapter 2 describes the state of the art in current and future technologies for carbon capture (i.e., non-aqueous systems and phase-change systems). Some of the knowledge gaps in novel technologies (modelling of non-aqueous systems and crystallization kinetics for precipitating systems) are presented and the system considered, AMP in NMP, is also introduced in Chapter 2. Chapter 3 describes the experiments performed to determine CO₂ solubility in the AMP-NMP solutions (Papers I and IV), which were used in modelling the system (Papers II and IV). Chapter 3 also summarizes the experiments performed to determine the solubility of the precipitate in the solution (Paper III), which was used to apply existing theories for crystallization kinetics to the system (Paper III).

Chapter 4 describes the methodology used for modelling non-aqueous systems and the results obtained. It also suggests a better way of determining the solubility of the salt in the system used. This chapter concentrates mainly on answering RQ1, and provides information about solubility that is valuable in answering RQ2. Paper I presents the experimental data needed for the method developed for modelling in Paper II, which addresses RQ1. Paper IV also contributed to answering RQ1 by updating the model, which is discussed in Chapter 4. Chapter 5 summarizes parts of Papers III and IV, which describe the crystallization kinetics theory, and the method and experiments adapted for systems with gas-liquid-solid equilibrium used to answer RQ2. The conclusions drawn from this work are presented in Chapter 6, and future work is discussed in Chapter 7.

Table 1.1. Outline of this thesis.

Chapter	RQ1	RQ2
2	Knowledge gap identified	Knowledge gap identified
3	Paper I, part of Paper IV Experiments used to answer RQ1	Part of Paper III Experiments used to obtain the solubility information required to answer RQ2
4	Paper II, part of Paper IV Methodology and results required to answer RQ1	Part of Paper IV Solubility results from the model used to answer RQ2
5	Paper IV Another application of the model in addition to answering RQ1	Paper III, IV Methodology and results required to answer RQ2

When more than one kind of experimental method has been used for the same purpose, each kind has been given a specific name to avoid confusion. Figure 1.1 displays some of the terms used in this thesis to refer the different experiments. For example, in Chapter 3, two kinds of experiments have been performed to measure solubility of CO₂ in AMP-NMP solutions. They have been consistently referred to as first *type* and second *type* of experiments. In Chapter 5, two kinds of experiments were performed to determine crystallization kinetics which are referred to as first *set* and second *set*. The word *series* has been consistently used to refer to experimental runs in a closed system where energy was exchanged, but there was no mass flow into or out of the reactor after a pre-defined condition was reached. The pre-defined condition is the CO₂ loading of the solution shown in brackets for every series in the figure. An experimental series with CO₂ loading of 0.62, for example, refers to an experimental run where the reactor was injected with CO₂ until a loading of 0.62 was reached, after which, the temperature in the reactor was increased or decreased but there was no more material exchange into or out of the reactor.

Figure 1.1 also shows the data flow between the different experiments performed, the thermodynamic models and the crystallization kinetics models. For example, the second type of experiments performed to determine the solubility of CO₂ in the AMP-NMP solutions were conducted together with the second set of experiments performed to obtain the crystallization kinetics. The results of the solubility of CO₂ experiments mentioned above were used to create the second model, that was also used in the determination of the crystallization kinetics. Finally, the proposed theory, i.e., the theory developed herein, was applied to get the crystallization kinetics in this case.

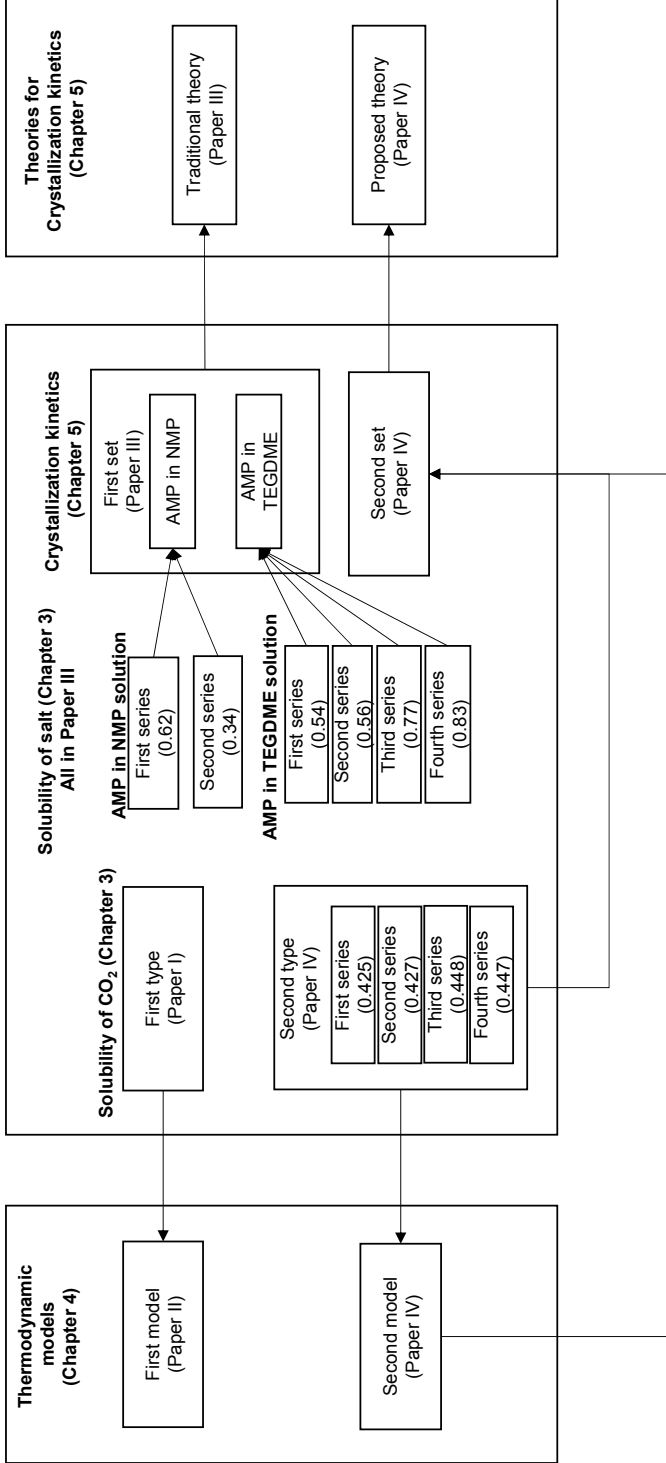
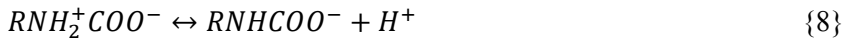


Figure 1.1. Data flow between the different experiments performed, the thermodynamic models and the crystallization kinetics models.

2 The State of the Art

The established benchmark for CCS applications is a 30wt% aqueous solution of MEA. A new benchmark, aqueous solution of AMP and piperazine, has recently been proposed (Cousins et al., 2019). However, the aqueous solution of MEA is referred to as the benchmark in this thesis since this is the benchmark used in the papers. The reaction mechanism proposed for an aqueous MEA solution is as follows (Puxty and Maeder, 2016):



A typical CCS plant is shown in Figure 2.1. The flue gas stream from a CO₂-emitting source is sent to a water-wash tower to cool the stream to the absorption temperature of the plant. A flue gas blower may be needed to compensate for pressure loss in the CCS plant. The CO₂ in the flue gas stream is absorbed in the aqueous MEA solution. The cleaned flue gas is processed in a water-wash tower to remove any amine emissions from the absorption column before the remaining gas is vented to the atmosphere. The CO₂-rich stream exiting the absorption column is pumped through a lean/rich cross heat exchanger and then to the regeneration column. The CO₂ is separated from the amine in the regeneration column by applying additional heat. Water vapor is produced in the process, which is condensed before the CO₂ is sent to compression and sequestration. The lean stream is pumped through the cross heat exchanger to extract as much of the

sensible heat as possible, which is then recycled to the absorption column. Some of the amine degrades over time and is removed in the reclaimer. Amine is added to compensate for the amount removed (Liang et al., 2011; Svendsen et al., 2011; Wang et al., 2011).

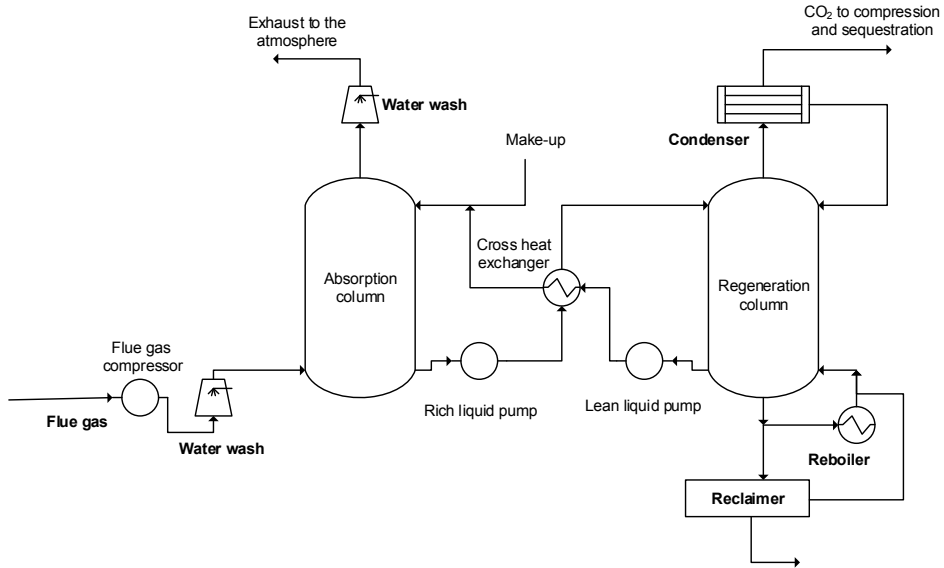


Figure 2.1. Process flow diagram for a typical CCS plant, drawn based on information in literature (Liang et al., 2011; Svendsen et al., 2011; Wang et al., 2011). The process units and streams effected by changing to non-aqueous systems are shown in bold.

The heat input required for regeneration, ΔH_{reg} , to desorb the CO_2 from a loaded aqueous MEA solution is given by Equation (2.1).

$$\Delta H_{reg} = \Delta H_{rxn} + \Delta H_{vap} + \Delta H_{sens} \quad (2.1)$$

The heat of reaction, ΔH_{rxn} , at the regeneration temperature must be supplied to reverse the CO_2 amine reactions in Reactions {1} to {8}. This depends on the amine used and the reaction mechanism. The heat of vaporization, ΔH_{vap} , is the heat supplied to vaporize the solvent, usually water, in the solution, which then acts as a stripping agent and allows operation at higher pressure. The sensible heat, ΔH_{sens} , is the heat required to increase the temperature of the rich stream to that of the regeneration column.

The performance of a process or a system is, in literature, expressed either in terms of heat duty, equivalent work or thermodynamic efficiency. Additionally, the performance can be evaluated for CO_2 separation or CO_2 separation plus subsequent compression to 15 MPa. To be able to compare these different values, it is important to understand the relation between the different terms, as in Equations (2.2) to (2.6):

$$W_{reb} = Q_{reb} \eta_{turbine} \frac{(T_{reb} + \Delta T_{reb} - T_{sink})}{T_{reb} + \Delta T_{reb}} \quad (2.2)$$

$$W_{CO_2sep} = W_{pump} + W_{reb} \quad (2.3)$$

$$W_{CO_2sep+comp} = W_{pump} + W_{comp} + W_{reb} \quad (2.4)$$

$$\eta_{th} = \frac{W_{min}}{W_{actual}} \quad (2.5)$$

$$W_{lost} = W_{actual} - W_{min} \quad (2.6)$$

where Q_{reb} and W_{reb} are the reboiler heat duty and the corresponding work equivalent, $\eta_{turbine}$ is the turbine efficiency, T_{reb} is the reboiler temperature, ΔT_{reb} is usually 5-10 °C, and T_{sink} is the temperature of the sink. W_{CO_2sep} is the work equivalent for the separation of CO₂, which includes the regeneration work (W_{reb}) and the pumping work (W_{pump}) through the plant. The regeneration work is usually about 90% of the total work in the plant, therefore, W_{reb} and W_{CO_2sep} are used interchangeably in this thesis. $W_{CO_2sep+comp}$ is the work that includes the separation work (W_{CO_2sep}) and the work required to compress the CO₂ to the pressures required for sequestration (W_{comp}). It is therefore greater than W_{CO_2sep} for the same system. W_{actual} could be equal to W_{CO_2sep} or $W_{CO_2sep+comp}$, depending on which aspects of CCS are taken into account. η_{th} is the thermodynamic efficiency, discussed in Section 1.1.

The work equivalent, 630 kJ/kg CO₂ separated, in the case of aqueous DEEA-MAPA system discussed in Section 1.1, corresponds to a heat duty of 2400 kJ/kg CO₂ separated (Budzianowski, 2017a). If the W_{pump} in Equation (2.3) is ignored and all the other terms in Equations (2.2) are assumed to be the same between the aqueous DEEA-MAPA system and aqueous MEA system, the work equivalent of 800-1000 kJ/kg CO₂ separated (discussed in Section 1.1) for aqueous MEA can be translated to a heat duty of 3000-3900 kJ/kg CO₂ separated.

A considerable proportion of the heat input to the plant is lost in the condenser and the cross heat exchanger (Lin and Rochelle, 2016). Advanced absorber and stripper configurations have been proposed to minimize this loss. Worth noting among advanced stripper configurations are the stripper with lean vapor compression and the advanced flash stripper configurations. In the stripper configuration with lean vapor compression, shown in Figure 2.2, the hot lean stream is flashed at a lower pressure and the vapor obtained is re-compressed and sent to the bottom of the stripper. The liquid part sent to the cross heat exchanger is cooler resulting in a cooler rich stream entering the regeneration column and, therefore, higher portion of the sensible and the latent heat is recovered at the top of the stripper. The carbon capture unit at the SaskPower Boundary Dam Power

Station in Canada uses an aqueous amine solution in the absorption column with lean vapor compression in the stripper, allowing the heat duty to be reduced to 2000-2500 kJ/kg CO₂ separated (Rochelle, 2016). This is much lower than the 3000-3900 kJ/kg CO₂ separated for the aqueous MEA system with simple stripper configuration. While part of the reduction in heat duty could be a result of the proprietary amine used, part of it is a result of the stripper configuration.

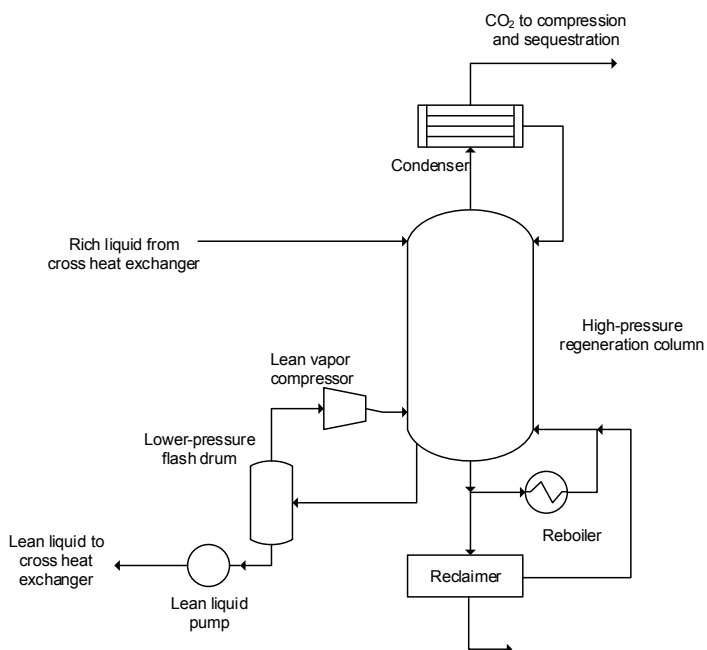


Figure 2.2. Process flow diagram for a regeneration column with lean vapor compression, drawn based on information in literature (Rochelle, 2016).

In an advanced flash stripper, shown in Figure 2.3, a cold rich bypass stream is separated from the rich stream leaving the absorption column (before the cross heat exchanger), which is used to recover latent and sensible heat from the vapor outlet of the stripper. The rest of the rich stream is heated in a cross heat exchanger. A warm rich bypass stream is separated again, and sent to the top of the stripper, while the rest of the rich stream is heated to the required temperature in another cross heat exchanger, and possibly heated further in a steam heater before entering the stripper. By varying both the cold and warm rich bypass streams it is possible to recover practically all the heat in the stripper overhead (Lin and Rochelle, 2016; Rochelle, 2016). Based on the results from (Van Wagener and Rochelle, 2011), the thermodynamic efficiency of 16% for aqueous MEA system discussed in Section 1.1, corresponds to a simple stripper configuration such as that shown in Figure 1.1. An advanced flash stripper configuration with piperazine system has been reported to have 74% thermodynamic efficiency (Lin and Rochelle, 2016). The only problem when

using an advanced flash stripper is the capital cost associated with the additional equipment (Rochelle, 2016).

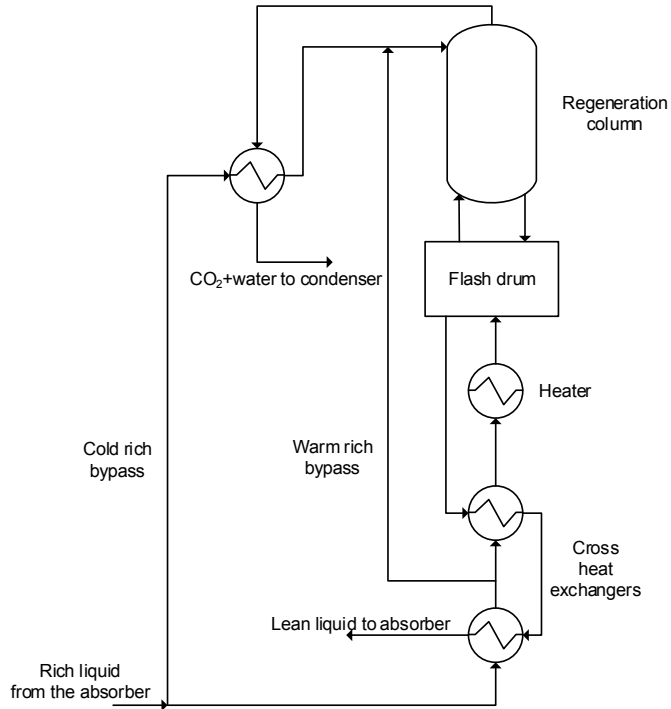


Figure 2.3. Process flow diagram for an advanced flash stripper, drawn based on information in literature (Rochelle, 2016).

While the research described above concerned recovering the heat expended, other research in the field has been focused on reducing individual terms in Equation (2.1) using novel systems. The heat of vaporization can be drastically reduced by avoiding or reducing the amount of water in the solution. Such solutions are called non-aqueous solutions or water-lean solutions. Another way to reduce the regeneration heat is by using phase-change systems, where the CO_2 -loaded stream undergoes either solid-liquid splitting or liquid-liquid splitting. Only the CO_2 -rich stream of the split is then regenerated, leading to a much lower sensible heat and vaporization heat requirement in Equation (2.1). The demonstration plant run by iCAP, discussed in Section 1.1, employs such a phase-change system with liquid-liquid splitting. It is likely that novel systems, such as non-aqueous or phase change systems, used in combination with advanced stripper configurations, would lead to improved energy efficiency. These novel systems are the topic of this thesis, and are discussed further in the following sections.

2.1 Non-aqueous systems and water-lean systems

As mentioned above, the heat of vaporization can be minimized by replacing all or part of the water solvent. Such systems are referred to below as non-aqueous systems (NASs) and water-lean systems (WLSs). These terms refer to the initial state of the solutions, i.e., a NAS initially contains no water (but might accumulate water), while a WLS initially contains some water. The term NAS is sometimes used in the literature to refer to hydrophobic organic solutions (Heldebrant et al., 2017a), i.e., not the definition used here.

Apart from minimizing the heat of vaporization, the sensible heat can also be affected by changing the solvent in the system. Furthermore, the organic solvents in NASs tend to have higher physical solubility for CO₂ than water, which leads to faster rates of absorption (Heldebrant et al., 2017b; Mota-Martinez et al., 2017). NASs are yet to be demonstrated at a pilot scale. However, preliminary results were obtained from simulation, which showed that NASs can have a reboiler heat duty as low as 1700 to 2500 kJ/kg CO₂ separated. The same simulation showed that the benchmark, 30wt% MEA solution, has a reboiler duty of 3680 kJ/kg CO₂ separated, which is in the range of 3000 to 3900 kJ/kg CO₂ separated as discussed above in this chapter (Heldebrant et al., 2017b; Lail et al., 2014).

Using new non-aqueous solvents is not without challenges. Among others, these include changes in the plant design to suit the organic solvents, including absorber packing. The components where an NAS might present challenges are indicated in boldface in Figure 2.1. The main drawback of NASs is associated with the presence of unavoidable water. The flue gas that enters the CCS unit tends to contain some water vapor. The temperature of the flue gas is usually lowered in the water-wash tower. The processing of the gas stream exiting the absorption column is also performed in a water-wash tower. Moreover, the emissions from the absorption column may not only be the amine but also the organic solvent that is being used to replace the water as solvent. Additionally, reclamation may need consideration from a process design point of view due to the change in reaction mechanism for CO₂ capture, as well as the presence of new compounds. A deeper understanding of the changes in several physical and chemical properties of the solvents in the presence and absence of water is therefore needed.

Lean loading and stripper pressure are related to the amount of water vapor in the gas stream of the regeneration unit for the aqueous MEA system. As can be seen from in Figure 2.4, the partial pressure of CO₂ at a desorption temperature of 120 °C and a lean loading of, for example, 0.2, is quite low (about 15 kPa) for aqueous MEA. Such low partial CO₂ pressures are impossible for this system at high pressures and low lean loadings without a stripping agent such as water. If water vapor is present in addition to the 15 kPa of CO₂, CO₂ desorption could take place,

at least at atmospheric pressure, and the water vapor could be condensed afterwards. In the absence of water, either the lean loading would have to be much higher, or the stripper pressure would have to be much lower. It is preferable to operate the regeneration column at high pressures as it leads to much lower compression work downstream (Lin and Rochelle, 2016).

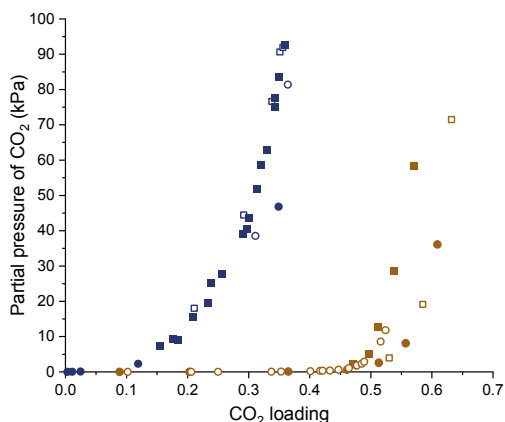
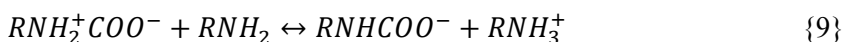


Figure 2.4. The solubility of CO₂ in aqueous MEA solutions at 40 °C (brown symbols) and 120 °C (blue symbols). The data were taken from: ●, ● = Jou et al., (1995), □, □ = Tong et al., (2012), ○, ○ = Aronu et al., (2011), ■ = Shen and Li, (1992), and ■=Ma'mun et al., (2005).

The behavior shown in Figure 2.4 could be altered by changing the solvent since the reaction mechanism could change with the solvent. In an NAS of MEA, where the organic solvent does not participate in any reaction with the amine or CO₂, the reaction mechanism could include Reactions {7} and {9}.



In Figure 2.5, the solubility of CO₂ in MEA-NMP system is shown. It can be seen from Figure 2.5 that the partial pressure of CO₂ at a desorption temperature of 120 °C and a lean loading of 0.2 is about 60 kPa, which is much higher than the 15 kPa observed for aqueous MEA system in Figure 2.4. However, to operate at atmospheric pressure with a lean loading of 0.2, this system would still need a stripping agent that can contribute ~40 kPa of partial pressure. It is important to consider this requirement when designing an NAS. In this regard, research is ongoing in the development of other low-energy stripping technologies (Wang et al., 2017).

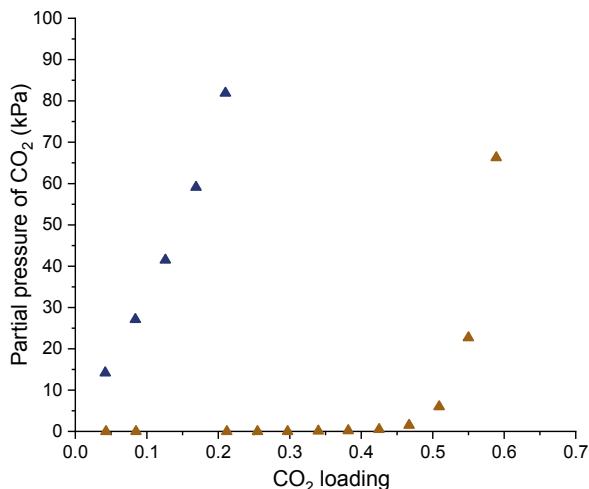


Figure 2.5. The solubility of CO₂ in MEA-NMP solutions at 40 (brown symbols) and 120 °C (blue symbols). The data were taken from Wanderley et al., (2020).

Several NASs and WLSs have been investigated recently, including ionic liquids (Kumar et al., 2014), aminosilicones (Perry et al., 2010), amines in organic solvents (Barzagli et al., 2014; Lail et al., 2014; Mobley et al., 2017), and amino acids in organic solvents (Firaha and Kirchner, 2016), among others. The literature focuses on experimental studies for the determination of solubility of CO₂ (Svensson et al., 2014a; Wanderley et al., 2020, 2019), absorption kinetics (Karlsson and Svensson, 2017; Wanderley et al., 2019), continuous experiments (Barzagli et al., 2014), heat of absorption measurements (Svensson et al., 2014c; Zheng et al., 2012), and speciation studies using NMR, of various single or blended amines in combination with various organic solvents (Barzagli et al., 2014, 2012). Non-rigorous modelling of NASs has been performed using various models: Kent-Eisenberg (Pakzad et al., 2018; Zheng et al., 2013), Deshmukh-Mather (Pakzad et al., 2018), and Jou-Mather (Li et al., 2014), among others. While non-rigorous models are empirical and, in some cases, may model the system accurately, the calculations are specific to each case and must be repeated for a particular amine in each new solvent. On the other hand, a rigorous model for an amine in a solvent, provides the possibility to transfer some of the thermodynamic parameters to model the same amine in another solvent. Therefore, rigorous models are desirable when modelling an amine in several solvents to accelerate research in this relatively new field. Rigorous modelling is hence identified as a knowledge gap in the field of NASs. The work presented in this thesis concentrates on the case of AMP in NMP, however, the methodology can be applied to other NAS systems, as will be seen in Chapter 4.

2.2 Phase-change systems

When precipitation or liquid-liquid splitting is involved in an aqueous system, the heat of regeneration can be expressed as in Equation (2.7).

$$\Delta H_{reg} = \Delta H_{rxn} + \Delta H_{vap} + \Delta H_{sens} + \Delta H_{phase} \quad (2.7)$$

The heat of phase change, ΔH_{phase} , must be compensated for in the regeneration column, and the entire plant must be designed to handle the phase change. In liquid-liquid splitting this could mean being able to handle higher viscosity, while for solid-liquid splitting, it could additionally mean being able to handle precipitation in the cooler parts of the plant. A criticalities study for the identification of unit operations prone to unwanted precipitation has been performed for the $\text{CO}_2\text{-NH}_3\text{-H}_2\text{O}$ system (Sutter et al., 2015). Similar analyses would be necessary for all precipitating systems. Nonetheless, pilot plant studies have shown that it is possible to work with precipitating systems (Aronu et al., 2018; Qader et al., 2017). Caution during intermittent operation and operation with concentrated solutions has been recommended in one of the pilot studies (Qader et al., 2017).

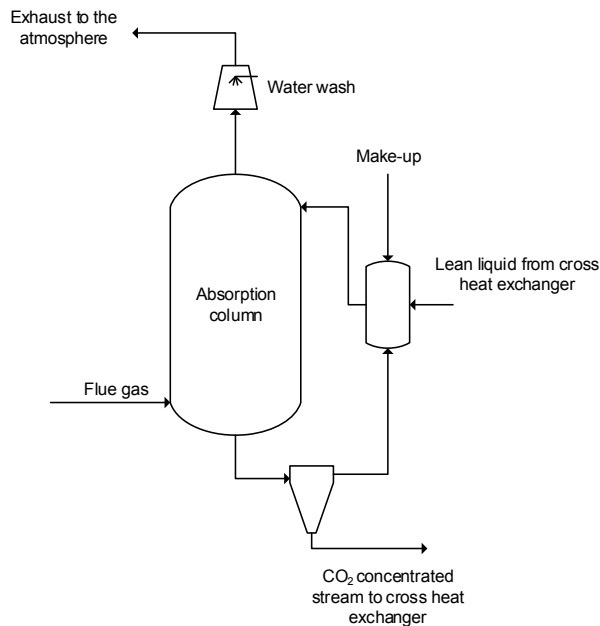


Figure 2.6. Process flow diagram for a precipitating CCS system.

As discussed above, and shown in Figure 2.6, only the fraction with high CO_2 loading would be separated and regenerated in phase-change systems, while the rest of the stream could be recycled without heating in the regeneration column.

This means that less water (or solvent) in the regeneration column needs to be vaporized and a smaller amount of solution needs to be heated to the regeneration temperature. Therefore, both the sensible heat and heat of vaporization are lowered at the expense of an additional heat of phase change. The sensible and vaporization heat can be partly lost in the stripper overhead, while the higher heat of reaction results in a higher CO₂ pressure in the stripper. Such thermal compression reduces the downstream cost of mechanically compressing the CO₂ (Lin and Rochelle, 2016). Similarly, phase change enthalpy also results in higher CO₂ pressure in the stripper and can be good for the energy performance of the stripper.

Improved absorption rate and increased loading capacity are other advantages that have been discussed with respect to precipitating systems (Ma, 2014). However, the opposite has also been observed, where precipitation has led to a decrease in the absorption efficiency (CO₂ absorbed per CO₂ flow in a continuous absorption column) (Barzagli et al., 2012). These contrasting results could be due to differences in the properties and size of the crystals formed. It has been argued that if the particle size is smaller than the width of the gas-liquid boundary layer, this could affect the absorption rate positively or negatively depending on the properties of the particles, while particles larger than the gas-liquid boundary layer would not influence the absorption rate (Ma, 2014; Zarzycki and Chacuk, 1993). Additionally, an increase in viscosity has been seen in precipitating systems due to dissolving salt, which also has a negative effect on the mass transfer in the system (Mullin, 2001).

The improvements obtained by operating with liquid-liquid splitting have already been demonstrated (Budzianowski, 2017a, 2017b), and were discussed in Section 1.1. A precipitating system based on aqueous K₂CO₃ has been demonstrated in pilot plant studies (Qader et al., 2017). Precipitating system such as 4M aqueous solution of potassium taurate has been rigorously modelled, and it has been observed that separating 20% of the solution and recycling before regeneration reduces the regeneration heat duty from 3310 to 2450 kJ/kg CO₂ separated. The same simulation showed that the 30wt% MEA solution has a reboiler duty of 3660 kJ/kg CO₂ separated, which is in the range of 3000 to 3900 kJ/kg CO₂ separated as discussed above in this chapter. However, amino-acid-based systems are not simply precipitating systems. They are also “pH swing” systems, i.e., part of the benefit is derived from the change in the pH of the system, and only part of the benefit is the result of precipitation (Sanchez-Fernandez et al., 2014).

Several studies on precipitating systems for CO₂ capture can be found in the literature, including studies to determine the solubility of CO₂ in precipitating systems (Ma'mun, 2014; Svensson et al., 2014a), detailed modelling and process simulations of precipitating systems (Sutter et al., 2015), studies in lab-scale continuous setups (Barzagli et al., 2012), and pilot plant tests (Aronu et al., 2018; Qader et al., 2017). Properties related to crystallization kinetics such as the

metastable zone width (Aronu and Ma, 2017; Majchrowicz et al., 2009), and kinetic parameters (Sutter et al., 2014; Wu et al., 2017a) have been determined for various precipitating systems. However, the crystallization kinetic theories applied have been developed for liquid-solid systems, not gas-liquid-solid systems.

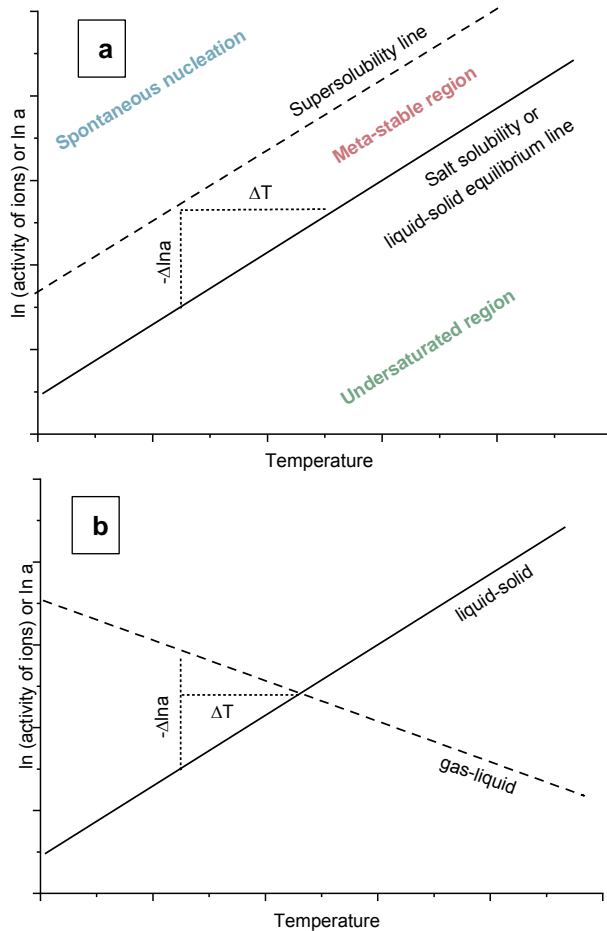


Figure 2.7. Representation of the relation between the meta-stable zone width in terms of the logarithm of activity and temperature for: a) simple liquid-solid systems and b) an example of a simplified gas-liquid-solid system.

Figure 2.7a shows a representation of the traditional system to which the existing precipitation kinetic theories are applied. The chemistry in this case consists of a single salt dissolution reaction as shown in Reaction {10} and the saturation activity of the ions is related to temperature as shown in the Figure 2.7a. That is, the meta-stable zone width (MSW) is a simple function of temperature. The systems that follow the behavior shown in Figure 2.7a are termed simple solid-liquid systems throughout this thesis.



In CCS applications, the chemistry involved is more complex. In the simple liquid-solid system, there are two phases and a single reaction. Unlike these systems, CCS applications (gas-liquid-solid system) might have three phases and at least two reactions. Figure 2.7b shows a simplified example of a gas-liquid-solid system, where the chemistry only involves two reactions: one gas-liquid reaction and one liquid-solid reaction. Figure 2.7b suggests that the MSW could be affected by the temperature and the activity of the ions when gas-liquid-solid chemistry is involved. If this is the case, traditional theories must be adapted to fit the changing chemistry that can lead to supersaturation resulting from more than one reaction. Gaseous CO₂ has been avoided in previous attempts to determine crystallization kinetics in CCS applications (Sutter et al., 2014; Wu et al., 2017b), probably due to the limitation of traditional crystallization kinetics theories. Nonetheless, it is yet to be shown theoretically that avoiding CO₂ release is sufficient in adapting traditional theories to crystallization in CCS applications. This is therefore identified as a knowledge gap in studies concerning precipitating systems. This thesis concentrates on the precipitation of carbamic acid amine salt in the AMP in NMP system. However, the methodology developed can be applied to any other multi-reaction-based precipitating system (even aqueous systems), as discussed in Chapter 5.

2.3 The system studied in this work: AMP-NMP

AMP is a sterically hindered primary amine, and NMP has been used as a physical sorbent for CO₂ (Yu Chih-Hung and Tan, Chung-Sung, 2012). The proposed reaction mechanism for this system is given by Reactions {7}, {9} (introduced above) and Reaction {11}. The CO₂ reacts with amine in the system to form zwitterion which is deprotonated by another amine molecule to form carbamate ion and protonated amine ion. When the ions reach sufficiently high concentration the carbamic acid amine salt, referred to in this thesis as the salt, precipitates in the form of white crystals.



From the reaction mechanism, it is clear that the maximum loading of AMP in the NMP system is only 0.5. This can be compared with the aqueous AMP and

aqueous MEA solutions, which have maximum loadings of 1 and 0.7, respectively (Sherman and Rochelle, 2017; Svensson et al., 2014a). The AMP-NMP system has been used as a model system to apply and test the methodologies developed in the present work since it is both an NAS and a precipitating system. Hence, methodologies developed for both can be tested using AMP-NMP.

3 Solubility Experiments

Most of the previous work on the AMP-NMP system has been performed within our research group. The physical solubility of CO₂ in NMP at 25 and 50 °C has been measured (Svensson et al., 2014a). The physical solubility of CO₂ in AMP-NMP solutions was determined using the N₂O analogy, and the viscosity of AMP-NMP solutions has been measured (Karlsson, 2018). The solubility of CO₂ in AMP-NMP solutions has been determined at 25, 40, 50 and 88 °C (Svensson et al., 2014a; Svensson and Karlsson, 2018). The heat of absorption for CO₂ in AMP-NMP mixtures has been obtained at 25 and 50 °C (Svensson et al., 2014c). To check the validity of the model developed to answer RQ1, it is important to measure the solubility of CO₂ in the solutions at a much wider range of temperatures. This will help in improving the quality of regression of parameters and when observing the behavior of the model with temperature. Therefore, solubility experiments were performed at various operating conditions, as described in this chapter.

The rate of absorption of CO₂ in the AMP-NMP system, measured using a wetted wall column, has previously been compared to that in aqueous MEA. The rate of absorption of CO₂ (for partial pressures up to 19 kPa) in 5m AMP in NMP and 1.5m AMP in NMP was found to be higher, than in 7m MEA in water and 1.5m MEA in water, respectively (Karlsson and Svensson, 2017). This is probably the result of the fact that the physical absorption of CO₂ in AMP-NMP is 4 times higher than that in MEA in water (Karlsson, 2018; Mota-Martinez et al., 2017). This higher absorption rate in AMP-NMP system compared to aqueous MEA is despite the higher viscosity of the former compared to the latter. Indeed, unloaded AMP-NMP system has 34% higher viscosity compared to the aqueous MEA at 40 °C (Karlsson, 2018). However, these experiments did not include precipitation, and the kinetic behavior could change with precipitation. Furthermore, if crystallization is to be included in the process design, knowledge is required on the crystallization kinetics and the saturation solubility of the salt in the solution as a function of temperature is needed to model the crystallization kinetics (see Chapter 5). The experiments carried out to determine the saturation solubility of the salt, to be used in obtaining the crystallization kinetics, are also described in this chapter.

3.1 Materials and Methods

3.1.1 Materials

The materials used in the experiments described in Section 3.1.2 were CO₂, AMP and NMP. For the experiments described in Section 3.1.3, AMP, NMP, CO₂, the carbamic acid amine salt of AMP, triethylene glycol dimethyl ether (TEGDME), hexane and silica were used. The solutions used in the experiments described in Section 3.1.2 were pure NMP (0AN), 15 wt% AMP in NMP (15AN) and 25 wt% AMP in NMP (25AN). The solubility of the salt was measured in 0AN, 15AN and 25AN (see Section 3.1.3). These salt solubility experiments were also performed in pure TEGDME (0AT), 2.5 wt% AMP in TEGDME (2.5AT) and 15 wt% AMP in TEGDME (15AT).

3.1.2 Solubility of CO₂ in AMP-NMP solutions

Experiments were performed to measure the solubility of CO₂ in the AMP-NMP solutions according to Reactions {7}, {9} and {11}. Two types of experiments were performed. The first type was performed to obtain the solubility of CO₂ in the AMP-NMP solutions (0AN, 15AN and 25AN) at different temperatures using an equilibrium time of 30 min (Paper I). Results from these experiments, together with results from previous experiments (Svensson et al., 2014a; Svensson and Karlsson, 2018), were used to regress the thermodynamic property parameters (Paper II). The experimental procedure followed to perform the experiments described in Paper I was the same as that described in the previous studies (Svensson et al., 2014a; Svensson and Karlsson, 2018).

These experiments were conducted at a constant temperature in a glass and stainless steel true heat reaction calorimeter (CPA201 Chemical Process Analyser, ChemiSens AB), with a volume of 250 cm³ (see Figure 3.1). Approximately 100 g of solution was added to the calorimeter at the beginning of the experiment. The system was evacuated for 10-12 s at 25 °C prior to each experimental run. CO₂ was added in batches of injections using a Bronkhorst Hi-Tec mass flow controller (MFC). The system was then allowed to reach equilibrium before CO₂ was again introduced into the reactor. An automation script was used to control the experiments and ensure equilibrium. This seeks stability in pressure (within ±0.005 bar) and true heat flow (within ±0.02 W) for 30 min, which is the definition of equilibrium in the type of experiments described in Paper I. In addition to pressure and true heat flow, the temperature and mass flow signals were also logged continuously throughout the experiment, in a computer. Two to four experiments were performed to check repeatability.

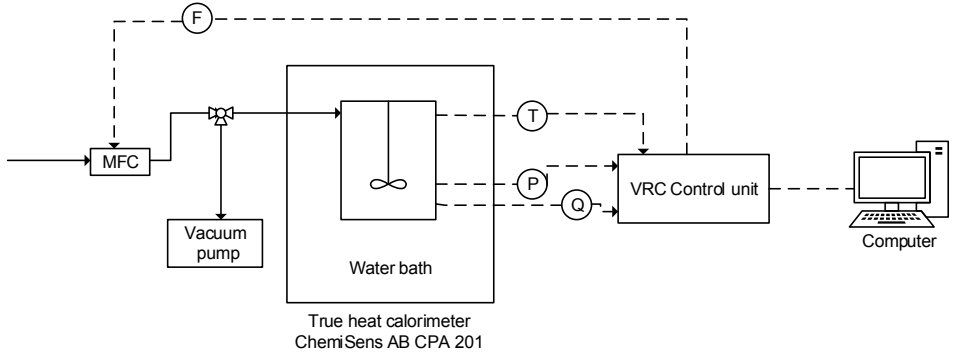


Figure 3.1. A schematic of the calorimeter used for the experiments presented in Papers I, III and IV.

The second type of experiments, described in Paper IV, was used to update the thermodynamic model developed in Paper II, the results of which are also presented in Paper IV. They were performed to obtain the solubility of CO₂ in 15AN and 25AN solutions at different temperatures (25, 40 and 60 °C). In this second type of experiments, 10 to 25 mg silica was added to the solution to act as crystallization seeds, and the definition of equilibrium was changed to stability in pressure (within ±0.005 bar) for at least 330 min. The purpose of these experiments was to investigate the effect of equilibrium time on the solubility, in order to shed light on whether equilibrium was truly achieved in the experiments described in Paper I. The seeds were added to provide an initial surface area for crystallization and to accelerate the process of achieving equilibrium.

From the data obtained, the amount of CO₂ absorbed in the solvent, $(CO_2)_{abs}$, was calculated from Equation (3.1):

$$(CO_2)_{abs} = (CO_2)_{in} - \frac{P_{CO_2}V}{RT} \quad (3.1)$$

where $(CO_2)_{in}$ is the total amount of CO₂ added to the reactor, and was calculated from the MFC signal. P_{CO_2} is the partial pressure of CO₂ above the solution, measured using the pressure transducer as the difference in the pressure at equilibrium and the initial pressure. The vapor pressure of amine and solvent in the gas phase of the reactor was assumed to be constant and equal to the total equilibrium pressure before the first addition of CO₂ to the reactor. V is the volume of the gas above the liquid in the reactor, R is the universal gas constant, and T is the temperature in K. The CO₂ loading, α , is defined as the number of moles of CO₂ absorbed per mole amine initially in the system, as in Equation (3.2):

$$\alpha = \frac{(CO_2)_{abs}}{n_{AMP,0}} \quad (3.2)$$

where $n_{AMP,0}$ is the amount of amine (AMP) present in the system at the start of the experiment.

3.1.3 Solubility of the salt in AMP-NMP solutions

The aim of these experiments was to measure the solubility of the salt in AMP-NMP solutions. The salt was produced by bubbling CO₂ in 20 wt% AMP in NMP solution until crystals appeared. The crystals were then washed with hexane and filtered under vacuum. The experiments performed to measure the solubility of the salt were repeated using a salt sample that was produced by bubbling CO₂ into 20 wt% AMP in NMP until crystals appeared, heating the solution with the crystals (in a closed reactor) until the crystals dissolved, and cooling the solution until the crystals reappeared. These reappeared crystals were then washed with hexane and filtered under vacuum as in the first case. Some experiments were also performed using TEGDME as the solvent in place of NMP.

The dissolution of the salt in the solution is a result of Reactions {11}, {9}, and {7} shifting to the left. That is, the salt dissolves in the solution to form carbamate and protonated amine ions, which in turn release amine and CO₂ into the solution. The salt dissolution can eventually lead to release of gaseous CO₂. The solubility of crystals in solution can be measured either by using the polythermal method or the isothermal method. In the polythermal method, the solubility of the salt is determined by adding a known amount of crystals to a solution and heating at different heating rates until the crystals dissolve. The saturation temperature is then obtained by extrapolating the dissolution temperature to zero heating rate (Barrett and Glennon, 2002; Sutter et al., 2014).

In the present case, an isothermal process was used, where the solubility was measured in the setup shown in Figure 3.2. The salt was weighed and added to a test tube, 380 cm³ in volume, which was then closed using a lid solely by friction (i.e., external means were not used to hold the lid in place). The pressure in the test tube would increase if CO₂ was released from the salt. Closing the test tube solely by friction ensured that the lid opened due to pressure build-up when pressure inside the test tube deviated from atmospheric pressure. Therefore, the experiments where the lid did not open can be said to be performed close to atmospheric pressure. This is important since the pressure in the test tube was not measured. The experiments where the lid opened due to pressure build-up were disregarded and repeated with lower amount of salt in the test tube. After closing the test tube, a solution was added to the test tube (intermittently) using a syringe pump. A magnetic stirrer ensured mixing of the salt and the solution. The desired temperature was maintained in the test tube by circulating hot water from a reservoir. A thermocouple was used to measure the temperature of the water in the reservoir, and a feedback signal was sent to the heater to maintain it at the

required level. The temperature of the water bath was varied between 25 and 88 °C in all the experiments, and the amount of solution needed to dissolve a known amount of salt was noted at a given temperature. This procedure was repeated for various temperatures and for various solutions (0AN, 15AN, 25AN, 0AT, 2.5AT and 15AT).

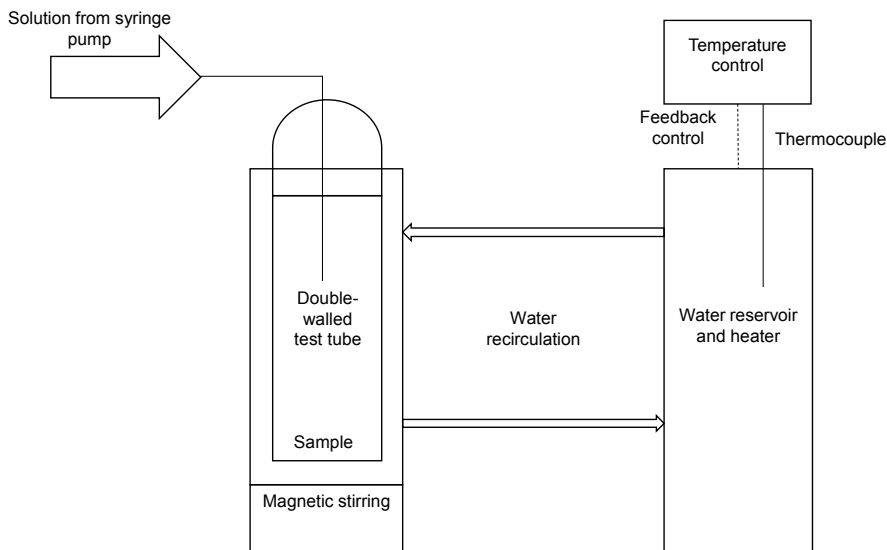


Figure 3.2. A schematic of the setup used to measure the solubility of the salt. Re-printed from Paper III, which is licensed under Creative Commons license.

The solubility of the salt measured in the test tube was expressed as moles of crystals dissolved per kg of solvent (NMP or TEGDME) according to Equation (3.3):

$$\ln c^s = A_S + B_S T \quad (3.3)$$

where c^s is obtained by dividing the number of moles of crystals in the test tube by the amount of solvent (in kg) needed to dissolve the crystals at temperature T . A_S and B_S are the parameters used to fit the solubility to the temperature.

The experiments described in Papers III and IV, to determine the crystallization kinetics, were performed in the calorimeter. In these experiments, 100 g of solution was added to the reactor of the calorimeter (Figure 3.1), and CO_2 was injected into the solution until precipitation was observed. The solution was heated until the crystals dissolved. The solubility of the salt at the dissolution point is referred to as the saturation solubility of the salt. The solution is then cooled (at different rates) until crystals formed once again. The solubility of the salt determined in the test tube, expressed according to Equation (3.3), can be

correlated to the saturation solubility of the salt in the calorimeter, which can be calculated according to Equation (3.4):

$$c^s = \frac{(CO_2)_{abs}}{w_{NMP}} \quad (3.4)$$

where $(CO_2)_{abs}$ is obtained from Equation (3.1) and w_{NMP} is the mass (in kg) of NMP in the solution used. In Equation (3.4) the upper limit of the solubility of the salt in the calorimeter is obtained because it is assumed that all the absorbed CO_2 is in the form of crystals. However, if the physically dissolved CO_2 , zwitterion and carbamate ion concentrations are negligible at dissolution (see the reaction mechanism in Section 2.3), it can be assumed to be the solubility of the salt.

The above described method for obtaining saturation solubility of the salt was used in Paper III, when calculating the crystallization kinetics. In paper IV, the saturation solubility of the salt was obtained from the thermodynamic model developed using the solubility experiments described in Section 3.1.1, with an equilibrium time of 330 min or longer. The thermodynamic model is discussed in Chapter 4.

3.2 Results and Discussion

3.2.1 Solubility of CO_2 in AMP-NMP solutions

The results from the first type of experiments (Paper I), with an equilibrium time of 30 min, described in Section 3.1.2, are shown in Figure 3.3. In 15AN (Figure 3.3b), precipitation occurred at 25 and 40 °C for loadings of 0.35 and 0.5 mol CO_2 /initial mol AMP, and the corresponding partial pressures of CO_2 were 10 kPa and 100 kPa, respectively. The solubility was higher in 25AN (Figure 3.3a) than in 15AN, at temperatures of 25-50 °C. This was largely the result of precipitation, which occurred at loadings of 0.2-0.3 mol CO_2 /initial mol AMP at relatively low partial pressures of up to 20 kPa.

It was pointed out in Section 2.1 that the means of stripping must be considered when replacing all the water with a high-boiling non-aqueous solvent. If the regeneration column is operated at atmospheric pressure, a lean loading of 0.05 can be achieved at 88 °C for both amine concentrations (see Figure 3.3) (Svensson and Karlsson, 2018). This means reasonably lean loadings can be achieved with AMP-NMP system even without a stripping agent.

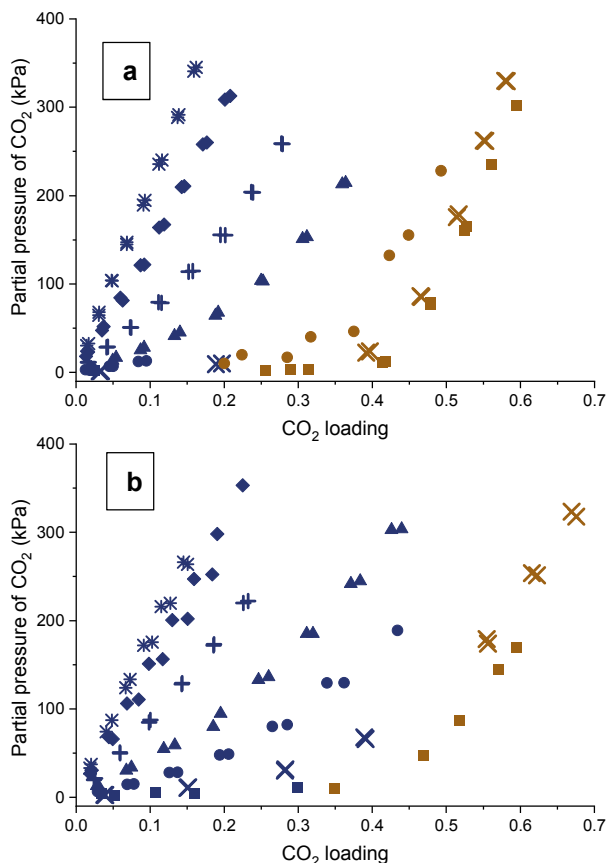


Figure 3.3. Solubility of CO₂ in AMP-NMP solutions: a) 25AN and b) 15AN, with an equilibrium time of 30 min. The explanation for the symbols is as follows: blue symbols = precipitation did not occur, brown symbols = precipitation occurred, ■ = 25 °C, X = 40 °C, ● = 50 °C, ▲ = 60 °C, + = 70 °C, ◆ = 80 °C, and ✕ = 88 °C. The sources for the data are as follows: 25, 50 °C = Svensson et al., (2014a), 40, 88 °C = Svensson and Karlsson, (2018), 60, 70, 80 °C = Paper I.

If a temperature of 40 °C and a CO₂ partial pressure of 20 kPa are used in the absorption column and a temperature of 88 °C and atmospheric pressure are used in the regeneration column with a 25AN solution, a cyclic capacity of about 0.3 mol CO₂/mol initial amine is possible. This is comparable to the cyclic capacity of the aqueous MEA solution (see Figure 2.4), where the rich loading is 0.5 and the lean loading is 0.2. However, using 25AN shifts the loadings to lower values compared to aqueous MEA, without compromising cyclic capacity. This could be much better in terms of corrosion, which usually increases with CO₂ loading (Blomen et al., 2009; Pearson and Cousins, 2016).

If the 25AN solution is to be used industrially, with a cyclic capacity comparable to that of aqueous MEA, it is likely to be a precipitating system. To use it as a non-precipitating system, concentrations of AMP as low as 15 wt% must be used.

This means that the total amount of CO₂ captured per kg of solution would be lower than in 25AN solutions, requiring higher circulation rates in the plant. A chiller (not shown in Figure 2.1) would probably be necessary to cool the inlet stream to the absorption column down to 25 °C, with a likely trade-off between absorption kinetics and cyclic capacity. The rich loading could then be as high as 0.35 and the lean loading as low as 0.05, making the cyclic capacity comparable to that using aqueous MEA but, at an additional cost due to higher circulation rates and the need for a chiller.

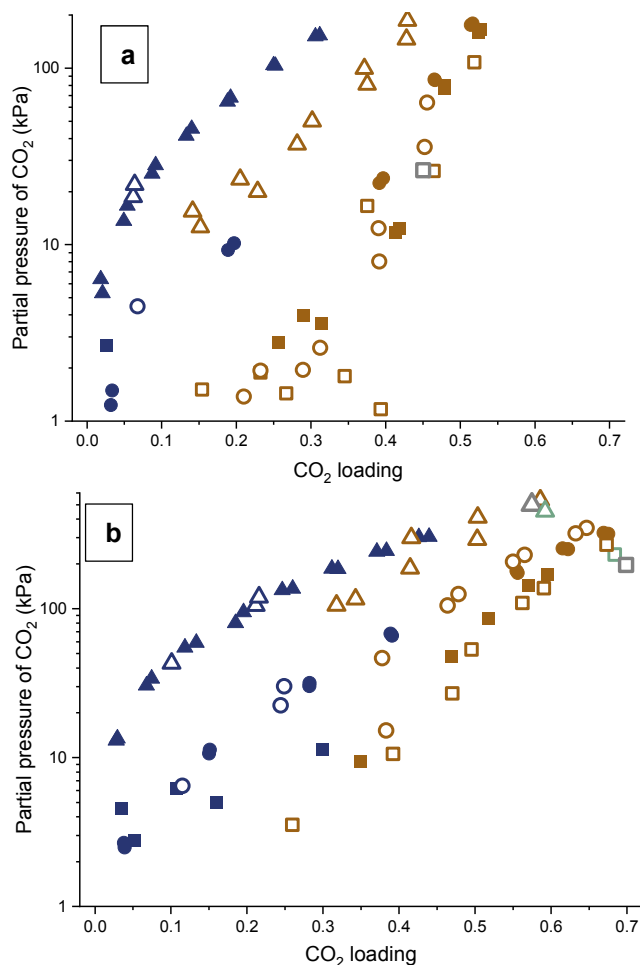


Figure 3.4. Comparison of the solubility of CO₂ in AMP-NMP solutions for equilibrium times of 30 min and 330 min for solutions of a) 25AN and b) 15AN. The explanation for the symbols is as follows: blue symbols = precipitation did not occur, brown symbols = precipitation occurred, gray symbols = equilibrium not reached, green symbols = equilibrium after precipitation that corresponds to the gray symbols at the same temperature, ■ = 25 °C, 30 min, ● = 40 °C, 30 min, ▲ = 60 °C, 30 min, □ = 25 °C, 330 min, ○ = 40 °C, 330 min, and △ = 60 °C, 330 min. The sources of the data are as follows: 25 °C, 30 min = Svensson et al., (2014a), 40 °C, 30 min = Svensson and Karlsson, (2018), 60 °C, 30 min = Paper I, 25, 40, 60 °C, 330 min = Paper IV.

Figure 3.4 compares the results of the experiments with equilibrium times of 30 min and at least 330 min. As seen in the figure, the state achieved with the former experiments was not true equilibrium. If it were true equilibrium, there would not have been any change in loading with additional time. The experiments with at least 330 min of equilibrium times are likely closer to true equilibrium. In Figure 3.4a, it can be seen that at 25 °C, the partial pressure of CO₂ is close to zero for CO₂ loadings as high as 0.4, when allowed to equilibrate for at least 330 min. On the other hand, with an equilibrium time of 30 min, the partial pressure of CO₂ deviates from zero significantly already at a CO₂ loading of 0.25. That is, the solution should be saturated with CO₂ when the loading is at least as high as 0.4, if the system has been given enough time to equilibrate. At 40 and 60 °C, precipitation took place at much lower loadings with equilibrium times of > 330 min compared to that of 30 min. This suggests that the solutions were supersaturated in the experiments with an equilibrium time of 30 min and needed much higher equilibrium time to precipitate.

Similar behavior is observed with 15AN solution (Figure 3.4b). At 25 °C, the 15AN solution is saturated with CO₂ at much higher loadings with an equilibrium time of 330 min as compared to the experiments with an equilibrium time of 30 min. Again, precipitation occurred at much lower CO₂ loadings when equilibration was allowed for > 330 min as compared to that of 30 min, suggesting supersaturated solutions in the latter experiments. The residence time in commercial plant operation is more likely to be closer to 30 min. However, this may increase considerably, for example, during unexpected shutdown. It can be seen from Figure 3.4 that such an increase in the residence time would lead to higher loading, and also to precipitation at much lower loadings than under normal operating conditions. This suggests that if a CCS plant were to be designed using 15AN solution as a non-precipitating solution, as described above, precipitation can be expected during intermittent operation.

The driving force for CO₂ absorption will depend on the concentration at true equilibrium, and not the value obtained from the experiments with 30 min equilibrium time, making it important to determine the true equilibrium from a design point of view. The error in the driving force would be lower when using the results from experiments performed with an equilibrium time of 330 min, instead of 30 min.

The difference between the partial pressures obtained in the original and the duplicate experiments with at least 330 min equilibrium time are very high in some cases (maximum deviations of 20 kPa and 60 kPa were observed for 25AN and 15AN, respectively). This was especially observed at 60 °C and higher loadings, and could be the result of insufficient time to reach equilibrium in one of the two cases. For 15AN at 60 °C (Figure 3.4b), precipitation took place a second time after apparent equilibrium had been reached (the data point in gray is before secondary precipitation and the point in green is after). This secondary

precipitation led to a decrease in the partial pressure of CO₂. Another interesting point was observed in Figure 3.4b, for 15AN at 25 °C, where precipitation resulted in an increase in the partial pressure of CO₂, in contrast to all the other data points (in gray is the data point before precipitation and the point in green is after). At 40 °C in 15AN, the experiments with an equilibrium time of > 330 min and higher loadings showed higher partial pressures of CO₂ as compared to that of 30 min. This also differs from the other experimental data points. The reason for these inconsistencies is unknown. Because both an increase or a decrease in pressure are observed with increased time, it is not possible to determine which of the two experimental points obtained with equilibrium times of 330 min (at a given temperature with a given solution) is closer to true equilibrium. Longer equilibrium times may provide the answer to this. For example, with 15AN, precipitation took place after 420 min in one instance. The green point in Figure 3.4b discussed above depicts equilibrium after 660 min. Since it is impossible to know how long the equilibrium time should be to achieve true equilibrium, equilibrating for longer times is an impractical approach. Another way of determining the true equilibrium is therefore preferable (suggested in Chapter 4). There is also a gray point in Figure 3.4a, where the equilibrium conditions set in Section 3.1.2 were not reached and this point is excluded from further consideration.

3.2.2 Solubility of the salt in AMP-NMP solutions

The purpose of measuring the salt solubility in the test tube was to be able to correlate it with the salt solubility under the dissolution conditions used in the calorimeter (see Chapter 5). The solubility of the salt in NMP solutions obtained in the test tube is shown together with the solubility of CO₂ obtained in the calorimeter at the dissolution temperature in Figure 3.5. The solubility of the salt was obtained as described in Section 3.1.3, and the data points were fitted to Equation (3.3) using data from both salt samples described in Section 3.1.3. The parameters of the fitted curves shown in Figure 3.5 are given in Table 3.1. The solubility of CO₂ in the NMP solutions obtained from the calorimeter according to Equation (3.4) are shown as data points. Points in the same color represent data from the same experimental series obtained at different cooling rates (see Chapter 5 for more details). Two interesting features can be observed in Figure 3.5. The first is that the solubility of CO₂ measured in the calorimeter, which would be an upper limit of the solubility of the salt observed in the calorimeter (Section 3.1.3), is much lower than that measured in the test tube. The second is that there is a change in the dissolution temperature of the salt formed in the calorimeter (brown points). After the shift in dissolution temperature was observed, the solution was cooled until crystallization and heated again to dissolve the crystals formed. However, the crystals did not dissolve even after heating to 88 °C in the same

series of experiments. These observations must be addressed to avoid unacceptably large errors in the solubility of the salt.

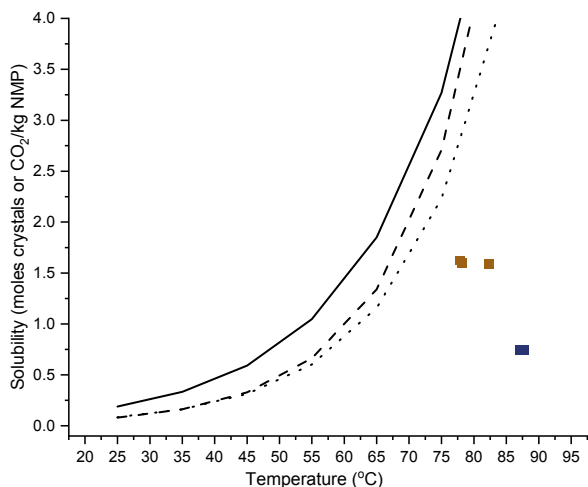


Figure 3.5. Comparison of the solubility of the salt in AMP-NMP solutions obtained in the test tube (lines) with the solubility of CO₂ obtained in the calorimeter (points). The explanation for the symbols is as follows: ■ = CO₂ loading of 0.62, ■ = CO₂ loading of 0.34, (—) = solubility of the salt in 0AN, (— —) = solubility of the salt in 25AN, and (···) = solubility of the salt in 15AN. The data points were obtained with 25AN.

Table 3.1. Values of the parameters describing the solubility of the salt in different solutions of AMP-NMP, measured in the test tube and fitted to Equation (3.3).

Solution	A	B	R ²
0AN	-3.09	0.057	0.9383
15AN	-4.11	0.066	0.9536
25AN	-4.28	0.070	0.8942

The shift in the dissolution temperature is examined further in Chapter 5. The lower solubility measured using the calorimeter could be due to three reasons. The first is the difference in pressure between the experiments performed in the test tube and in the calorimeter. The pressure in the calorimeter increased to 600 kPa in one series of experiments and 1000 kPa in the other, while in the test tube it remained close to 100 kPa. The second is the CO₂ released (but unaccounted for) in the test tube during the salt solubility measurements. In the experiments performed in the test tube, the amount of salt dissolved is considered. When dissolved, the salt gives rise to carbamate (=protonated amine) ions, zwitterions, dissolved CO₂, and released CO₂. In the experiments performed in the calorimeter, the absorbed CO₂ is measured, which is equal to the carbamate ions, zwitterions and dissolved CO₂ at the dissolution temperature. Not accounting for the released CO₂ in the test tube can thus lead to errors. As mentioned in Section 3.1.3, the experiments in the test tube, where the pressure could have been significantly higher than atmospheric were disregarded and the experiment was

repeated with lower amounts of salt. The reason for this was to minimize the error due to the unaccounted CO₂ release. However, the amount of salt that allowed for acceptable operation in the test tube was so small (0.05 to 0.38 g) that the percentage of CO₂ released per amount of salt could still be substantial without increasing the pressure in the test tube significantly. In the calorimeter, the CO₂ released in the gas phase through dissolution was quantified and found to be 30% of the CO₂ loading for 25AN.

The third reason maybe the formation of free amine during dissolution of the salt in the test tube. As seen from the solubility curves in Figure 3.5, the presence of amine in the solution affects the solubility of the salt. However, the salt used in the test tube contained only 1-2% amine compared to the amount of amine in 25AN solution. On the other hand, in the calorimeter, the change in free amine concentration is much higher upon crystal dissolution, since 25AN solution was used in these experiments and a large amount of crystals was formed.

If lower amounts of amine (as low as 5 wt%) could be used in the calorimeter, the pressure difference between the two setups, the CO₂ released as gas in the calorimeter, and the change in the free amine concentration, can all be minimized. However, using such low amounts of amine in NMP does not lead to crystallization (on cooling) within the temperature range of the calorimeter, making it difficult to estimate the crystallization kinetics. The method was therefore tested with another solution, namely AMP in TEGDME. In contrast to AMP-NMP system, in AMP-TEGDME solution salt precipitates for amine concentrations as low as 2.5 wt%. Reducing the amount of amine used in the calorimeter will cause less salt to precipitate. This means that on dissolving the salt, a higher percentage of the precipitated salt will be physically absorbed in the TEGDME solvent, and less CO₂ will be released into the gas phase. It also means that the CO₂ pressure in the calorimeter will be closer to that in the test tube, and less amine will thus influence the solubility curve.

Figure 3.6 compares the solubility of the salt measured in the test tube with the solubility of CO₂ measured in the calorimeter for AMP in TEGDME solutions. The values of the fitted parameters are given in Table 3.2. As can be seen from the figure, the results obtained using the test tube are in much better agreement with the results in the calorimeter for the 2.5AT solution. The pressure generated in these experiments performed in the calorimeter was 130 kPa to 200 kPa during dissolution, while the pressure in the test tube was ~100 kPa. However, the values obtained using the calorimeter still do not agree with the results obtained using the test tube in all the experiments. The first dissolution point was always 4 to 10 °C lower compared to all the other dissolution points in every experiment series performed with this solution in the calorimeter. Therefore, a shift in the dissolution temperature was observed with both systems but, the behavior in 2.5AT was consistent unlike that in 25AN. Moreover, the CO₂ released during

dissolution is up to 33% in the calorimeter for 2.5AT solutions. This source of error could not be eliminated in either solvents.

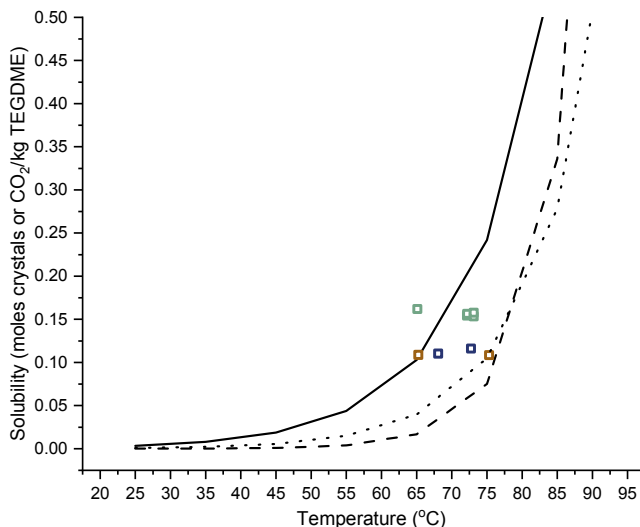


Figure 3.6. Comparison of the solubility of the salt in AMP-TEGDME solutions obtained in the test tube (lines) with the solubility of CO₂ obtained in the calorimeter (points). The explanation for the symbols is as follows: \square = CO₂ loading of 0.54, \diamond = CO₂ loading of 0.56, \triangle = CO₂ loading of 0.77, (—) = solubility of the salt in 0AT, (---) = solubility of the salt in 2.5AT, and (···) = solubility of the salt in 15AT. The data points were obtained with 2.5AT.

Table 3.2. Values of the parameters describing the solubility of the salt in different solutions of AMP-TEGDME, measured in the test tube and fitted to Equation (3.3).

Solution	A	B	R ²
0AT	-7.82	0.085	0.9676
2.5AT*	-13.82	0.150	0.9418
15AT*	-9.57	0.098	0.9676

*The parameters were obtained from data between 55 and 90 °C only.

It is now understood why the method used to estimate solubility in the test tube could not be used to determine the crystallization kinetics for the 25AN solution. Although two of the three sources of error could be eliminated reasonably in case of 2.5AT solution, 2.5 wt% amine is not likely to be an industrially viable solution, and the crystallization kinetics in a 2.5 wt% solution might not be the same as in solutions with higher concentrations of amine. Furthermore, a method is still required to estimate the solubility of the salt, in order to determine the crystallization kinetics for solutions in NMP. This is discussed in Chapter 4, where the experimental results from measurements of the solubility of CO₂ in AMP-NMP solutions are used to obtain a thermodynamic model that has value in itself, but can also be used to estimate the saturation solubility at the dissolution temperature in order to determine the crystallization kinetics. Also, since the release of CO₂ could not be avoided in the solutions used, it must be accounted for. The shift in dissolution temperature discussed above in this chapter must also

be considered. Both these aspects are addressed in Chapter 5, where the methodology used to determine the crystallization kinetics is described.

4 Modelling Non-aqueous Systems

A robust model of the AMP-NMP system should be able to predict the thermodynamic properties, transport properties, and reaction kinetics within reasonable error. In this chapter, a method of modelling the thermodynamic properties of the system, which is an NAS, was developed in an attempt to answer RQ1. RQ1 is further divided into two parts:

RQ1.1. Can an established thermodynamic property method be used to model NASs?

RQ1.2. Can the parameters developed for an amine in a solvent be adapted to model the same amine in other solvents?

4.1 Theory

For the accurate prediction of phase equilibrium in the system, a thermodynamic property model must predict the compositions of the vapor, liquid and solid phases. The changes taking place in these phases are illustrated in Figure 4.1. Chemical reactions influence the composition of the liquid, and hence the behavior of the phase. The reaction mechanism proposed in Section 2.3 has been simplified to that given by Reactions {12}, {13}, and {11}.



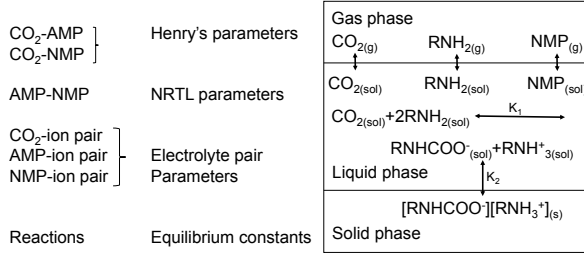


Figure 4.1. Physical and chemical interactions in the system and the corresponding parameters used.

The Gibbs energy for component i in an ideal mixture is given by Equation (4.1):

$$G_i^{id} = G_i^0 + RT \ln x_i \quad (4.1)$$

where G_i^{id} is the Gibbs energy of i in ideal solution, G_i^0 is the standard state Gibbs energy of pure component i , R is the universal gas constant, T is the temperature and x_i is the mole fraction of component i in the solution.

The Gibbs energy for component i in a non-ideal mixture is given by Equation (4.2):

$$G_i = G_i^0 + RT \ln \gamma_i x_i \quad (4.2)$$

where G_i is the Gibbs energy of i in a non-ideal solution and γ_i is the activity coefficient of the component. That is, the non-ideality is addressed by the activity coefficients.

In this work (see Papers II and IV), the thermodynamic model was developed using the property method ENRTL-RK in the commercially available software ASPEN Plus®. According to ENRTL-RK, the activity coefficient for an ion, i , is given by Equation (4.3) (Chen et al., 1982):

$$\ln \gamma_i^* = \ln \gamma_i^{*,local} + \ln \gamma_i^{*,PDH} + \ln \gamma_i^{*,Born} \quad (4.3)$$

where superscript, $*$, is used to denote unsymmetric reference state discussed in Section 4.1.1.1. $\gamma_i^{*,local}$ is the contribution to the activity coefficient from local interactions between the components. It is based on two assumptions: 1) like-ions repel each other, i.e., a cation (or anion) is never found in the immediate vicinity of another cation (or anion), and 2) local electroneutrality, as observed, for example, in a crystal lattice (Chen et al., 1982). $\gamma_i^{*,PDH}$ denotes the long-range interactions, i.e., coulombic forces. The term $\gamma_i^{*,Born}$ is a correction resulting from the different reference states used for $\gamma_i^{*,local}$ (infinite dilution in water) and

$\gamma_i^{*,PDH}$ (mixed solvent), known as the Born correction (Song and Chen, 2009) (Further details on the reference states are given in Section 4.1.1.2.).

4.1.1 Chemical reaction thermodynamics

This section gives a brief review of the relations between equilibrium constants, the activities of various components in the reaction, the concentrations in different units, and the activity coefficients in different reference states and concentration units. Reaction {11} is used as an example below, where + denotes the protonated amine and – denotes the carbamate ion.

4.1.1.1 Reference state

The equilibrium constant for the precipitation reaction in Reaction {11} is given by Equation (4.4) in pure component reference states for all components. The reference state for the precipitate is the pure solid state. The activities are then given by Equation (4.5) for the protonated amine, and similar equations can be written for the carbamate ion.

$$\ln K_2 = - \left(\frac{\Delta G_{[RNH_3^+][RNHCOO^-]}^{0,s} - \Delta G_+^0 - \Delta G_-^0}{RT} \right) = \ln \frac{1}{a_+ a_-} \quad (4.4)$$

$$a_+ = x_+ \gamma_+ \quad (4.5)$$

Here, K_2 is the equilibrium constant for Reaction {11}, $\Delta G_+^0, \Delta G_-^0$ and $\Delta G_{[RNH_3^+][RNHCOO^-]}^{0,s}$ are the Gibbs energies of the protonated amine ion, the carbamate ion and the precipitate in the pure component reference state, R is the universal gas constant, T is the temperature, a_+ and a_- are the activities of the protonated amine and carbamate ions, respectively, x_+ is the mole fraction of the protonated ion, and γ_+ is the activity coefficient of the protonated ion in the pure component reference state, the definition of which is given in Equation (4.6).

$$x_+ \rightarrow 1 \Rightarrow \gamma_+ \rightarrow 1 \quad (4.6)$$

However, it is impossible to achieve the state of a pure ion due to the electroneutrality constraint. In the case of dissolved salts, the state of pure fused salt is commonly used as the reference state. This is the symmetric reference state for ions, where the mean mole fraction and mean activity coefficient of the protonated ion and carbamate ion defined by Equation (4.7) are used as shown in Equation (4.8), which reduces Equation (4.4) to Equation (4.9).

$$x_{\pm} \rightarrow 1 \Rightarrow \gamma_{\pm} \rightarrow 1 \quad (4.7)$$

$$x_{\pm} = (x_+^{v_+} x_-^{v_-})^{\frac{1}{v}}, \gamma_{\pm} = (\gamma_+^{v_+} \gamma_-^{v_-})^{\frac{1}{v}}, a_{\pm} = (a_+^{v_+} a_-^{v_-})^{\frac{1}{v}} \quad (4.8)$$

$$\ln K_2 = - \left(\frac{\Delta G_{[RNH_3^+][RNHCOO^-]}^{0,S} - \Delta G_+^0 - \Delta G_-^0}{RT} \right) = \ln \frac{1}{a_{\pm}^{\frac{1}{2}}} \quad (4.9)$$

Here, $v = v_+ + v_-$, where v_+ and v_- are the stoichiometric coefficients for the cation and anion, respectively.

Another approach commonly used is the infinite dilution of the ions (also known as the unsymmetric reference state) defined by Equation (4.10). The equilibrium constant must then be consistently defined in the same reference state as in Equation (4.11), where the activity is as given in Equation (4.12). Finally, Equation (4.13) gives the relationship between the pure component reference state and the infinite dilution reference state.

$$x_+ \rightarrow 0 \Rightarrow \gamma_+^* \rightarrow 1 \quad (4.10)$$

$$\ln K_2^* = - \left(\frac{\Delta G_{[RNH_3^+][RNHCOO^-]}^{0,S} - \Delta G_+^* - \Delta G_-^*}{RT} \right) = \ln \frac{1}{a_+^* a_-^*} \quad (4.11)$$

$$a_+^* = x_+ \gamma_+^* \quad (4.12)$$

$$\gamma_+^* = \frac{\gamma_+}{\gamma_+^\infty}, \Delta G_+^* = \Delta G_+^0 + RT \ln \gamma_+^\infty \quad (4.13)$$

The superscript * denotes the reference state of infinite dilution, as defined by Equation (4.10), and γ_+^∞ is the infinite dilution activity coefficient of the cation in the symmetric reference state.

There are several different ways of defining infinite dilution. Equation (4.10) defines infinite dilution in a solution. The activity coefficient can also be normalized based on infinite dilution in a solvent, in the present case, NMP as in Equations (4.14) to (4.16):

$$x_{NMP} \rightarrow 1 \Rightarrow \gamma_{+(NMP)}^* \rightarrow 1 \quad (4.14)$$

$$\ln K_{2(NMP)}^* = - \left(\frac{\Delta G_{[RNH_3^+][RNHCOO^-]}^{0,S} - \Delta G_{+(NMP)}^* - \Delta G_{-(NMP)}^*}{RT} \right) = \ln \frac{1}{a_{+(NMP)}^* a_{-(NMP)}^*} \quad (4.15)$$

$$a_{+(NMP)}^* = x_+ \gamma_{+(NMP)}^* \quad (4.16)$$

where, $X_{(NMP)}^*$ is the property X with the reference state of infinite dilution in the solvent NMP.

The definition of infinite dilution in Equation (4.14) is more convenient compared to that in Equation (4.11). This is because the former avoids a change in the standard Gibbs free energies with the composition of the solution while in the latter, the composition affects both the activity coefficient and the behavior of standard state Gibbs energy.

4.1.1.2 Concentration scale

In Equations (4.4) to (4.16) the mole fraction scale is used, which is the basis for ASPEN Plus. Experimental data are usually expressed in terms of molality. Therefore, conversion from one scale to another is needed. For example, Equations (4.14) to (4.16) have been converted to molality scale in Equations (4.17) to (4.19). The activity coefficient in the molality scale is set to one at a hypothetical molality, $c_0 = 1 \frac{\text{mol}}{\text{kg NMP}}$.

$$c_+ \rightarrow c_0 = 1 \frac{\text{mol}}{\text{kg NMP}} \Rightarrow \gamma_{+(NMP)}^m = 1 \quad (4.17)$$

$$\ln K_{2(NMP)}^m = - \left(\frac{\Delta G_{[RNH_3^+][RNHCOO^-]}^{0,S} - \Delta G_{+(NMP)}^m - \Delta G_{-(NMP)}^m}{RT} \right) = \ln \frac{1}{a_{+(NMP)}^m a_{-(NMP)}^m} \quad (4.18)$$

$$a_{+(NMP)}^m = c_+ \gamma_{+(NMP)}^m \quad (4.19)$$

Terms of the form X^m denote the property X in the molality scale, i.e., $X_{(NMP)}^m$ denotes the property X with the unsymmetric reference state in molality scale normalized to unit molality in the solvent NMP, and c_+ is the molality of the protonated amine ion.

The relation between molality- and mole fraction-based standard parameters is given in Equation (4.20):

$$\gamma_{+(NMP)}^m = x_{NMP} \gamma_{+(NMP)}^*, \Delta G_{+(NMP)}^m = \Delta G_{+(NMP)}^* + RT \ln(M_{NMP} c_0) \quad (4.20)$$

where, M_{NMP} is the molecular weight of NMP, and the other terms are as described above.

4.1.1.3 Ions in non-aqueous solutions

Most of the CCS technologies researched so far have been aqueous systems. Therefore, a large amount of data is available for electrolytes that might form during CCS applications in terms of infinite dilution in water. Being able to use those data and avoiding the need to regress data for ions in many different solvents could significantly accelerate research in the field of NASs. The ternary CO₂-AMP-NMP system has thus been re-defined as a quaternary CO₂-AMP-NMP-water system in order to be able to use infinite dilution in water as the reference state for electrolytes in the non-aqueous solution. Since ions only affect the phase equilibrium through chemistry, the system should be thermodynamically consistent, provided the equilibrium constants are inter-derivable, and the standard state properties are used consistently. The difference in equilibrium constants in the two reference states is derived in Equation (4.21) and (4.22) in unsymmetric reference state in molality scale:

$$\ln K_{2(NMP)}^m - \ln K_{2(aq)}^m = - \left(\frac{\Delta G_{+(aq)}^m + \Delta G_{-(aq)}^m - \Delta G_{+(NMP)}^m - \Delta G_{-(NMP)}^m}{RT} \right) \quad (4.21)$$

$$\Delta G_{+(aq)}^m - \Delta G_{+(NMP)}^m = RT \ln \frac{c_{+(NMP)} \gamma_{+(NMP)}^m}{c_{+(aq)} \gamma_{+(aq)}^m} = RT \ln \frac{\frac{n_+ n_{NMP} \gamma_+}{w_{NMP} n_{total} \gamma_{+,NMP}^\infty}}{\frac{n_+ n_{aq} \gamma_+}{w_{aq} n_{total} \gamma_{+,aq}^\infty}} = RT \ln \frac{\gamma_{+,aq}^\infty M_{aq}}{\gamma_{+,NMP}^\infty M_{NMP}} \quad (4.22)$$

where $K_{2(NMP)}^m$ denotes the equilibrium constant in the ternary CO₂-AMP-NMP system, and $K_{2(aq)}^m$ denotes the equilibrium constant in the quaternary CO₂-AMP-NMP-water system, both in molality scale. The terms $\Delta G_{+(aq)}^m$ and $\Delta G_{+(NMP)}^m$ denote the Gibbs energy of the cation in the reference state of infinite dilution, in water and NMP, respectively. c_+ is the molality of the cation in the ternary or quaternary solution with the subscripts (NMP) and (aq), respectively. n_+, n_{NMP}, n_{aq} , and n_{total} are the moles of cation, NMP, water, and total moles in the solution, respectively. w_{NMP} is the mass of NMP in the solution, and w_{aq} is the mass of water in the solution. $\gamma_{+,NMP}^\infty$ and $\gamma_{+,aq}^\infty$ denote the infinite dilution activity coefficients of the cation in NMP and water, respectively. Finally, M_{aq} and M_{NMP} are the molecular weights of water and NMP, respectively.

From Equations (4.21) and (4.22), it is clear that the difference between the equilibrium constants in the two reference states is constant for all concentrations and is inter-derivable. Therefore, properties such as the Gibbs energy of

formation for an ion with the reference state of infinite dilution in water can be used in NASSs.

4.2 Thermodynamic property model

The experiments described in Section 3.1.2 were used to construct a model in ASPEN Plus using the ENRTL-RK property method (which uses the unsymmetric reference state, as discussed in Section 4.1). Two different models were developed in the present work. The first type of experiments, described in Section 3.1.2, performed with an equilibrium time of 30 min (Paper I), were used to develop the first model (Paper II), the procedure for which is presented below. The second model is described later in this section.

The pure component data for most compounds (CO₂, AMP, NMP, N₂, and water) are readily available in the Aspen databases. The data for the Gibbs energy and the enthalpy of formation at infinite dilution in water for both protonated AMP and the AMP carbamate ion, are also available (Sherman, 2016). As it was established in Section 4.1.1.3 that the reference state of infinite dilution in water can be used for ions in NASSs, these data have been added to the model. Some data for the protonated amine ion are available in Aspen databases, while some are user-defined. The data for the AMP carbamate ion is also user-defined. All the user-defined data used for the ions is given in Table 4.1.

Table 4.1. User-defined data for the AMP carbamate ion and the protonated amine ion.

Parameter	Units	$RNHCOO^-$	RNH_3^+
Molecular weight		132.14	
Ion type		4	
Charge of the ion		-1	
Gibbs energy of formation with the reference state of infinite dilution in water	J/kmol	-4.57E+08*	-1.68E+08*
Enthalpy of formation with the reference state of infinite dilution in water	J/kmol	-7.50E+08*	-3.99E+08*
Vapor pressure given by extended Antoine equation	bar	-1E+20	

*From (Sherman, 2016).

The Born term in Equation (4.3) is a function of dielectric constant. Therefore, the dielectric constants for the components in the solution are given according to Equation (4.23). The dielectric constant in the mixture is then averaged in ASPEN Plus according to Equation (4.24).

$$\varepsilon = a + b \left(\frac{1}{T} - \frac{1}{T_{ref}} \right) \quad (4.23)$$

$$\varepsilon_{mix} = \frac{\sum_S x_S M_S \varepsilon_S}{\sum_S x_S M_S} \quad (4.24)$$

Here, a and b are the parameters used to fit the dielectric constant as a function of temperature (shown in Table 4.2), and T_{ref} is the reference temperature, ϵ_S is the dielectric constant given by Equation (4.23), x_S is the mole fraction of component S in the mixture, and M_S is the molecular weight of S .

Table 4.2. Dielectric constants used in the simulation defined in Equation (4.23).

Component	Database	a	b	T_{ref}
NMP	USER*	32.17	15331.0	298.15
H ₂ O	DB-ASPENPCD	78.54	31989.4	298.15
CO ₂	DB-ASPENPCD	1.6	0	293.15
AMP	DB-ELECPURE	22.0	8992.68	298.15
N ₂	DB-ASPENPCD	1.454	0.	70.15

*Using data from George and Sastry, (2004); Hsieh et al., (2007); Pakzad et al., (2018).

Table 4.3. Henry's parameters used in the model according to Equation (4.25).

Component i	Component S	A_H	B_H	C_H	D_H
CO ₂	NMP*	93.9	-369.4	-16.5	0.05855
CO ₂	AMP**	3.29	-820.9	1.7	-0.0027
CO ₂	H ₂ O#	159.2	-8477.7	-22.0	0.0058
N ₂	H ₂ O##	165.0	-8432.8	-21.6	-0.0084

*User-defined based on data from Paper I with $H_{i,S}$ in N/m², valid between 25 and 88 °C.

**User-defined based on data from (Dash et al., 2011; Wang et al., 1992)) with $H_{i,S}$ in kPa, valid between 34.6 and 81.7 °C.

#From Aspen database APV100 ENRTL-RK with $H_{i,S}$ in bar, valid between -0.15 and 226.85 °C.

From Aspen database APV100 BINARY with $H_{i,S}$ in bar, valid between -0.15 and 72.85 °C.

The temperature in K was used to obtain the parameters in the table.

The physical interactions of CO₂ (accounting for Reaction {12}) with the components AMP and NMP are considered using Henry's parameters according to Equation (4.25), which is the expression used in ASPEN Plus. The physical solubility of CO₂ in the mixture is then approximated as in Equation (4.26). The parameters used in the model according to Equation (4.25) are given in Table 4.3.

$$\ln H(T) = \left[A_H + \frac{B_H}{T} + C_H \ln T + D_H T \right] \quad (4.25)$$

$$\ln \left(\frac{H_{i,mix}}{\gamma_i^\infty} \right) = \sum_S w_S \ln \left(\frac{H_{i,S}}{\gamma_{i,S}^\infty} \right), w_S = \frac{x_S (V_S^{*,l})^{\frac{2}{3}}}{\sum_{S'} x_{S'} (V_{S'}^{*,l})^{\frac{2}{3}}} \quad (4.26)$$

Henry's constant, H , is expressed as a function of temperature, T , $H_{i,mix}$ is Henry's constant for component i in the mixture, and $H_{i,S}$ is given by Equation (4.25) for each S in the liquid mixture. x_S is the mole fraction of component S in the mixture, $V_S^{*,l}$ is the liquid molar volume of S , $\gamma_{i,S}^\infty$ is the infinite dilution activity coefficient of CO₂ in component S under the conditions ($x_i \rightarrow 0, x_S \rightarrow 1$) and, finally, γ_i^∞ is the infinite dilution activity coefficient of component i in the

mixture. The basis for Henry's constant was chosen as infinite dilution in the mixed solution.

The interactions for CO₂-AMP and CO₂-NMP are mostly accounted for by Equation (4.25) with parameters given in Table 4.3. The NRTL model, discussed in more detail elsewhere (Aspentech, 2017; Renon and Prausnitz, 1968), is used to model the interactions between the NMP-AMP pair. Using the NRTL model requires fitting the non-randomness factor and the binary interaction parameters in Equations (4.27) and (4.28):

$$A_{ij} = A_{ji} = c_{ij} + d_{ij} (T - 273.15) \quad (4.27)$$

$$\tau_{ij} = a_{ij} + \frac{b_{ij}}{T} + e_{ij} \ln T + f_{ij} T \quad (4.28)$$

where A_{ij} is the non-randomness factor; $A_{ij} = 0$ corresponds to complete mixing, and the further the value of A_{ij} is from 0, the higher the non-ideality of the mixture. The value of the non-randomness factor was set at 0.3 for the regression, as usually recommended (Aspentech, 2017; Renon and Prausnitz, 1968). τ_{ij} is the NRTL binary interaction parameter, and $\tau_{ij} \neq \tau_{ji}$; therefore, both τ_{ij} and τ_{ji} must be regressed. Regression was performed using data from Karlsson and Svensson (2017), and the results of the regression are given in Table 4.4.

Table 4.4. NRTL parameters for AMP-NMP according to Equation (4.28).

a_{ij}	a_{ji}	b_{ij}	b_{ji}
8.1354	0.1218	-3633.97	506.77

The molecule-ion pair interaction parameters include interactions between the NMP-ion pair, the AMP-ion pair, the CO₂-ion pair, the ion pair-CO₂, the ion pair-AMP, and the ion pair-NMP. The electrolyte NRTL parameters were regressed using the ternary AMP-NMP-CO₂ data obtained when precipitation did not take place. This regression was performed to fit Equations (4.29) and (4.30), and the results are given in Table 4.5. An insignificant amount of water (1E-10 mole fraction) was added to the ternary data sets used for regression of these parameters. The data were taken from (Svensson et al., 2014a; Svensson and Karlsson, 2018), and from Paper I. The parameters for the NMP-ion pair and the ion pair-NMP were prioritized in the regression, and the others were set at recommended values of 15 and -8 for the CO₂-ion pair and the ion pair-CO₂ respectively, and 10 and -2 for the AMP-ion pair and the ion pair-AMP, respectively (Renon and Prausnitz, 1968).

$$\tau_{m,ca} = C_{m,ca} + \frac{D_{m,ca}}{T} + E_{m,ca} \left[\frac{T_{ref}-T}{T} + \ln \left(\frac{T}{T_{ref}} \right) \right] \quad (4.29)$$

$$\tau_{ca,m} = C_{ca,m} + \frac{D_{ca,m}}{T} + E_{ca,m} \left[\frac{T_{ref}-T}{T} + \ln \left(\frac{T}{T_{ref}} \right) \right] \quad (4.30)$$

$C_{m,ca}$, $C_{ca,m}$, $D_{m,ca}$, $D_{ca,m}$, $E_{m,ca}$, and $E_{ca,m}$ are parameters that can be regressed from experimental data, and T_{ref} is the reference temperature. The non-randomness factors were set to a default value of 0.1 for the NMP-ion pair, the AMP-ion pair and the CO₂-ion pair, as recommended by (Renon and Prausnitz, 1968). The terms $E_{m,ca}$ and $E_{ca,m}$ were left at their default values of zero. The terms $C_{m,ca}$ and $C_{ca,m}$ were regressed first. No improvement was observed upon adding $D_{m,ca}$ and $D_{ca,m}$ and hence, these terms were disregarded.

Table 4.5. Electrolyte pair parameters for NMP-ion pair according to Equations (4.29) and (4.30).

$C_{m,ca}$	$C_{ca,m}$
-8.2606	13.1056

The structure of the precipitate (shown in Figure 4.2) was added to the model. The standard state ideal gas enthalpy of formation of the precipitate was estimated using the JOBACK method (Calle, 2018), which is a method based on group contribution (Joback and Reid, 1987). The molar volume and molar heat capacity were added as temperature-independent constants (Calle, 2018); the values of which are given in Table 4.6.

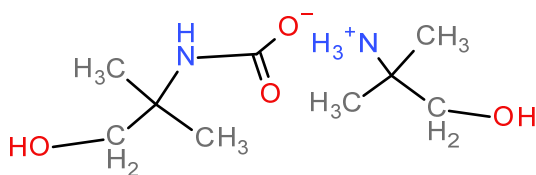


Figure 4.2. Structure of the precipitate.

Table 4.6. User-defined pure component parameters for the precipitate.

Parameter	Units	Value	Remarks
Molecular weight		222.285	
Ideal gas enthalpy of formation of the precipitate	J/kmol	-9.26E+08*	Estimated using the JOBACK method
Molar volume of the precipitate	m ³ /kmol	0.183101*	
Molar heat capacity of the precipitate	J/kmol-K	358746*	

*From Calle, (2018).

The equilibrium constants for the reactions involved were expressed as in Equation (4.31).

$$\ln K = A_K + \frac{B_K}{T} \quad (4.31)$$

It was established in Section 4.1.1.3 that infinite dilution in water can be used as a reference state for ions in this system, and the Gibbs free energy and enthalpy of formation of the ions in this reference state can be found in Table 4.1. The equilibrium constant can be expressed in terms of the Gibbs energies as in Equations (4.32) and (4.33), for Reactions {13} and {11}, respectively.

$$\ln K_{1(aq)} = -\frac{\Delta G_{RNH_3^+(aq)}^* + \Delta G_{RNHCOO^-(aq)}^* - \Delta G_{CO_2(sol)}^* - 2\Delta G_{RNH_2(l)}^0}{RT} = \ln \frac{a_{RNH_3^+(aq)}^* a_{RNHCOO^-(aq)}^*}{a_{CO_2(sol)}^* a_{RNH_2(l)}^{02}} \quad (4.32)$$

$$\ln K_{2(aq)} = -\frac{\Delta G_{RNH_3^+RNHCOO^-}^{0,s} - \Delta G_{RNH_3^+(aq)}^* - \Delta G_{RNHCOO^-(aq)}^*}{RT} = \ln \frac{1}{a_{RNH_3^+(aq)}^* a_{RNHCOO^-(aq)}^*} \quad (4.33)$$

Differentiating Equations (4.31) to (4.33) gives Equations (4.34) to (4.36):

$$\frac{d \ln K}{dT} = -\frac{B_K}{T^2} \quad (4.34)$$

$$\frac{d \ln K_1}{dT} = \frac{\Delta H_{RNH_3^+(aq)}^* + \Delta H_{RNHCOO^-(aq)}^* - \Delta H_{CO_2(sol)}^* - 2\Delta H_{RNH_2(l)}^0}{RT^2} \quad (4.35)$$

$$\frac{d \ln K_2}{dT} = \frac{\Delta H_{RNH_3^+RNHCOO^-}^{0,s} - \Delta H_{RNH_3^+(aq)}^* - \Delta H_{RNHCOO^-(aq)}^*}{RT^2} \quad (4.36)$$

The equilibrium constant for Reaction {13} is already defined in terms of Equation (4.31) since the Gibbs energy and enthalpy of formation are available or given for all the components involved in that reaction. For Reaction {11}, the equilibrium constant can be regressed using ternary experimental data with precipitation. As mentioned above, an insignificant amount of water was added to accommodate the need for some water, since infinite dilution in water was used as the reference state. The data at 25 °C were used to obtain the term A_K , and data at all available temperatures were used to obtain the term B_K . The values of A_K and B_K are given in Table 4.7.

Table 4.7. Parameters in Equation (4.31) for the reverse of Reaction {11}.

A_K	B_K
-10.1971	360.36

The Gibbs energy and enthalpy of solid formation of the precipitate were then calculated using Equations (4.33) and (4.36). The values obtained are given in Table 4.8.

Table 4.8. Gibbs energy and enthalpy of solid formation for the precipitate (Paper II).

Property	Unit	Value
$\Delta G_{RNH_3^+ RNHCOO^-}^{0,s}$	J/kmol-K	-6.473E+08
$\Delta H_{RNH_3^+ RNHCOO^-}^{0,s}$	J/kmol-K	-1.146E+09

The option codes used in the model are given in Table 4.9. Option codes 1 to 4 indicate the following: 1) the PDH term was considered as in Equation (4.3), 2) the dielectric constant was calculated according to Equation (4.24) with parameters defined in Table 4.2, 3) the density of water was calculated from steam tables (left at default), and 4) the reference state was infinite dilution in water (Aspentech, 2017).

Table 4.9. The option codes used in the model.

Option code	1	2	3	4
Value	0	1	0	0

As mentioned above, the model was updated using results from the second type of experiments described in Section 3.1.2 (Paper IV). The thermodynamic models described in Paper IV and Paper II are similar, apart from the results given in Tables 4.7 and 4.8. The equilibrium constant for Reaction {11} was updated using results from the experiments performed with an equilibrium time of at least 330 min. However, all the results obtained from this type of experiments were not used in the new regression. In the 15AN solutions, equilibrium took 920 min for loading as high as 0.45. In contrast, precipitation occurred immediately in 25AN solutions at loading as low as 0.14. It is thus likely that the experiments with 25AN are closer to true equilibrium, and thus only the data obtained from the 25AN solutions were used in the regression. Also, only the data points where the solution was completely saturated with CO₂ at the end of the experiment were used in the regression, i.e., only the points where the partial pressure of CO₂ in the reactor was greater than zero were used. The updated Gibbs energy and enthalpy of solid formation for the precipitate are given in Table 4.10.

Table 4.10. Gibbs energy and enthalpy of solid formation for the precipitate (Paper IV).

Property	Units	Value
$\Delta G_{RNH_3^+ RNHCOO^-}^{0,s}$	J/kmol-K	-6.531E+08
$\Delta H_{RNH_3^+ RNHCOO^-}^{0,s}$	J/kmol-K	-1.289E+09

4.3 Discussion

The experimental data shown in Figure 3.3 are compared to the estimates made with the first model in Figure 4.3. The model estimates and experimental data are in good agreement at high temperatures. However, as the temperature is lowered, the model and experiments agree only at lower loadings. As the loading increases, the model indicates a change in the reaction mechanism much earlier than the experimental data. This agrees with the results shown in Figure 3.4, where, on extending the equilibrium time to more than 330 min, precipitation occurred much earlier than when the equilibrium time was only 30 min.

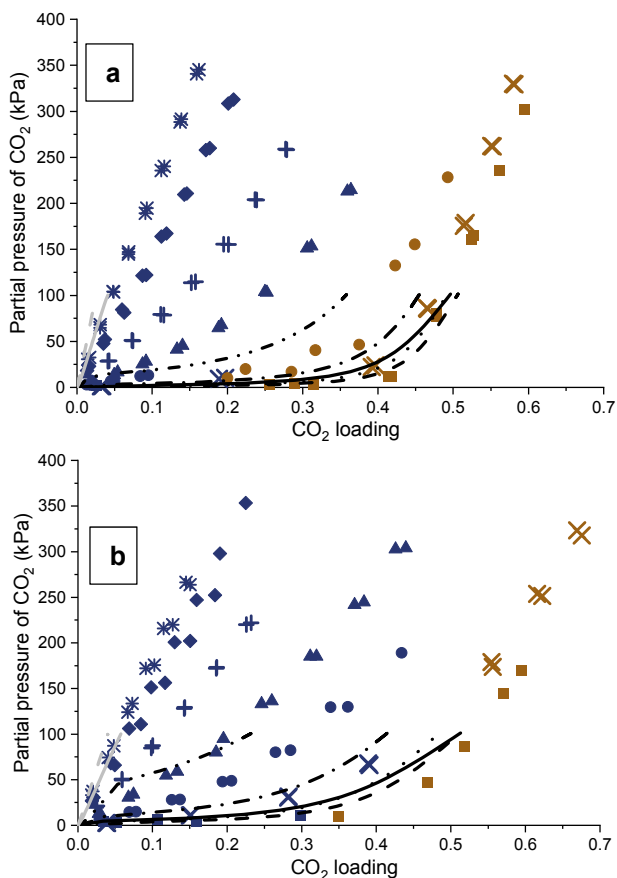


Figure 4.3. Estimates of the solubility of CO₂ in AMP-NMP solutions obtained from the model (lines) compared with the experimental data (points) for: a) 25AN and b) 15AN. The explanation for the symbols is as follows: blue symbols = precipitation did not occur, brown symbols = precipitation occurred, ■ = 25 °C, X = 40 °C, ● = 50 °C, ▲ = 60 °C, + = 70 °C, ◆ = 80 °C, ✕ = 88 °C, (—) = 25 °C, (---) = 40 °C, (···) = 50 °C, (- · -) = 60 °C, (- · ·) = 70 °C, (—) = 80 °C, and (- -) = 88 °C. The sources of the data are as follows: 25, 50 °C = Svensson et al., (2014a), 40, 88 °C = Svensson and Karlsson, (2018), 60, 70, 80 °C = Paper I, Model estimates = Paper II.

The model presented in Paper II was updated with the experimental data presented in Paper IV, obtained with an equilibrium time of >330 min (as described in Section 4.2). Figure 4.4 shows the results obtained from the experiments with extended equilibrium time at 25, 40 and 60 °C, the results from the experiments with 30 min equilibrium time at 70, 80 and 88 °C, and compares them with the estimates of the updated thermodynamic model described in Paper IV. The agreement between the model and the experimental data is much better in Figure 4.4 compared to that in Figure 4.3. In Figure 4.4, the model seems to agree well with the experimental data at 25 °C. At 40 °C, the model and the experiments agree well for the 25AN solution, but some disagreement can be seen for the 15AN solution. The model predicts precipitation at much lower loadings than seen in the experiments for 15AN at 40 °C. In the case of the 25AN solution the thermodynamic model predicts precipitation at a loading of 0.06 at 60 °C, while in 15AN, precipitation is predicted at a loading of 0.2 at 60 °C. However, no precipitation was observed in the experiments with 25AN and 15AN under these conditions, even after equilibrium times of 330 min and 1 000 min, respectively. This could be because the experiments were not run for a sufficiently long time, or the model is not accurate in its prediction of precipitation. At 70 °C, the model predicts precipitation while no precipitation was observed experimentally. However, these experiments were only equilibrated for 30 min. At 80 and 88 °C, the model overpredicts the partial pressure at a given loading, particularly in the 25AN solution (Figure 4.3 and Figure 4.4).

The models described in this chapter were developed using experiments performed with solutions of 15AN and/or 25AN. These concentrations are reasonable for a traditional capture plant design (such as that shown in Figure 2.1), which could be used for a non-aqueous non-precipitating system such as with 15AN solution (as discussed in Section 3.2.1). The estimates of the thermodynamic property model shown in Figure 4.4 were considered sufficiently good to model a full-scale CO₂ capture plant using an AMP-NMP solution to further evaluate the system with the plant design shown in Figure 2.1, and to assess possible energy savings. However, if a plant with phase separation, as shown in Figure 2.5, is to be designed, data obtained using solutions with higher AMP concentrations should be used in the regression to ensure validity over the whole range of operating conditions. In addition, the methodology developed has certain limitations. As can be seen from Equation (4.22), there may be a slight thermodynamic inconsistency in the system as the total number of moles in the ternary CO₂-AMP-NMP system and the quaternary CO₂-AMP-NMP-water system are not the same. Hence, the amount of water added to the system must be very small. However, low mole fractions can cause convergence problems in the simulation.

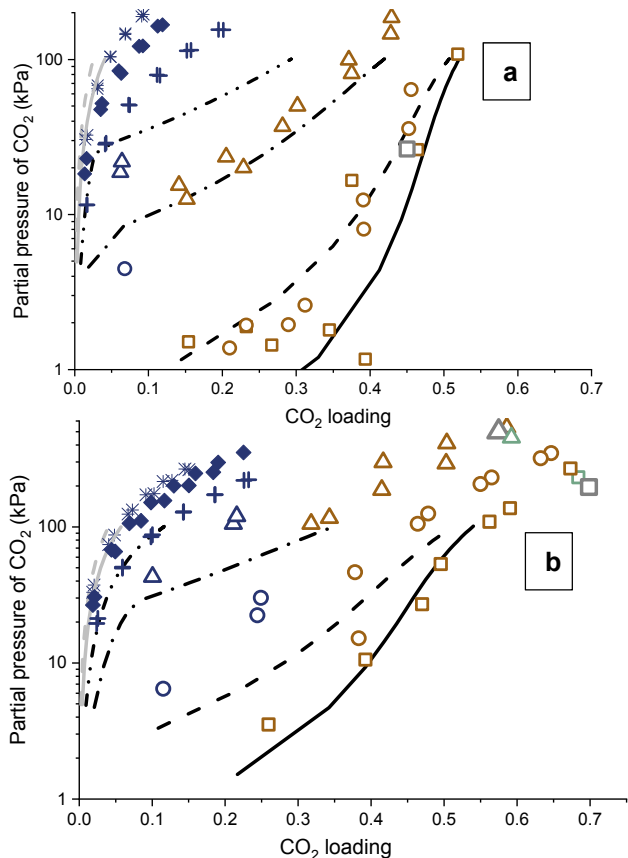


Figure 4.4. Estimates of the solubility of CO₂ in AMP-NMP solutions obtained from the model (lines) compared with the experimental data (points) for: a) 25AN and b) 15AN. The explanation for the symbols is as follows: blue symbols = precipitation did not occur, brown symbols = precipitation occurred, gray symbols = intermediate points before precipitation, green points = equilibrium after precipitation that corresponds to the gray points, □ = 25 °C, 330 min, ○ = 40 °C, 330 min, Δ = 60 °C, 330 min, + = 70 °C, 30 min, ◆ = 80 °C, 30 min, ✕ = 88 °C, 30 min, (—) = 25 °C, (---) = 40 °C, (- · -) = 60 °C, (- · ·) = 70 °C, (- - -) = 80 °C, and (- · - ·) = 88 °C. The sources for the data are as follows: 25, 40 and 60 °C = Paper IV, 70 and 80 °C = Paper I, 88 °C = Svensson and Karlsson, (2018), model estimates = Paper IV.

Yet another limitation of the methodology is the mathematical complexity introduced into the regression process by the addition of water into the system. On the one hand, it is important that the property model obtained for AMP (or any other amine) in a non-aqueous solvent is thoroughly rigorous in one solvent so that the transferable parameters can be applied to other solvents without further regression. This means a small residual root mean square error (rrmse) is desired. On the other hand, the rrmse cannot be as low as expected for the ternary CO₂-AMP-NMP system due to the added complexity in the regression arising from the presence of water. This means that it must be treated mathematically as a quaternary CO₂-AMP-NMP-water system which would have a higher rrmse.

As mentioned at the beginning of this chapter, the model was mainly developed to answer RQ1, which was divided into RQ1.1, and RQ1.2. The question RQ1.1 has been shown to be satisfactorily answered in this chapter. The NAS AMP-NMP has been modelled using the unsymmetric ENRTL-RK property method. The model could also have been developed using the symmetric reference state defined in Equations (4.7) to (4.9). The corresponding property method in ASPEN Plus is called ENRTL-SR (Simoni et al., 2008; Song and Chen, 2009). However, to reduce the research efforts for future systems with AMP in other solvents, using the unsymmetric reference state provides the benefit of being able to directly transfer parameters. Therefore, this reference state was preferred in view of RQ1.2. While the reference states are inter-derivable, an unsymmetric reference state (with infinite dilution in water) allows parameters obtained with AMP in one solvent to be used when modelling CO₂ capture with AMP in other solvents. Yet another option to consider with regard to RQ1.1 would be to test extended UNIQUAC, a property method also used for electrolytic systems (Thomsen, 1997), in NAS applications, which could be considered in future work.

Ideally, a better fit could be expected from a model. However, the quality of the fit is probably the result of the experimental data used. To transfer parameters developed for AMP in one solvent to AMP in another solvent, i.e., to answer RQ1.2, it is first necessary to obtain a property model that is reliable for AMP in a particular solvent. Some of the parameters, such as the equilibrium constants for a given reaction, could then be extended to AMP in other solvents. An obvious way to improve the experimental data is to extend the equilibrium time even further, however, this is not practical as discussed in Section 3.2.1. Another way of achieving this is based on an extension of the theory discussed in Section 4.1.1.3 to other solvents. It is known qualitatively from the solubility experiments in Section 3.2.1 that the crystallization prevents the system from reaching true equilibrium. The kinetics of crystallization can be affected by changing the solvent. A direct implication seen from Equations (4.21) and (4.22) is that the equilibrium constant regressed for a reaction in one solvent can be applied to the reaction in another solvent (theoretically answering RQ1.2). Therefore, if the equilibrium constant is obtained in a solvent where Reaction {11} is fast, it can be applied to that reaction in all the other solvents.

In addition to answering RQ1, the research presented in this chapter provides valuable information that is required to test the theory developed to answer RQ2. Figure 4.5a shows the logarithm of the activity of the carbamate ion as a function of temperature, obtained using the thermodynamic model presented in Paper IV at two different pressures.

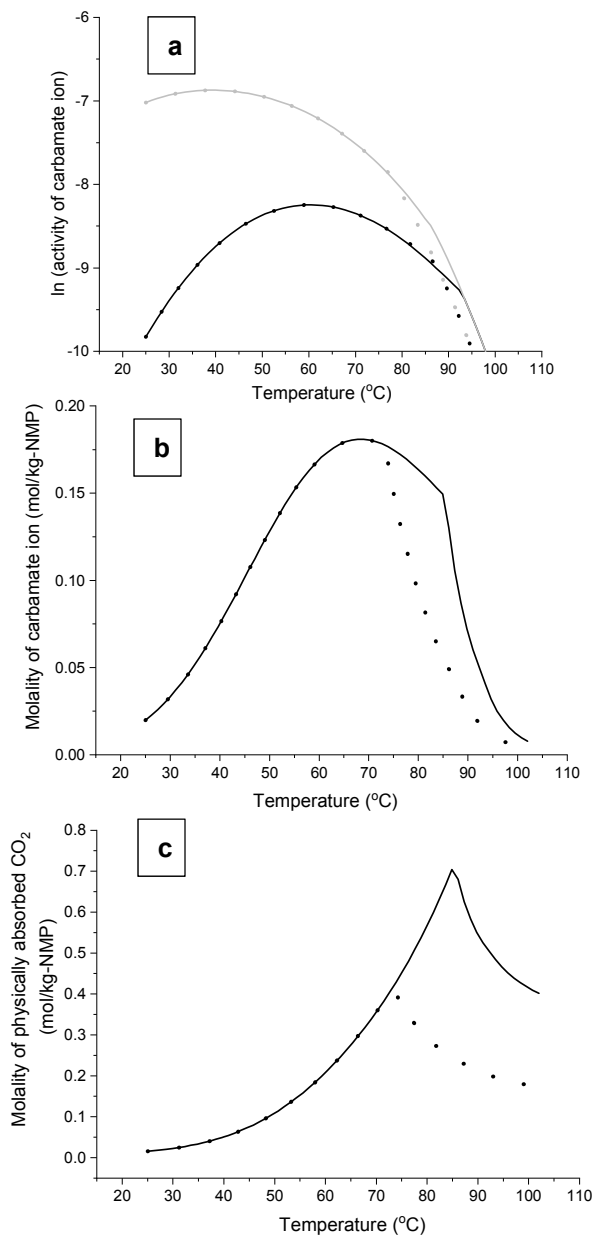


Figure 4.5. Plots of: a) the logarithm of the activity of the carbamate ion b) the molality of carbamate ion and c) the molality of physically dissolved CO₂ versus temperature, obtained using the thermodynamic model described in Paper IV for a loading of 0.448 in a 25AN solution at 709 kPa (—) and 304 kPa (···). The logarithm of the activity of the carbamate ion is also plotted with temperature without the precipitation reaction, i.e., without Reaction {11} at 709 kPa (—) and 304 kPa (···).

For a solution at equilibrium with the precipitate, dissolved CO₂, and carbamate ions, at 25 °C and 709 kPa, the reaction equilibrium, shown in Reactions {12}, {13}, and {11}, moves to the left upon increasing the temperature. This leads to a curve, the shape of which depend on the temperature dependency of the equilibrium constants (for Reactions {13} and {11}) and Henry's constant (for Reaction {12}). This is in contrast to the behavior of the simple liquid-solid systems shown in Figure 2.7a. Eventually, at temperatures higher than the dissolution temperature of the precipitate (93 °C at 709 kPa), there is no further contribution to the carbamate activity from Reaction {11}, and a clear change in shape is observed. This point of discontinuity in the black curves in Figure 4.5a is the point of dissolution according to the model. It is worth noting that the visually observed dissolution temperature in the experiments performed to determine the crystallization kinetics was between 87 and 88 °C for a loading of 0.448 (see Chapter 5). The model thus appears to overestimate the dissolution temperature by 5 to 6 °C. On cooling after dissolution, carbamate ions (and protonated amine ions) form in the solution along the gray lines shown in Figure 4.5a. Once the meta-stable zone has been crossed, precipitation takes place until the lower equilibrium curve in Figure 4.5a is reached. The supersaturation can be calculated as the difference between the equilibrium curve and the no precipitation curve at the temperature of crystallization. This behavior is much more complex than that seen in Figure 2.7a, and must be accounted for in order to determine the crystallization kinetics, as described in the next chapter.

The behavior of any component in the system with temperature can be predicted with the thermodynamic model. The molality of the carbamate ion and the physically dissolved CO₂ are plotted in Figure 4.5b and 4.5c, respectively. Figure 4.5b can be compared to the lines in Figure 3.5, where the salt solubility was measured in the test tube, as described in Section 3.1.3. As can be seen from the figures, the molality of carbamate ion (Figure 4.5b) is lower than the solubility of the salt (Figure 3.5) measured in the test tube. This is an expected result since the salt solubility shown in Figure 3.5 includes not just the carbamate ion, but also the physically dissolved CO₂ and the released CO₂ as described in Section 3.1.3. Furthermore, Figure 4.5b shows that the molality of CO₂ decreases after reaching a maximum unlike the behavior in Figure 3.5. This highlights the limitation of the method described in Section 3.1.3 for measuring the solubility of the salt. Additionally, from Figure 4.5c it can be seen that the amount of physically dissolved CO₂ is comparable to that of the carbamate ion concentration in Figure 4.5b. This suggests that the attempt to avoid CO₂ release in Section 3.1.3 would not have been enough to use Equation (3.4). Therefore, the thermodynamic model is a much better way of estimating the concentrations for the crystallization kinetics in Chapter 5.

5 Crystallization Kinetics for Precipitating Systems

Understanding crystallization kinetics is important in designing the crystallization unit. This chapter is concerned with the topic of crystallization, i.e., answering RQ2. This research question was further divided into the following five parts:

RQ2.1. Is the traditional power law relation adequate to model the crystallization kinetics of the AMP-NMP system?

RQ2.2. Is it sufficient to avoid CO₂ release during experiments when applying the traditional power law relation to the AMP-NMP system?

RQ2.3. How does the width of the meta-stable zone vary in the case of AMP-NMP system?

RQ2.4. Can the crystallization kinetics theory developed for an amine in an organic solvent be used to reduce the research efforts required for the same amine in other solvents?

RQ2.5. Can the proposed crystallization kinetics theory be applied to other precipitating CCS systems?

RQ2.1 was the focus of Papers III and IV, while RQ2.2 and RQ2.3 were the focus of Paper IV. RQ2.4 and RQ2.5 are discussed theoretically in Section 5.3 with regard to the potential of the methodology developed.

5.1 Theory

Several theories, described in detail elsewhere (Sangwal, 2018) are available for determining the crystallization kinetics of a simple liquid-solid system shown in Figure 2.7a. A power law relation is used here as it simplifies all the physically significant terms to two empirical parameters. Thus, the focus is on the theoretical changes in the crystallization process due to the additional complexity of CCS

applications and not on the already established crystallization process itself. A more physically significant theory can then be applied to the CCS applications based on the knowledge gained from the power law relation. To determine the crystallization kinetics of the AMP-NMP system, the reaction mechanism described in Chapter 4, i.e., the reaction mechanism is as described by Reactions {12}, {13}, and {11}, has been employed.

Supersaturation is expressed as the supersaturation ratio S , the relative supersaturation σ , or as a difference Δ in activity or concentration based on the definition of the supersaturation. Activity and concentration refer to the ions that constitute the precipitating salt, i.e., the carbamate and protonated amine ions. Concentration is expressed in terms of molality throughout this chapter. The expressions for supersaturation are given in terms of activity in Equations (5.1) to (5.3):

$$S_a = \frac{a_{\pm}}{a_{\pm}^s} \quad (5.1)$$

$$\sigma_a = \frac{\Delta a_{\pm}}{a_{\pm}^s} \quad (5.2)$$

$$\Delta a = a_{\pm} - a_{\pm}^s \quad (5.3)$$

where the activity, a , can be written $c \cdot \gamma^m$, where c is the molality of the ions in moles per kg NMP, and γ^m refers to the molality-based activity coefficient of the ions (see Section 4.1.1.2). The subscript \pm denotes the mean ionic property as described in Equation (4.8); $a_{\pm} = (a_+^{v_+} a_-^{v_-})^{1/(v_+ + v_-)} = (a_+ a_-)^{0.5}$. If more than one anion or cation is present in the system, a_+ and a_- would have different values. In the present case, $a_{\pm} = a_+ = a_- = a$. The superscript s refers to the property at saturation. The supersaturation is sometimes expressed in terms of concentration by neglecting the activity coefficient, in which case, Equations (5.1) to (5.3) become Equations (5.4) to (5.6):

$$S_c = \frac{c_{\pm}}{c_{\pm}^s} \quad (5.4)$$

$$\sigma_c = \frac{\Delta c_{\pm}}{c_{\pm}^s} \quad (5.5)$$

$$\Delta c = c_{\pm} - c_{\pm}^s \quad (5.6)$$

The subscript \pm is dropped for brevity throughout the rest of the chapter. All these definitions of supersaturation are inter-related. For low supersaturations, Equation (5.7) is valid:

$$\ln S_a = \ln(1 + \sigma_a) \approx \sigma_a \approx \text{constant} \cdot \Delta a \quad (5.7)$$

where the term, $1/a^S$ in Equation (5.2), which is not necessarily constant (for example, with temperature) is considered a constant. Similar relations can be derived in terms of concentration, when the activity coefficient is neglected. Equation (5.8) can be obtained from Equations (5.4) to (5.6).

$$\ln S_c = \ln(1 + \sigma_c) \approx \sigma_c \approx \text{constant} \cdot \Delta c \quad (5.8)$$

5.1.1 Traditional power law kinetics

Traditionally, the power law relation given in Equation (5.9) has been applied in terms of concentration for the case shown in Reaction {10}. In the case of simple liquid-solid chemistry, the relation between activity and temperature is that shown in Figure 2.7a. However, the effect of the activity coefficients is here assumed to be negligible, and the power law relation is applied in terms of concentration.

To estimate the crystallization kinetics or rate of formation of the precipitate $\left(\frac{dm}{dt}\right)$ according to power law relation, the parameters k and p in Equation (5.9) must be determined (Mullin, 2001).

$$\frac{dm}{dt} = k(\Delta c)^p \Rightarrow \ln\left(\frac{dm}{dt}\right) = \ln k + p \cdot \ln(\Delta c) \quad (5.9)$$

The supersaturation of the solution, Δc , is given in Equation (5.6) and can be expressed in terms of the width of the temperature-based meta-stable zone (MSW), as shown in Figure 2.7a. The experimental procedure involves heating a solution in equilibrium with crystals until dissolution, and then cooling it until re-crystallization takes place. The difference between temperature at which the crystals dissolve and that at which re-crystallization occurs is the temperature-based MSW. In the case of Figure 2.7a, Δc can be expressed as in Equation (5.10):

$$\Delta c = \frac{dc^S}{dT}(\Delta T) \quad (5.10)$$

where, ΔT is the temperature-based MSW (see Figure 2.7a) and dc^S/dT is the slope of the equilibrium curve expressed in terms of concentration (note that in Figure 2.7a, the equilibrium curve is shown in terms of activity). In the case of Figure 2.7a, a mole balance for the precipitate can be written according to Equation (5.11):

$$\frac{dm}{dt} = \frac{dc^S}{dt} + \frac{d(\Delta c)}{dt} \quad (5.11)$$

That is to say, all the precipitate is formed from the conversion of the ion concentration and consumption of supersaturation. This is not true for most precipitating CCS applications. If precipitation promotes CO₂ absorption, the gas phase also participates in the above mole balance. This is probably the reason why CO₂ release was avoided or minimized in previous experiments performed to determine the crystallization kinetics of the salts formed from CO₂ absorption, as discussed in Section 2.2 (Sutter et al., 2014; Wu et al., 2017a). However, it is not necessarily enough to avoid the release of gaseous CO₂. For example, AMP-NMP, being a non-aqueous precipitating system, has significant amounts of physically dissolved CO₂. As seen from Figure 4.5c, the physically dissolved CO₂ changes considerably with temperature and should be considered in the mole balance of Equation (5.11). Furthermore, in the case of AMP-NMP, it has not been possible to avoid CO₂ release, as discussed in Section 3.2.2. Using Equation (5.11) for the AMP-NMP system would mean neglecting changes in both the physically dissolved CO₂ and released CO₂ contributing to the mole balance.

The point in time when the term $\frac{d(\Delta c)}{dt}$ in Equation (5.11) equals zero is usually defined as the crystallization point. Initially, it was assumed that as soon as nucleation began, the rate of formation of supersaturation was equal to the rate of consumption of supersaturation and the net change in supersaturation over time is zero. However, the point in time when nucleation is detectable includes the growth of crystals to detectable sizes together with nucleation and the above assumption is not valid (Mullin, 2001; Nývlt, 1983). Nevertheless, there is a point at which $\frac{d(\Delta c)}{dt}$ is equal to zero; when the supersaturation reaches a maximum. The point of crystallization is henceforth defined as the point when Δc goes through a maximum. Crystal growth kinetics must be determined separately and combined with the power law relation obtained here to completely define the crystallization process.

At the point of crystallization, Equation (5.11) can be written as Equation (5.12):

$$\frac{dm}{dt} = \frac{dc^s}{dt} = \frac{dc^s}{dT} \cdot \frac{dT}{dt} \quad (5.12)$$

Combining Equations (5.9) to (5.12) gives Equation (5.13), which shows that the kinetic parameters for crystallization can be estimated by plotting $\ln(-\Delta T)$ vs. $\ln\left(-\frac{dT}{dt}\right)$, if the term $\frac{dc^s}{dT}$ is known.

$$\ln(-\Delta T) = -\frac{1}{p} \ln k + \frac{1-p}{p} \ln\left(\frac{dc^s}{dT}\right) + \frac{1}{p} \ln\left(-\frac{dT}{dt}\right) \quad (5.13)$$

The term $\frac{dc^s}{dT}$ is the slope of the solubility curve traditionally estimated at the saturation temperature. By observing the origin of the term $\frac{dc^s}{dT}$, it can be seen that it has two contributions. The first is the result of mole balance for the precipitate from Equation (5.11) at the point of crystallization, and the second is the result of supersaturation built up from the point of dissolution (Equation (5.10)). In the case of Figure 2.7a, in terms of activity, the temperature derivative at the point of crystallization is the same as that at the point of dissolution. These terms can, therefore, be added, as in Equation (5.13). In terms of concentration, an error may be introduced unless the effect of the activity coefficient is negligible. The term $\frac{dc^s}{dT}$ was determined by differentiating Equation (3.3) to obtain Equation (5.14) (Paper III).

$$\frac{dc^s}{dT} = B_s c^s \quad (5.14)$$

5.1.2 Proposed power law kinetics

To overcome the shortcomings of the power law relation discussed in Section 5.1.1, the following modifications were proposed (Paper IV). The theory was developed based on activity, and the rate of formation of solid is expressed in units of molality per min. To determine the crystallization kinetics, k' and p' in Equation (5.15) must be determined (Mullin, 2001):

$$\frac{dm}{dt} = k' \cdot \left(\frac{\Delta\mu}{RT}\right)^{p'} \quad (5.15)$$

where m denotes the moles of solid per kg NMP, R is the universal gas constant, T is the temperature, and $\Delta\mu$ is the driving force in terms of the chemical potential given by Equation (5.16):

$$\Delta\mu = \mu - \mu^s = \nu RT \ln S_a \quad (5.16)$$

where, S_a is the activity-based supersaturation ratio, and is related to Δc in Equation (5.9) by the relations in Equations (5.1) to (5.8). ν is the number of moles of ions in 1 mole of solute (solute in this chapter refers to the salt alone); $\nu = 2$ for the current system, according to Reaction {11}. μ is the chemical potential at any given time t , while μ^s is the chemical potential under saturation conditions (of dissolved solids in liquid).

A mole balance similar to that given in Equation (5.11) is performed in Equation (5.17) below. The mass of NMP in the solution, w_{NMP} , is assumed to be constant and equal to the initial mass in the solution. The CO_2 is present either in gas form

(denoted g), or in the liquid phase (denoted c) as dissolved CO_2 (with the subscript CO_2), or as the carbamate ion (subscript $-$), or in the solid phase (denoted m) as the precipitate. To ensure the same units for all the terms, the gaseous CO_2 is divided by w_{NMP} and is referred to as the “concentration” or “molality” of gaseous CO_2 . Unlike Equation (5.11), Equation (5.17) considers all components involved in the mole balance, minimizing any error caused by evolved CO_2 . It is also clear from Equation (5.17) that avoiding CO_2 release into the gas phase is not sufficient to apply the traditional crystallization kinetic theories. One must ensure that no change takes place in any of the components except the ions forming the salt in order to reduce Equation (5.17) to (5.11).

$$\frac{dm}{dt} + \frac{dc_-}{dt} + \frac{dc_{\text{CO}_2}}{dt} + \frac{1000}{w_{\text{NMP}}} \frac{dg_{\text{CO}_2}}{dt} = 0 \Rightarrow \frac{dm}{dt} + \frac{d(\Delta c_- + c_-^s)}{dt} + \frac{dc_{\text{CO}_2}}{dt} + \frac{1000}{w_{\text{NMP}}} \frac{dg_{\text{CO}_2}}{dt} = 0 \quad (5.17)$$

It is also worth noting that Reactions {13} and {12} are assumed to be in equilibrium, and Reaction {11} is considered the rate-determining step, the rate of which is given by Equation (5.15). When the reactor is filled with AMP-NMP solution and CO_2 is injected, the pressure and true heat flow seem to be in apparent equilibrium until the pressure starts to decrease, a peak in true heat starts to appear, and precipitation takes place simultaneously (Svensson et al., 2014a). This shows that Reaction {11} is indeed the rate-limiting step.

The definition of the point of crystallization is still expressed as the point at which $\frac{d(\Delta c_-)}{dt} = 0$, and $\frac{dm}{dt}$ can be expressed as in Equation (5.18).

$$\frac{dm}{dt} = -\frac{dc_-^s}{dt} - \frac{dc_{\text{CO}_2}}{dt} - \frac{1000}{w_{\text{NMP}}} \frac{dg_{\text{CO}_2}}{dt} \quad (5.18)$$

The concentrations in Equation (5.18) can be varied by using a constant cooling rate $\left(-\frac{dT}{dt}\right)$, and Equation (5.19) is obtained.

$$\frac{dm}{dt} = \left(\frac{dc_-^s}{dT} + \frac{dc_{\text{CO}_2}}{dT} + \frac{1000}{w_{\text{NMP}}} \frac{dg_{\text{CO}_2}}{dT}\right) \left(-\frac{dT}{dt}\right) \quad (5.19)$$

Figure 4.5a shows the saturation activity as a function of temperature for the AMP-NMP system. As mentioned in Section 4.3, the supersaturation, $\ln S_a$, can be calculated as the difference between the equilibrium curve with and without precipitation at the temperature of crystallization in Figure 4.5a.

Combining Equations (5.15), (5.16), and (5.19), gives Equation (5.20):

$$\ln\left(\frac{dc^S}{dT} + \frac{dc_{CO_2}}{dT} + \frac{1000}{w_{NMP}} \frac{dg_{CO_2}}{dT}\right) + \ln\left(-\frac{dT}{dt}\right) = \ln k' + p' \cdot \ln(2 \ln S_a) \quad (5.20)$$

The parameters, k' and p' , can then be estimated by plotting $\left[\ln\left(\frac{dc^S}{dT} + \frac{dc_{CO_2}}{dT} + \frac{1000}{w_{NMP}} \frac{dg_{CO_2}}{dT}\right) + \ln\left(-\frac{dT}{dt}\right)\right]$ vs. $\ln(2 \ln S_a)$.

5.2 Experimental procedure

The experiments used to determine the crystallization kinetics were performed in the calorimeter shown in Figure 3.1. Two different sets of experiments were performed: preliminary experiments described in Paper III, and the second set were refined based on observations from the preliminary experiments (described in Paper IV). The experimental procedures for both are described below.

In the first set of experiments (Paper III), 100 g of solution was added to the reactor (AMP in NMP or TEGDME) and the system was evacuated for 10-12 s at 25 °C. The temperature was then increased to 50 °C. CO₂ was added at 50 °C in batches of injections using a Bronkhorst Hi-Tec mass flow controller. The system was then allowed to reach equilibrium, defined as stability in pressure (within ±0.005 bar) and true heat flow (within ±0.02 W) for 15 min. The solution was then heated until dissolution. The temperature setting in the calorimeter was employed for the heating step. This does not guarantee that the heating procedure is always the same, only that the set temperature is reached. The temperature was increased intermittently until dissolution was observed. Following dissolution, cooling rates between 0.1 and 1.5 °C/min were employed, and the system was cooled until re-crystallization took place. The process was repeated with a different cooling rate.

The temperature at which the salt dissolved was noted visually. These dissolution points are shown in Figures 3.5 and 3.6. The point of crystallization was defined in Section 5.1 as the point at which supersaturation, Δc , reaches a maximum. This point was approximated to the point at which the true heat flow value reaches a maximum. True heat flow depends on the extent to which Reactions {12}, {13}, and {11} take place and is also a function of activity and not concentration. The crystallization parameters can then be calculated from Equation (5.13) using Equation (5.14). The saturation solubility can be calculated at the dissolution temperature using Equation (3.4).

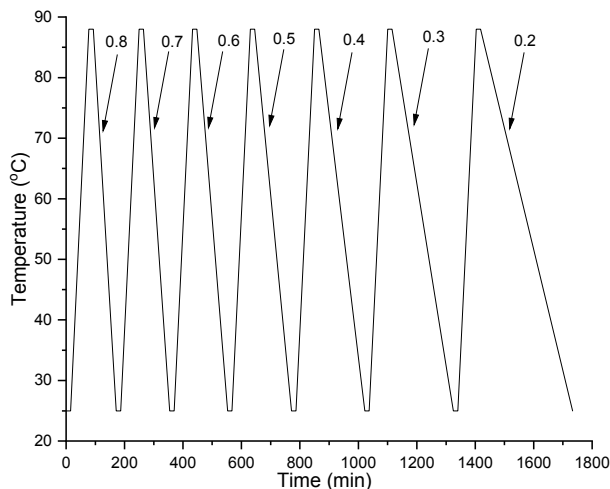


Figure 5.1. Experimental procedure used to determine the crystallization kinetics for second set of experiments, i.e., used in Paper IV. The cooling rates are given in °C/min and the heating rate was 1 °C/min.

The procedure used for the second set of experiments (Paper IV) is illustrated in Figure 5.1. Apart from 100 g solution, 20 mg silica was added to the reactor as seeds. The system was evacuated at 25 °C and was loaded with CO₂ and equilibrated for at least 15 min. It was then heated to 88 °C at a rate of 1 °C/min, equilibrated for 15 mins, before cooling to 25 °C at a cooling rate of 1 °C/min. The CO₂ loadings that led to precipitation during the cooling step and complete dissolution of the crystals during the heating step were chosen for further experiments. The cooling rates were then varied between 0.8 and 0.2 °C/min. The purpose of the heating ramp was solely to dissolve the solid crystals.

The terms $\frac{dc^S}{dT}$ and $\frac{dc_{CO_2}}{dT}$ in Equation (5.20) were obtained from the second model described in Chapter 4 and represent the slopes of the curves shown in Figures 4.5b and 4.5c. The MSW was obtained in terms of activity, $\ln S_a$, as the difference between the activity of the carbamate ions with and without precipitation in Figure 4.5a at the crystallization temperature. The crystallization temperature is approximated to the temperature at which the true heat flow reaches a maximum. To calculate $\frac{dc^S}{dT}$, $\frac{dc_{CO_2}}{dT}$ and $\ln S_a$, the amount of CO₂ captured, and the amounts of AMP and NMP used in the calorimeter were added to a flash tank, simulated using the thermodynamic property model described in Chapter 4. The dissolution temperature was defined as the point at which the crystals disappeared in the product stream of the flash tank simulation, i.e., the point of discontinuity in Figure 4.5a. The pressure used in the simulation was approximately the same as in the reactor. By obtaining these values from a validated thermodynamic model, the error-prone assumptions described in Paper III were avoided. The term $\frac{dg_{CO_2}}{dT}$ was calculated from the pressure readings of the calorimeter. The term

$\left[\ln \left(\frac{dc^s}{dT} + \frac{dc_{CO_2}}{dt} + \frac{1000}{w_{NMP}} \frac{dg_{CO_2}}{dT} \right) + \ln \left(-\frac{dT}{dt} \right) \right]$ could then be plotted against $\ln(2 \ln S_a)$ to obtain the crystallization parameters.

5.3 Results and Discussion

Based on the results discussed in Section 3.2.2 and the questions posed at the beginning of this chapter: 1) The shift in the dissolution temperature observed in Figure 3.5 and 3.6, 2) The presence of reactions other than precipitation, and 3) The release of gaseous CO₂. To begin with, the shift in the dissolution temperature must be examined in more detail.

In Figure 3.5, the solubility of the salt obtained in the test tube is compared to the solubility of CO₂ obtained in the calorimeter. All the points shown in Figure 3.5 correspond to the dissolution points for the first set of experiments (Paper III) discussed in Section 5.2. In Figure 5.2, these dissolution points are presented along with the corresponding crystallization points (points where true heat flow reaches maximum) and the points where crystals first became visible on cooling from the dissolution point. On cooling after dissolution (brown points), crystals appear first (blue points), followed by changes in the true heat flow. These observations are in agreement with other reports in the literature, where the formation of crystals was observed before property changes (Mullin, 2001b). Eventually, the maximum true heat flow appears (one green point is shown in Figure 5.2a for comparison; the other maxima in true heat flow are omitted for clarity). The chronological order of the observed changes is explained in the figure caption.

In Figure 5.2c, it can be observed that the dissolution points are separate from the points at which crystals first appear, and the latter varies depending on the cooling rate. This is in contrast to the behavior seen in Figure 5.2a, where the dissolution points are not isolated from the other points. In fact, in one case shown in Figure 5.2b, the point of visible crystal formation (blue filled triangle) appears at temperatures where previously dissolution was observed (filled and open brown squares). The observation of crystallization above dissolution temperature is a clear shift in thermodynamics and not a result of kinetics. Such behavior could be seen if a more stable form of the same compound was being formed. Previous observations, where two different crystal structures have been identified with this system (Svensson et al., 2014b), support this claim. This hypothesis of a shift in thermodynamics is further supported by the increase in dissolution temperature in the heating step that followed (filled brown triangle in Figure 5.2a), and a lack of dissolution, even at 88 °C, in the heating steps after that (data not shown). Unlike the series of experiments shown Figure 5.2a, there was no shift in the

dissolution points for the experimental series shown in Figure 5.2c. This lack of shift suggests that the crystal structure did not change during these experiments.

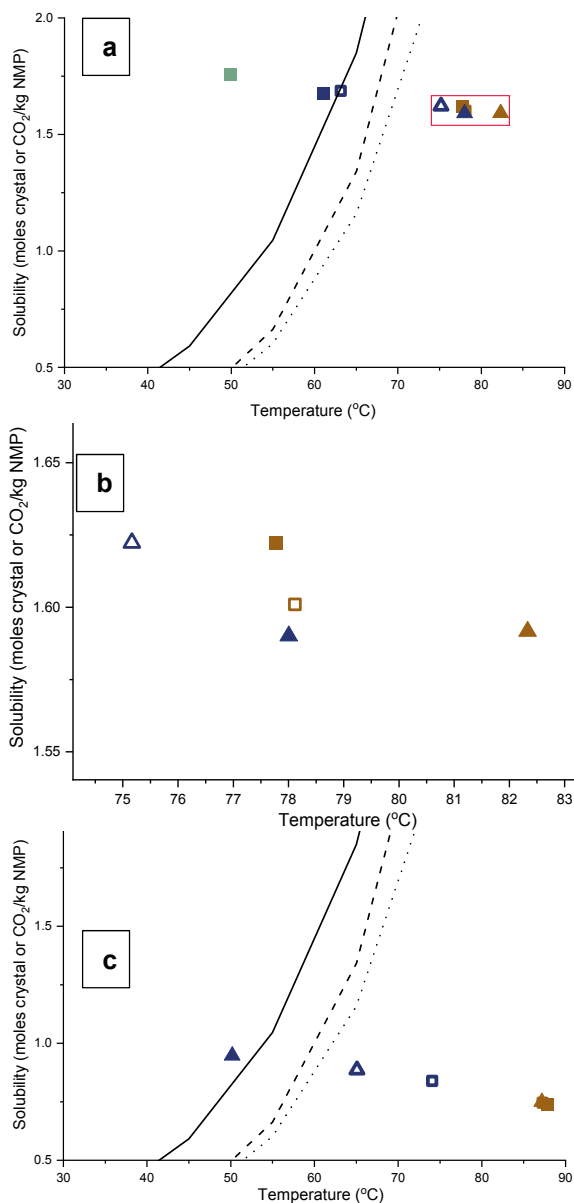


Figure 5.2. The behavior observed during an experimental series to determine the crystallization kinetics (first set of experiments described in Section 5.2, i.e., experiments from Paper III) with CO₂ loadings of a) 0.62 and c) 0.34. b) Enlargement of the points between T=74 and 84 °C in Figure 5.2a. The explanation for the symbols is as follows: brown symbols = dissolution of crystals, blue symbols = appearance of crystals, green symbol = appearance of maximum in the true heat flow. The sequence of events is as follows: ■, ■, ■, □, □, ▲, ▲, △, △.

Table 5.1. Timeline for the experiments with crystallization-dissolution steps

Period during which experiments were performed	Solution	CO ₂ loading	Dissolution temperature	Data Source
▫Before 2014	25AN	≥ 0.45*	75 °C	(Svensson, 2014)
#2015/07/28-30	25AN	0.62	78 to 82 to >88 °C	Paper III
§2015/08/05-07	25AN	0.34	87 °C	Paper III
##2016/02/03-10	2.5AT	0.54, 0.56, 0.77	between 65 and 75 °C	Paper III
**2019/02/06 to 2019/08/01	25AN	0.42-0.45	88 °C	Paper IV

*(H Svensson 2019, personal communication, 2 December)

▫Loading measured at 25 °C and experiments were performed in a different calorimeter unit (H Svensson 2020, personal communication, 8 January).

#Brown points in Figure 3.5 and all points in Figure 5.2a and b, loading measured at 50 °C.

§Blue points in Figure 3.5 and all points in Figure 5.2c, loading measured at 50 °C.

##All points in Figure 3.6 and Figure 5.4, loading measured at 25 °C.

**Points in Figure 5.5. Experiments were also performed with 15AN and with 25AN at other loadings but the crystallization and dissolution steps were not within the temperature range of the equipment (25 to 88 °C).

In Table 5.1, the sequence in which the series of experiments have been performed is given. As seen from the table, the experiments that were performed after the experimental series shown in Figure 5.2a and 5.2b show higher dissolution temperature for lower CO₂ loadings. For example, the experimental series shown in Figure 5.2c, performed after those in Figure 5.2a, has a dissolution temperature much higher in comparison (87 °C vs. 78 °C) for a loading that was much lower (0.34 vs. 0.62). The experiments performed in a different calorimeter with 25AN solution have had lower dissolution temperatures (75 °C) with a CO₂ loading above 0.45. Not all behavior in Table 5.1 could be explained at the moment. Crystals formed at a CO₂ loading of 0.34 for the case shown in Figure 5.2c (Paper III), that was not the case for the experiments performed after them (Paper IV). In the latter experiments, crystals did not form during the cooling step for any loading below 0.42.

As mentioned in Section 5.1, the MSW was calculated as the difference between the temperatures at which dissolution and the maximum in true heat flow were observed (i.e., the brown and green filled squares in Figure 5.2a). The MSW is plotted against cooling rate in Figure 5.3 for the 25AN solution at the two CO₂ loadings of 0.62 and 0.34 (Paper III). The slopes for the two CO₂ loadings are different, which suggests different crystallization kinetics. Table 5.2 shows the crystallization kinetic parameters derived using the methodology in Section 5.1.1 and the values of the exponent, p , differ for the two CO₂ loadings. This could be a result of difference in crystal structure or a drawback of the theory. To judge the applicability of the theory described in Section 5.1.1, the system complications due to the changing crystal structure must be avoided. Further experiments were thus deemed necessary in order to isolate possible effects of the theoretical methodology used.

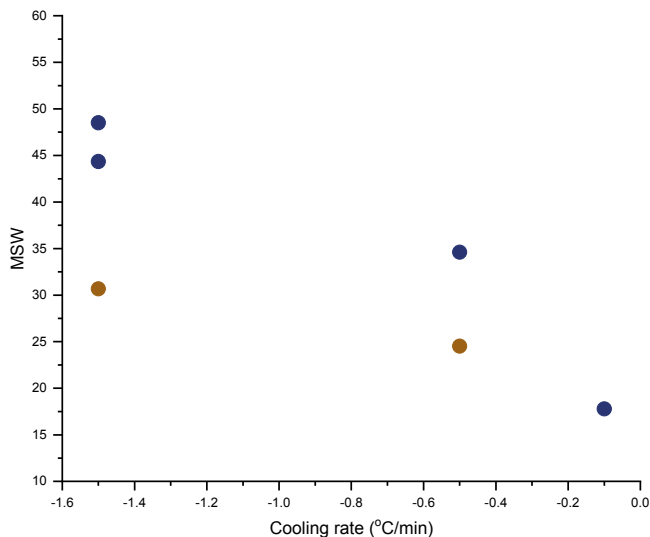


Figure 5.3. The MSW in terms of temperature plotted against the cooling rate for 25AN solutions at two different CO₂ loadings (first set of experiments described in 5.2, i.e., from Paper III). The explanation for the symbols is as follows: ● = CO₂ loading of 0.62, ● = CO₂ loading of 0.34

Table 5.2. Parameters of crystallization kinetics according to Equation (5.9) for 25AN solutions.

CO ₂ loading	ln <i>k</i>	<i>p</i>
0.62	-11.1	4.90
0.34	-6.65	2.85

The AMP-TEGDME system was tested to see if the change in crystal structure could be addressed with this system. Figure 5.4 shows the MSW in terms of temperature for the experiments performed with 2.5AT using the theory described in Section 5.1.1. Four series of experiments were performed, three of which are shown in the figure. A fourth series of experiments was also performed, with a CO₂ loading of 0.83. In this case, the first dissolution was not conclusively observed and was therefore not considered further. As seen in Figure 3.6, there was a shift in the dissolution temperature, which was always after the first dissolution point in the case of these experiments. Only one series of experiments was performed at several cooling rates (with a loading of 0.77, Figure 5.4). For this case, the first dissolution temperature was 65 °C and the dissolution temperatures for all the heating steps that followed in this experimental series was between 72 and 73 °C (see green points in Figure 3.6). This suggests that the initially formed crystal structure dissolved in the first heating step and on cooling a more stable crystal structure was formed. The dissolution temperature corresponding to this new crystal structure would be the one measured in the subsequent dissolution step. Therefore, the second dissolution temperature was used in the calculation of the MSW and, the shift in the dissolution temperature did not affect the MSW as seen in Figure 5.4. The problem of the different crystal

structures can thus be avoided using the 2.5AT solution and any crystallization kinetics calculated using this data will correspond to that of the more stable crystal structure. However, the amount of amine in these solutions might not be high enough to observe the influence of other reactions and unavoidable release of gaseous CO₂ in the system. On increasing the amount of amine in the system, precipitation or dissolution occurs outside the temperature range (25 to 88 °C) of the equipment used. Since observing the influence of CO₂ release and other reactions is key to answering RQ2, AMP-TEGDME system was not considered any further.

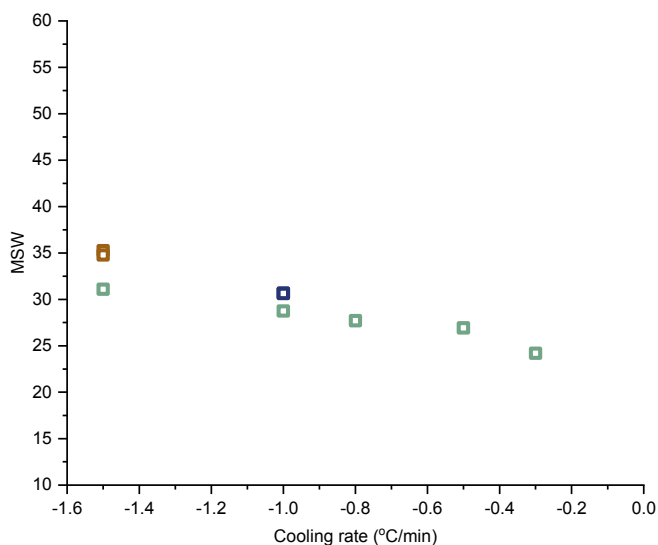


Figure 5.4. The MSW in terms of temperature plotted against the cooling rate for 2.5AT solutions at different CO₂ loadings (first set of experiments described in 5.2, i.e., from Paper III I). The explanation for the symbols is as follows: ■ = CO₂ loading of 0.54, ■ = CO₂ loading of 0.56, ■ = CO₂ loading of 0.77

Based on the above discussed results, the experiments performed to determine the crystallization kinetics (Paper IV) were designed as shown in Figure 5.1. The heating process was repeatable and consistent before the cooling steps in all the experiments. 25AN solutions were used, in which case, it is important to ensure that the crystal structure remains the same in the cooling steps. The ideal way to check the crystal structure would be to examine samples of the crystals after each cooling step. However, taking a sample from the calorimeter during the experiments might be challenging for the AMP-NMP system. As seen from Figure 3.4a, the partial pressure of CO₂ in equilibrium with 25AN solution could be above the atmospheric CO₂ partial pressure for CO₂ loadings above 0.3, when the equilibration time is 30 min. If the equilibration time is increased to >330 min, the partial pressure of CO₂ in equilibrium with the solution could be above the atmospheric CO₂ partial pressure for CO₂ loadings above 0.4. A sample taken from the calorimeter during the crystallization experiments could, therefore,

release CO₂ to the atmosphere depending on the CO₂ loading and the equilibrium time. Sampling was hence, not a suitable method for identifying a change in crystal structure in case of the AMP-NMP system. For this system, a constant dissolution temperature has been considered an indication of constant crystal structure. This is from observations based on Figure 3.5 and Figure 5.2a where, a change in crystal structure led to clear change in the dissolution temperature.

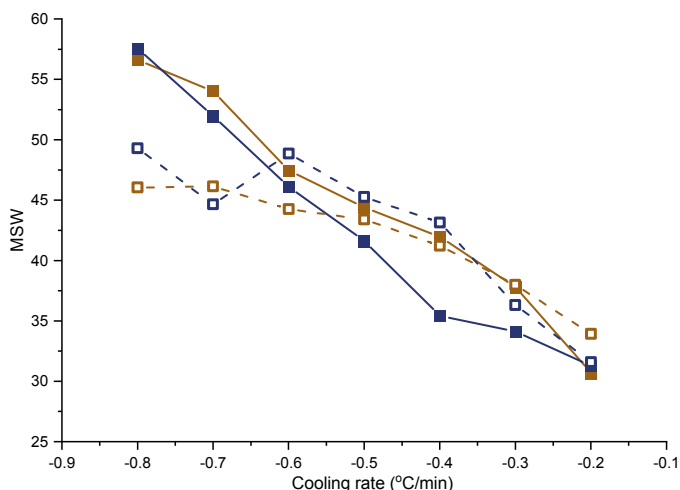


Figure 5.5. The MSW in terms of temperature plotted against the cooling rate for 25AN solutions for different CO₂ loadings (second set of experiments described in Section 5.2, i.e., from Paper IV). The explanation for the symbols is as follows: ■ = CO₂ loading of 0.425, ■ = CO₂ loading of 0.427, □ = CO₂ loading of 0.448, □ = CO₂ loading of 0.447.

Figure 5.5 shows the results of the experiments performed with 25AN to determine the crystallization kinetics (Paper IV). Dissolution was observed at a temperature between 87 and 88 °C, suggesting the crystal structure was the same. In some cases, dissolution took place during equilibration at 88 °C. The MSW and the dissolution conditions were estimated using the thermodynamic model described in Chapter 4. The model predicted a dissolution temperature of 93 °C (see Figure 4.5), which is higher than experimentally observed. Furthermore, the dissolution temperature obtained experimentally was measured at a heating rate of 1 °C/min, and a lower heating rate would probably have led to a lower dissolution temperature in the experiments. This gives an indication of the accuracy of the model, which over predicts the dissolution temperature by at least 6 °C. Despite the error, a straight line is obtained when MSW in terms of activity is plotted against the cooling rate, since the carbamate ion activity at the dissolution temperature is constant for a given CO₂ loading. However, this leads to an error in the intercept obtained from plotting $\left[\ln \left(\frac{dc^S}{dT} + \frac{dc_{CO_2}}{dt} + \frac{1000}{w_{NMP}} \frac{dg_{CO_2}}{dT} \right) + \ln \left(-\frac{dT}{dt} \right) \right]$ against $\ln(2 \ln S_a)$ in Equation (5.20).

The CO₂ loading was limited to between 0.42 and 0.45 to be suitable for the instrument's operational temperature range of 25 to 88 °C. Below 0.42, crystallization did not occur during the cooling steps in Figure 5.1, and above 0.45, dissolution did not take place in the operating temperature range. Low loadings of 0.425 and 0.427, and high loadings of 0.447 and 0.448 were investigated further. Values of the CO₂ loading are used to distinguish between these experiments. The crystallization temperature is noted from the calorimeter and the supersaturation was measured from Figure 4.5a. The pressure in the calorimeter during dissolution is ~709 kPa and gradually decreases as the system is cooled to ~304 kPa during the crystallization step. As seen from Figure 4.5a, the change in pressure does not affect the supersaturation significantly.

From Figure 5.5 it can be seen that the MSW varies with cooling rate, which is expected. More interestingly, there is a clear difference between the MSW at higher cooling rates, for different loadings. This means that the MSW is also affected by the CO₂ loading of the system, behavior that is not explained by Figure 2.7a. This behavior can be explained with the help of Figure 2.7b. Precipitation occurs in the region where the solid-liquid equilibrium line is below the gas-liquid line. Since all reactions except precipitation are in equilibrium, the solution would lie between these two lines. In this region, a supersaturated solution with higher loading will be closer to the gas-liquid equilibrium line than the solution with lower loading, at the same temperature. On the one hand, supersaturation pushes the solution towards precipitation, while on the other, the solution's capability to hold dissolved CO₂ and ions until the gas-liquid equilibrium is reached, keeps it from precipitating. This resistance to precipitation can be overcome more easily under one or more of the following three conditions: when the cooling rate is high, when the loading is increased, or when the amine concentration in the solution is higher. The amine concentration is the same and the loading does not differ significantly in the experiments shown in Figure 5.5. However, for the experiments with higher loading at high cooling rates, a clear difference in the MSW is observed.

Similar behavior has also been reported for the K₂CO₃-based system (Wu et al., 2017a), where lower loading and a higher cooling rate led to a broader MSW than higher loading at the same cooling rate. However, in the K₂CO₃-based system, lower loading and a lower cooling rate led to a narrower MSW than higher loading at the same cooling rate, while the AMP-NMP system showed almost the same MSW at lower cooling rates (for both lower and higher loadings). The observed difference in the two systems could be due to the difference in the interactions of the cation in the salt. In the AMP-NMP system, both the cation and anion are interdependent. An increase in the number of ions leads to a decrease in the amount of free amine, which is held together only by weak forces. Furthermore, the solvent has the ability to hold ions, preventing precipitation. In the case of KHCO₃, resistance to precipitation is a result of the equilibrium

between KHCO_3 and K_2CO_3 , as the cation K^+ tries to precipitate in the KHCO_3 system, and the interactions are ionic in nature. These ionic interactions are much stronger than the amine-ion or ion-solvent interactions in the AMP-NMP system. Since one of the three conditions to overcome resistance to precipitation is the amine concentration in the solution, this explains why precipitation from the 15AN solution took much longer than from 25AN solution (see Section 4.2).

The parameters for crystallization kinetics from Equation (5.15) are given in Table 5.3. The kinetics of crystallization in the AMP-NMP- CO_2 system were indeed slow, as can be seen from the long equilibrium times and the metastable zone widths in Figure 5.5. In terms of plant design, this means that a very large crystallizer would be needed. Based on the results presented in Figure 3.3 and Section 3.2.1, precipitation is likely to take place in the absorption column, which means that the part of the absorber column where precipitation takes place will be large.

Table 5.3. Crystallization kinetic parameters obtained in 25AN solutions using the methodology presented in Section 5.1.2.

Loading	p'	$\ln k'$
0.425	1.33	-6.09
0.427	1.12	-5.75
0.448	2.91	-7.51
0.447	2.28	-6.86

Several observations support the claim that the traditional power law relation is not sufficient to model crystallization kinetics for the AMP-NMP system, thus, answering RQ2.1. In Section 5.1.1, the traditional power law relation has been derived for the case presented in Figure 2.7a. If the behavior deviates strongly from that shown in Figure 2.7a, it can be understood from the derivation in Section 5.1.1 that the power law relation will change. In Figure 4.5a, the behavior of the AMP-NMP system is presented which is indeed, different from that in Figure 2.7a. The difference between the black and the gray curves in Figure 4.5a gives a measure of the MSW for AMP-NMP system, answering RQ2.3. The relation between MSW in terms of concentration and temperature shown in Equation (5.10) would not be valid for this system as mentioned in Section 5.1.1.

CO_2 release has been unavoidable in both AMP-NMP and -TEGDME, as discussed in Section 3.2.2. The change in the definition of supersaturation and CO_2 released are taken into account in Equation (5.20). In addition, Equation (5.20) also includes a term accounting for the physically dissolved CO_2 . The various temperature derivatives required according to Equation (5.20) are presented in Table 5.4 for a CO_2 loading of 0.425. It can be seen from the table that the temperature derivative of dissolved CO_2 increases with decreasing cooling rate. This increase is much greater than the decrease in the corresponding temperature derivative of carbamate ion concentration. The contributions from

the various terms presented in Table 5.4 are in the same order of magnitude (Note that the gaseous CO₂ term must be multiplied by a factor of 1000/*w*_{NMP}). There is a clear increase in the total mass balance term with decreasing cooling rate. This suggests that the amount of salt precipitating increases at lower cooling rates. On comparing the contribution of the carbamate ion to total mole balance, it can be seen that the carbamate ion is only 6 to 25% of the precipitation. Even if the released CO₂ could be avoided, the increase in dissolved CO₂ is also significant (13 to 50% of the total precipitation). RQ2.2 has hence been answered and in order to use the traditional power law as expressed in Equation (5.13), it is not sufficient to avoid CO₂ release from the AMP-NMP system. It is necessary to show that changes in all the other terms except those related to the ions forming the salt, are negligible.

Table 5.4. Changes in the various terms of the CO₂ mole balance in Equation (5.19) with the CO₂ loading of 0.425 in a 25AN solution (Paper IV).

$-\frac{dT}{dt}$	$-\Delta T$	$\frac{dc^s}{dT}$	$\frac{dc_{CO_2}}{dT}$	$\frac{dg_{CO_2}}{dT}$	$\left(\frac{dc^s}{dT} + \frac{dc_{CO_2}}{dT} + \frac{1000}{w_{NMP}} \frac{dg_{CO_2}}{dT}\right)$
0.8	56.6	0.00427	0.00225	0.00078	0.0168
0.7	54.0	0.00455	0.00277	0.00075	0.0173
0.6	47.5	0.00483	0.00479	0.00078	0.0200
0.5	44.4	0.00460	0.00627	0.00081	0.0216
0.4	42.0	0.00427	0.00735	0.00084	0.0228
0.3	37.8	0.00356	0.00908	0.00086	0.0240
0.2	30.7	0.00157	0.01288	0.00088	0.0260
SD(%)		26.3%	53.1%	5.3%	15%

$\frac{dg_{CO_2}}{dT}$ were obtained from the experimental data.

$\frac{dc^s}{dT}$ and $\frac{dc_{CO_2}}{dT}$ were obtained from the thermodynamic model, Chapter 4.

$-\Delta T$ is calculated as a difference of the crystallization temperature (obtained from the experimental data) and dissolution temperature (obtained from the thermodynamic model, Chapter 4).

The extent to which the model developed can be applied to future systems, more specifically, AMP in other solvents, has been discussed in Chapter 4 (RQ2.4).

The values of the terms $\frac{dc^s}{dT}$, $\frac{dc_{CO_2}}{dT}$, and $\ln S_a$ in Equation (5.20) were all obtained from the model. In order to extend the crystallization kinetics to other solvents, experiments would be required to determine the crystallization temperature and the value of the term $\frac{dg_{CO_2}}{dT}$. The amount of research efforts required for future systems employing AMP as the amine could be decreased by applying the thermodynamic model presented in Chapter 4.

Although the theory presented in Section 5.1.2 was developed for the AMP-NMP system with gas-liquid-solid equilibrium (i.e., unavoidable CO₂ release), it is also valid for other CCS systems with and without CO₂ release (RQ2.5). For example, extending the theory to the K₂CO₃ system suggests that the water equilibrium in Reactions {14} and {15} plays a role in the production of the anion. A balance for water would have to be considered, especially for concentrated K₂CO₃

solutions. Similar deductions can be made about other precipitating carbon capture systems.



The semi-empirical power law relation combines several physically significant terms into a rate constant, k or k' , and order of crystallization, p or p' . That is, the parameters given in Table 5.3 and Table 5.2 have little physical significance, although their values can be compared, to determine whether a particular system is slower or faster than another. Moreover, the crystallization kinetics are expressed here in terms of molality/min, while the kinetics of crystallization will depend on the number of crystals. Applying the theory in terms of molality/min is equivalent to assuming that the number of crystals formed is constant.

6 Conclusions

Two main research questions were posed in this thesis with the aim of accelerating research in the fields of non-aqueous and precipitating systems. The first concerned the modelling of non-aqueous systems (precipitating or non-precipitating) and the second the estimation of the crystallization kinetics in precipitating CCS systems (aqueous or non-aqueous). AMP in NMP, which is both non-aqueous and precipitating, was used as a case study for the application of the methodologies developed. Experimental data were obtained to help answer these two questions. Some useful conclusions have been drawn based on the experimental data on the solubility of CO₂ in AMP-NMP solutions.

- A solution of 25wt% AMP in NMP is useful as a non-aqueous precipitating system while a 15wt% AMP in NMP solution could be used as a non-aqueous non-precipitating system if the inlet stream is cooled to 25 °C.
- Very low lean loadings can be achieved without any stripping agent in the AMP-NMP system at atmospheric pressure.
- A cyclic capacity comparable to that of the benchmark aqueous MEA system is possible in 25wt% AMP in NMP solutions.
- The solubility of CO₂ in the AMP-NMP solutions will be higher during intermittent operation of a plant with a 25wt% AMP in NMP solution (precipitating system) than during normal operation. If a plant were designed to operate with 15wt% AMP in NMP solution as a non-aqueous non-precipitating system, precipitation can be expected during unexpected shutdown.

Using the experiments performed to determine CO₂ solubility in the AMP-NMP solutions, research question 1 was answered.

How can non-aqueous systems be modelled?

Infinite dilution in water was chosen as the reference state for ions in non-aqueous system of AMP-NMP, and the electrolyte NRTL-based property method was used in the model. This methodology was shown to satisfactorily model non-aqueous electrolytic systems with a few exceptions observed for the AMP-NMP case study. Disagreement was observed between the model and experimental data

at CO₂ loadings close to those causing precipitation. Either the model was unable to predict the point of precipitation accurately or the experimental results do not represent true equilibrium points. The model also overpredicted the dissolution temperature, which was later used to obtain the crystallization kinetics.

In an attempt to answer research question 2, solubility of salt was measured in a test tube. This experimental method was however, deemed unsuitable due to the unavoidable release of CO₂ during dissolution. Nevertheless, some useful conclusions could be drawn from these measurements.

- Such experimental results could not be used in the determination of crystallization kinetics due to the error resulting from the pressure difference in the two experimental setups compared (the test tube, in which the solubility was measured, and the calorimeter, in which the crystallization kinetics were measured).
- There were at least two different crystal structures, based on the shift in the observed dissolution temperature of the crystals.

The experiments performed to determine the crystallization kinetics were complicated by the experimental procedure and the different crystal structures, which had to be addressed before attempting to evaluate the methodology used for determining crystallization kinetics. The problem of different crystal structures was addressed by ensuring that the dissolution temperature was the same throughout experimental series performed to obtain the crystallization kinetics. By using the model to predict the concentrations at saturation conditions, the complications due to the experimental procedure were avoided. The second research question could thus be answered.

How can crystallization kinetics for gas-liquid-solid systems be estimated?

A methodology has been developed involving the use of the power law to determine the crystallization kinetics for gas-liquid-solid systems. The thermodynamic model was used to complement the experiments performed to determine crystallization kinetics. Sources of error in the traditional power law were identified, and it was shown that avoiding CO₂ release during the experiments is not sufficient when using the traditional power law to obtain crystallization kinetics in carbon capture applications. It is necessary to ensure that all temperature derivatives of all components except the ions forming salt are negligible in order to use the traditional power law relation. One of the main conclusions from this study was that the width of the meta-stable zone is dependent on the CO₂ loading of the system. The method of obtaining the crystallization kinetics developed for AMP-NMP could be extended to other AMP-based non-aqueous precipitating systems using the thermodynamic model. Since the thermodynamic model has been used to estimate the carbamate ion and dissolved CO₂, an adapted version could be used for the prediction of the same

terms in other solvents. Furthermore, the methodology can be extended to other precipitating CCS systems (aqueous or non-aqueous).

7 Future work

A methodology to thermodynamically model a non-aqueous system has been developed in the thesis. It has been observed that the experimental data used to obtain the model parameters might not correspond to true equilibrium. Experiments performed with AMP in a different solvent might be more fitting to model the equilibrium constants. TEGDME might be a more suitable solvent for this purpose. These equilibrium constants could then be extended for other solvents as long as the reaction mechanism is the same. Similarly, the thermodynamic behavior of the two crystal structures could be studied in TEGDME and extended to AMP-NMP. The temperature range of the equipment can be extended by using a different medium, rather than or in addition to, using the current water bath. This would help in determining how the MSW changes with a wider range of CO₂ loading and amine concentration. Speciation using NMR to ensure the reaction mechanism are recommended. In addition, tolerance to water is necessary for any non-aqueous system and such tests must be performed before scaling the process.

Validating the thermodynamic model developed in unsymmetric reference state with the same model developed in symmetric reference state and comparing results would increase confidence in the model. In view of crystallization kinetics, developing a methodology for gas-liquid-solid systems using a more physically significant classical theory can be valuable. It is also important to check if the theory developed holds up at other loadings and amine concentrations in AMP-NMP solution. Application of the developed theory to other precipitating systems like K₂CO₃ or amino acid-based systems might be useful in understanding the full potential of the theory.

References

- Aronu, U.E., Gondal, S., Hessen, E.T., Haug-Warberg, T., Hartono, A., Hoff, K.A., Svendsen, H.F., 2011. Solubility of CO₂ in 15, 30, 45 and 60 mass% MEA from 40 to 120 °C and model representation using the extended UNIQUAC framework. *Chem. Eng. Sci.* 66, 6393–6406. <https://doi.org/10.1016/J.CES.2011.08.042>
- Aronu, U.E., Hjarbo, K., Chikukwa, A., Kim, I., Tobiesen, A., Mejdell, T., 2018. Learnings from pilot plant test of a precipitating process for CO₂ scrubbing from flue gas, in: 14th International Conference on Greenhouse Gas Control Technologies. Melbourne, Australia.
- Aronu, U.E., Ma, X., 2017. Liquid-solid Solubility in AMP-KSAR-CO₂-H₂O System. *Energy Procedia* 114, 693–706. <https://doi.org/10.1016/j.egypro.2017.03.1212>
- Aspentech, 2017. Aspen Physical Property System – Physical Property Models v10.
- AVOID2, 2019. The INDCs and climate impacts [WWW Document]. URL <https://www.avoid.uk.net/> (accessed 12.10.19).
- Barrett, P., Glennon, B., 2002. Characterizing the metastable zone width and solubility curve using Lasentec FBRM and PVM. *Trans IChemE* 80, 799–805.
- Barzagli, F., Di Vaira, M., Mani, F., Peruzzini, M., 2012. Improved solvent formulations for efficient CO₂ absorption and low-temperature desorption. *ChemSusChem* 5, 1724–1731. <https://doi.org/10.1002/cssc.201200062>
- Barzagli, F., Lai, S., Mani, F., Stoppioni, P., 2014. Novel non-aqueous amine solvents for biogas upgrading. *Energy and Fuels* 28, 5252–5258. <https://doi.org/10.1021/ef501170d>
- Blomen, E., Hendriks, C., Neele, F., 2009. Capture technologies: Improvements and promising developments. *Energy Procedia* 1, 1505–1512. <https://doi.org/10.1016/j.egypro.2009.01.197>
- Budzianowski, W.M., 2017a. Assessment of Thermodynamic Efficiency of Carbon Dioxide Separation in Capture Plants by Using Gas-Liquid Absorption, in: Budzianowski, W.M. (Ed.), *Energy Efficient Solvents for CO₂ Capture by Gas-Liquid Absorption: Compounds, Blends and Advanced Solvent Systems*. Springer International Publishing, Cham, pp. 13–26. https://doi.org/10.1007/978-3-319-47262-1_2
- Budzianowski, W.M., 2017b. Useful Mechanisms, Energy Efficiency Benefits, and Challenges of Emerging Innovative Advanced Solvent Based Capture Processes, in: Budzianowski, W.M. (Ed.), *Energy Efficient Solvents for CO₂ Capture by Gas-Liquid Absorption: Compounds, Blends and Advanced Solvent Systems*. Springer International Publishing, Cham, pp. 69–98. https://doi.org/10.1007/978-3-319-47262-1_4

- Calle, R.G., 2018. Modelling of an Amine-Organic Solvent based Carbon-Capture Process for Efficient Excess Heat Utilization. Chalmers University of Technology.
- Carbon countdown clock: how much of the world's carbon budget have we spent? [WWW Document], 2017. . The Guardian URL <https://www.theguardian.com/environment/datablog/2017/jan/19/carbon-countdown-clock-how-much-of-the-worlds-carbon-budget-have-we-spent> (accessed 10.7.19).
- Chen, C.-C., Britt, H.I., Boston, J.F., Evans, L.B., 1982. Local composition model for excess Gibbs energy of electrolyte systems. Part I: Single solvent, single completely dissociated electrolyte systems. *AIChE J.* 28, 588–596. <https://doi.org/10.1002/aic.690280410>
- Clack, C.T.M., Qvist, S.A., Apt, J., Bazilian, M., Brandt, A.R., Caldeira, K., Davis, S.J., Diakov, V., Handschy, M.A., Hines, P.D.H., Jaramillo, P., Kammen, D.M., Long, J.C.S., Morgan, M.G., Reed, A., Sivaram, V., Sweeney, J., Tynan, G.R., Victor, D.G., Weyant, J.P., Whitacre, J.F., 2017. Evaluation of a proposal for reliable low-cost grid power with 100% wind, water, and solar. *Proc. Natl. Acad. Sci.* 114, 6722 LP – 6727. <https://doi.org/10.1073/pnas.1610381114>
- Climeworks, 2019. CO2 removal [WWW Document]. URL <https://www.climeworks.com/co2-removal/>
- European Commission, 2015a. Paris Agreement [WWW Document]. URL https://ec.europa.eu/clima/policies/international/negotiations/paris_en (accessed 10.7.19).
- European Commission, 2015b. Final Report Summary - ICAP (Innovative CO2 capture) [WWW Document]. URL <https://cordis.europa.eu/project/rcn/93169/reporting/en> (accessed 11.22.19).
- Consoli, C.P., Wildgust, N., 2017. Current Status of Global Storage Resources. *Energy Procedia* 114, 4623–4628. <https://doi.org/10.1016/J.EGYPRO.2017.03.1866>
- Cousins, A., Feron, P.H., Hayward, J., Jiang, K., Zhai, R., Puxty, G., Garcia, M., 2019. Review of current and emerging CO2 capture technologies, in: 10th Trondheim CCS Conference. Trondheim.
- Carbon Tracker Initiative, 2017. Unburnable Carbon 2013: Wasted Capital and Stranded Assets [WWW Document]. URL <https://www.carbontracker.org/tools-and-insights/unburnable-carbon-2013-wasted-capital-and-stranded-assets-cti-report/> (accessed 10.7.19).
- Firaha, D.S., Kirchner, B., 2016. Tuning the Carbon Dioxide Absorption in Amino Acid Ionic Liquids. *ChemSusChem* 9, 1591–1599. <https://doi.org/10.1002/cssc.201600126>
- George, J., Sastry, N. V., 2004. Densities, Viscosities, Speeds of Sound, and Relative Permittivities for Water + Cyclic Amides (2-Pyrrolidinone, 1-Methyl-2-pyrrolidinone, and 1-Vinyl-2-pyrrolidinone) at Different Temperatures. *J. Chem. Eng. Data* 49, 235–242. <https://doi.org/10.1021/jc0340809>
- Heard, B.P., Brook, B.W., Wigley, T.M.L., Bradshaw, C.J.A., 2017. Burden of proof: A comprehensive review of the feasibility of 100% renewable-electricity systems. *Renew. Sustain. Energy Rev.* 76, 1122–1133.

- <https://doi.org/10.1016/J.RSER.2017.03.114>
- Heldebrant, D.J., Koech, P.K., Glezakou, V.-A., Rousseau, R., Malhotra, D., Cantu, D.C., 2017a. Water-Lean Solvents for Post-Combustion CO₂ Capture: Fundamentals, Uncertainties, Opportunities, and Outlook. *Chem. Rev.* 117, 9594–9624. <https://doi.org/10.1021/acs.chemrev.6b00768>
- Heldebrant, D.J., Koech, P.K., Rousseau, R., Glezakou, V.-A., Cantu, D., Malhotra, D., Zheng, F., Whyatt, G., Freeman, C.J., Bearden, M.D., 2017b. Are Water-lean Solvent Systems Viable for Post-Combustion CO₂ Capture? *Energy Procedia* 114, 756–763. <https://doi.org/10.1016/J.EGYPRO.2017.03.1218>
- Hsieh, C.-J., Chen, J.-M., Li, M.-H., 2007. Dielectric constants of aqueous diisopropanolamine, diethanolamine, N-methyldiethanolamine, triethanolamine, and 2-amino-2-methyl-1-propanol solutions. *J. Chem. Eng. Data* 52, 619–623. <https://doi.org/10.1021/je600515j>
- HYBRIT, n.d. HYBRIT-Towards fossil-free steel [WWW Document]. URL <http://www.hybritdevelopment.com/hybrit-toward-fossil-free-steel> (accessed 10.7.19).
- IEA, 2019a. CO₂ Emissions from Fuel Combustion 2019 Edition.
- IEA, 2019b. World Energy Outlook-Data and statistics [WWW Document]. URL <https://www.iea.org/data-and-statistics> (accessed 10.7.19).
- IEA, 2013. Global Action to Advance Carbon Capture and Storage.
- IEAGHG, 2013a. Deployment of CCS in the Cement Industry.
- IEAGHG, 2013b. Iron and Steel CCS Study: Techno-Economics Integrated Steel Mill, Report 2013/04.
- IPCC, 2018a. Chapter 3. Impacts of 1.5°C of Global Warming on Natural and Human Systems.
- IPCC, 2018b. Chapter 2. Mitigation Pathways Compatible with 1.5°C in the Context of Sustainable Development.
- IPCC, 2018c. Chapter 4. Strengthening and Implementing the Global Response.
- IPCC, 2013. Climate change 2013: The physical science basis.
- Jakob, M., Hilaire, J., 2015. Unburnable fossil-fuel reserves. *Nature* 517, 150.
- Joback, K.G., Reid, R.C., 1987. Estimation of Pure-Component Properties from Group-Contributions. *Chem. Eng. Commun.* 57, 233–243.
- Jou, F.-Y., Mather, A.E., Otto, F.D., 1995. The solubility of CO₂ in a 30 mass percent monoethanolamine solution. *Can. J. Chem. Eng.* 73, 140–147. <https://doi.org/10.1002/cjce.5450730116>
- Karlsson, H., 2018. Physical properties of the 2-amino-2-methyl-1-propanol and N-methyl-2-pyrrolidone system. SSRN.
- Karlsson, H., Svensson, H., 2017. Regeneration of Non-Aqueous Precipitating Amine Solvents, in: 4th Post Combustion Capture Conference (PCCC4).
- Karlsson, H.K., Svensson, H., 2017. Rate of absorption for CO₂ absorption systems using a wetted wall column. *Energy Procedia* 114, 2009–2023.
- Kumar, S., Cho, J.H., Moon, I., 2014. Ionic liquid-amine blends and CO₂BOLs:

- Prospective solvents for natural gas sweetening and CO₂ capture technology—A review. *Int. J. Greenh. Gas Control* 20, 87–116.
<https://doi.org/10.1016/J.IJGGC.2013.10.019>
- Lail, M., Tanthana, J., Coleman, L., 2014. Non-Aqueous Solvent (NAS) CO₂ Capture Process. *Energy Procedia* 63, 580–594.
<https://doi.org/10.1016/J.EGYPRO.2014.11.063>
- Li, J., Chen, L., Ye, Y., Qi, Z., 2014. Solubility of CO₂ in the Mixed Solvent System of Alkanolamines and Poly(ethylene glycol) 200. *J. Chem. Eng. Data* 59, 1781–1787.
<https://doi.org/10.1021/je400947t>
- Liang, Z.H., Sanpasertparnich, T., Tontiwachwuthikul, P.P.T., Gelowitz, D., Idem, R., 2011. Part 1: Design, modeling and simulation of post-combustion CO₂ capture systems using reactive solvents. *Carbon Manag.* 2, 265–288.
<https://doi.org/10.4155/cmt.11.19>
- Lin, Y.-J.J., Rochelle, G.T., 2016. Approaching a reversible stripping process for CO₂ capture. *Chem. Eng. J.* 283, 1033–1043. <https://doi.org/10.1016/j.cej.2015.08.086>
- Ma'mun, S., 2014. Solubility of carbon dioxide in aqueous solution of potassium sarcosine from 353 to 393K. *Energy Procedia* 51, 191–196.
<https://doi.org/10.1016/j.egypro.2014.07.022>
- Ma'mun, S., Nilsen, R., Svendsen, H.F., Juliusen, O., 2005. Solubility of Carbon Dioxide in 30 mass % Monoethanolamine and 50 mass % Methyl-diethanolamine Solutions. *J. Chem. Eng. Data* 50, 630–634. <https://doi.org/10.1021/je0496490>
- Ma, X., 2014. Precipitation in Carbon Dioxide Capture Processes. Norwegian University of Science and Technology.
- Majchrowicz, M.E., Brilman, D.W.F. (Wim), Groeneveld, M.J., 2009. Precipitation regime for selected amino acid salts for CO₂ capture from flue gases. *Energy Procedia* 1, 979–984. <https://doi.org/10.1016/j.egypro.2009.01.130>
- Mobley, P.D., Rayer, A. V, Tanthana, J., Gohndrone, T.R., Soukri, M., Coleman, L.J.I., Lail, M., 2017. CO₂ Capture Using Fluorinated Hydrophobic Solvents. *Ind. Eng. Chem. Res.* 56, 11958–11966. <https://doi.org/10.1021/acs.iecr.7b03088>
- Mota-Martinez, M.T., Hallett, J., MacDowell, N., 2017. Screening Solvents Properties for CO₂ Capture Based on the Process Performance. *Energy Procedia* 114, 1551–1557. <https://doi.org/10.1016/j.egypro.2017.03.1285>
- Mullin, J.W., 2001a. 5 – Nucleation, in: *Crystallization*. pp. 181–215.
<https://doi.org/10.1016/B978-075064833-2/50007-3>
- Mullin, J.W., 2001b. *Crystallization*, fourth. ed. Butterworth-Heinemann.
- Newton-Cross, G. (Energy technologies institute), Gammer, D. (Energy technologies institute), 2016. The evidence for deploying bioenergy with CCS (BECCS) in the UK [WWW Document]. URL <https://www.eti.co.uk/insights/the-evidence-for-deploying-bioenergy-with-ccs-beccs-in-the-uk> (accessed 10.8.19).
- Nývlt, J., 1983. Induction period of nucleation and metastable zone width. *Collect. Czechoslov. Chem. Commun.* 48, 1977–1983.
- Pakzad, P., Mofarahi, M., Izadpanah, A.A., Afkhamipour, M., Lee, C.-H., 2018. An experimental and modeling study of CO₂ solubility in a 2-amino-2-methyl-1-

- propanol (AMP) + N-methyl-2-pyrrolidone (NMP) solution. *Chem. Eng. Sci.* 175, 365–376. <https://doi.org/10.1016/J.CES.2017.10.015>
- Pearson, P., Cousins, A., 2016. 18 - Assessment of corrosion in amine-based post-combustion capture of carbon dioxide systems, in: Feron (Ed.), *Absorption Based Post Combustion Capture of Carbon Dioxide*. Woodhead Publishing, pp. 439–463. <https://doi.org/https://doi.org/10.1016/B978-0-08-100514-9.00018-4>
- Perry, R.J., Grocela-Rocha, T.A., O'Brien, M.J., Genovese, S., Wood, B.R., Lewis, L.N., Lam, H., Soloveichik, G., Rubinsztajn, M., Kniajanski, S., Draper, S., Enick, R.M., Johnson, J.K., Xie, H., Tapriyal, D., 2010. Aminosilicone solvents for CO₂ capture. *ChemSusChem* 3, 919–930. <https://doi.org/10.1002/cssc.201000077>
- Puxty, G., Maeder, M., 2016. 2 - The fundamentals of post-combustion capture, in: Feron (Ed.), *Absorption Based Post Combustion Capture of Carbon Dioxide*. Woodhead Publishing, pp. 13–33. <https://doi.org/https://doi.org/10.1016/B978-0-08-100514-9.00002-0>
- Qader, A., Webley, P.A., Stevens, G.W., Hooper, B., Harkin, T., Wiley, D.E., Kentish, S.E., Scholes, C.A., Smith, K., Mumford, K., Chen, V., 2017. Learnings from CO₂CRC Capture Pilot Plant Testing - Assessing Technology Development. *Energy Procedia* 114, 5855–5868. <https://doi.org/10.1016/j.egypro.2017.03.1723>
- Renon, H., Prausnitz, J.M., 1968. Local compositions in thermodynamic excess functions for liquid mixtures. *AIChE J.* 14, 135–144. <https://doi.org/10.1002/aic.690140124>
- Riebeek, H. (NASA), 2011. The Carbon Cycle [WWW Document]. URL <https://www.earthobservatory.nasa.gov/features/CarbonCycle> (accessed 10.7.19).
- Rochelle, G.T., 2016. 3 - Conventional amine scrubbing for CO₂ capture, in: Feron (Ed.), *Absorption Based Post Combustion Capture of Carbon Dioxide*. Woodhead Publishing, pp. 35–67. <https://doi.org/https://doi.org/10.1016/B978-0-08-100514-9.00003-2>
- Sanchez-Fernandez, E., Heffernan, K., Van Der Ham, L., Linders, M.J.G., Goetheer, E.L.V., Vlucht, T.J.H., 2014. Precipitating amino acid solvents for CO₂ capture. Opportunities to reduce costs in Post combustion capture. *Energy Procedia* 63, 727–738. <https://doi.org/10.1016/j.egypro.2014.11.080>
- Sangwal, K., 2018. Nonisothermal Crystallization Kinetics and the Metastable Zone Width, in: *Nucleation and Crystal Growth*, Wiley Online Books. pp. 189–265. <https://doi.org/doi:10.1002/9781119461616.ch5>
- Shen, K.P., Li, M.H., 1992. Solubility of carbon dioxide in aqueous mixtures of monoethanolamine with methyldiethanolamine. *J. Chem. Eng. Data* 37, 96–100. <https://doi.org/10.1021/je00005a025>
- Sherman, B.J., 2016. Thermodynamic and Mass Transfer Modeling of Aqueous Hindered Amines for Carbon Dioxide Capture. University of Texas.
- Sherman, B.J., Rochelle, G.T., 2017. Thermodynamic and Mass-Transfer Modeling of Carbon Dioxide Absorption into Aqueous 2-Amino-2-Methyl-1-Propanol. *Ind. Eng. Chem. Res.* 56, 319–330. <https://doi.org/10.1021/acs.iecr.6b03009>
- Simoni, L.D., Lin, Y., Brennecke, J.F., Stadtherr, M.A., 2008. Modeling Liquid–Liquid Equilibrium of Ionic Liquid Systems with NRTL, Electrolyte-NRTL, and UNIQUAC. *Ind. Eng. Chem. Res.* 47, 256–272. <https://doi.org/10.1021/ie070956j>

- Solidia, n.d. Solutions [WWW Document]. URL <https://www.solidiatech.com/solutions.html> (accessed 12.11.19).
- Song, Y., Chen, C.-C., 2009. Symmetric Electrolyte Nonrandom Two-Liquid Activity Coefficient Model. *Ind. Eng. Chem. Res.* 48, 7788–7797. <https://doi.org/10.1021/ie9004578>
- Sutter, D., Gazzani, M., Mazzotti, M., 2015. Formation of solids in ammonia-based CO₂ capture processes — Identification of criticalities through thermodynamic analysis of the CO₂–NH₃–H₂O system. *Chem. Eng. Sci.* 133, 170–180. <https://doi.org/10.1016/j.ces.2014.12.064>
- Sutter, D., Gazzani, M., Mazzotti, M., 2014. Kinetics of Solid Formation in the Chilled Ammonia System and Implications for a 2nd Generation Process. *Energy Procedia* 63, 1957–1962. <https://doi.org/10.1016/j.egypro.2014.11.207>
- Svendsen, H.F., Hessen, E.T., Mejdell, T., 2011. Carbon dioxide capture by absorption, challenges and possibilities. *Chem. Eng. J.* 171, 718–724. <https://doi.org/https://doi.org/10.1016/j.ces.2011.01.014>
- Svensson, H., 2014. Energy efficient processes for the production of gaseous biofuels - Reforming and Gas upgrading. Lund University.
- Svensson, H., Edfeldt, J., Zejnullahu Velasco, V., Hulteberg, C., Karlsson, H.T., 2014a. Solubility of carbon dioxide in mixtures of 2-amino-2-methyl-1-propanol and organic solvents. *Int. J. Greenh. Gas Control* 27, 247–254. <https://doi.org/10.1016/j.ijggc.2014.06.004>
- Svensson, H., Hulteberg, C., Karlsson, H.T., 2014b. Precipitation of AMP Carbamate in CO₂ Absorption Process. *Energy Procedia* 63, 750–757. <https://doi.org/10.1016/j.egypro.2014.11.083>
- Svensson, H., Karlsson, H.K., 2018. Solubility of carbon dioxide in mixtures of 2-amino-2-methyl-1-propanol and N-methyl-2-pyrrolidone at absorption and desorption conditions, in: 14th International Conference on Greenhouse Gas Control Technologies.
- Svensson, H., Zejnullahu Velasco, V., Hulteberg, C., Karlsson, H.T., 2014c. Heat of absorption of carbon dioxide in mixtures of 2-amino-2-methyl-1-propanol and organic solvents. *Int. J. Greenh. Gas Control* 30, 1–8. <https://doi.org/10.1016/j.ijggc.2014.08.022>
- Temple, J., 2018. Relying on renewables alone significantly inflates the cost of overhauling energy [WWW Document]. *MIT Technol. Rev.* URL <https://www.technologyreview.com/s/610366/relying-on-renewables-alone-would-significantly-raise-the-cost-of-overhauling-the-energy/> (accessed 10.8.19).
- Thomsen, K., 1997. Aqueous electrolytes: model parameters and process simulation. Technical University of Denmark.
- Tong, D., Trusler, J.P.M., Maitland, G.C., Gibbins, J., Fennell, P.S., 2012. Solubility of carbon dioxide in aqueous solution of monoethanolamine or 2-amino-2-methyl-1-propanol: Experimental measurements and modelling. *Int. J. Greenh. Gas Control* 6, 37–47. <https://doi.org/10.1016/J.IJGGC.2011.11.005>
- United Nations Framework Convention on Climate Change, 2015. Summary of the Paris Agreement [WWW Document]. URL

- <https://unfccc.int/resource/bigpicture/#content-the-paris-agreemen> (accessed 10.7.19).
- Van Wagener, D.H., Rochelle, G.T., 2011. Stripper configurations for CO₂ capture by aqueous monoethanolamine and piperazine. *Energy Procedia* 4, 1323–1330. <https://doi.org/10.1016/J.EGYPRO.2011.01.190>
- Wanderley, R.R., Pinto, D.D.D., Knuutila, H.K., 2020. Investigating opportunities for water-lean solvents in CO₂ capture: VLE and heat of absorption in water-lean solvents containing MEA. *Sep. Purif. Technol.* 231, 115883. <https://doi.org/https://doi.org/10.1016/j.seppur.2019.115883>
- Wanderley, R.R., Yuan, Y., Rochelle, G.T., Knuutila, H.K., 2019. CO₂ solubility and mass transfer in water-lean solvents. *Chem. Eng. Sci.* 202, 403–416. <https://doi.org/https://doi.org/10.1016/j.ces.2019.03.052>
- Wang, M., Lawal, A., Stephenson, P., Sidders, J., Ramshaw, C., 2011. Post-combustion CO₂ capture with chemical absorption: A state-of-the-art review. *Chem. Eng. Res. Des.* 89, 1609–1624. <https://doi.org/10.1016/j.cherd.2010.11.005>
- Wang, T., Yu, W., Le Moullec, Y., Liu, F., Xiong, Y., He, H., Lu, J., Hsu, E., Fang, M., Luo, Z., 2017. Solvent regeneration by novel direct non-aqueous gas stripping process for post-combustion CO₂ capture. *Appl. Energy* 205, 23–32. <https://doi.org/https://doi.org/10.1016/j.apenergy.2017.07.040>
- Wu, Y., Mirza, N.R., Hu, G., Smith, K.H., Stevens, G.W., Mumford, K.A., 2017a. Precipitating Characteristics of Potassium Bicarbonate Using Concentrated Potassium Carbonate Solvent for Carbon Dioxide Capture. Part 1: Nucleation. *Ind. Eng. Chem. Res.* 56, 6764–6774. <https://doi.org/10.1021/acs.iecr.7b03637>
- Wu, Y., Tao, L., Wu, F., Mirza, N.R., Stevens, G.W., Mumford, K.A., 2017b. Precipitating Characteristics of Potassium Bicarbonate Using Concentrated Potassium Carbonate Solvent for Carbon Dioxide Capture. Part 2: Crystal Growth. *Ind. Eng. Chem. Res.* 56, 15131–15142. <https://doi.org/10.1021/acs.iecr.7b03637>
- Yu Chih-Hung and Tan, Chung-Sung, C.-H. and H., 2012. A Review of CO₂ Capture by Absorption and Adsorption. *Aerosol Air Qual. Res.* 12, 745–769. <https://doi.org/10.4209/aaqr.2012.05.0132>
- Zarzycki, R., Chacuk, A., 1993. *Absorption: Fundamentals & Applications*. Pergamon. <https://doi.org/https://doi.org/10.1016/C2009-0-14786-4>
- Zhang, G., Yang, Y., Xu, G., Zhang, K., Zhang, D., 2015. CO₂ capture by chemical absorption in coal-fired power plants: Energy-saving mechanism, proposed methods, and performance analysis. *Int. J. Greenh. Gas Control* 39, 449–462. <https://doi.org/https://doi.org/10.1016/j.ijggc.2015.06.006>
- Zheng, C., Tan, J., Wang, Y.J., Luo, G.S., 2013. CO₂ Solubility in a Mixture Absorption System of 2-Amino-2-methyl-1-propanol with Ethylene Glycol. *Ind. Eng. Chem. Res.* 52, 12247–12252. <https://doi.org/10.1021/ie401805n>
- Zheng, C., Tan, J., Wang, Y.J., Luo, G.S., 2012. CO₂ Solubility in a Mixture Absorption System of 2-Amino-2-methyl-1-propanol with Glycol. *Ind. Eng. Chem. Res.* 51, 11236–11244. <https://doi.org/10.1021/ie3007165>



ISBN: 978-91-7422-726-0

Department of Chemical Engineering
Faculty of Engineering, LTH
Lund University

